Achieving Higher Fidelity Building Response through Emerging Technologies and Analytical Techniques

Thesis by

Anthony Thomas Massari, P.E., LEED AP

In Partial Fulfillment of the Requirements for

the degree of

Doctor of Philosophy

CALIFORNIA INSTITUTE OF TECHNOLOGY

Pasadena, California

2018

(Defended July 14th 2017)

Anthony Thomas Massari, P.E., LEED AP

ORCID: 0000-0002-6561-4674

Acknowledgements

I would like to start by thanking the California Institute of Technology for giving me the opportunity to work in an incredible community of researches, faculty and students. The support of the institute throughout my five years here will not soon be forgotten, and I am grateful for having been a part of this unique place.

From the faculty, I would especially like to thank Thomas Heaton for taking me under his wing and guiding be along this journey. Your advice and open door have been an unquantifiable resource to me over these years. Thank you Monica Kohler, and everyone else from the Community Seismic Network team, for letting me work with you on this exciting project.

To my cohorts here in the MCE department, it would have been a very different experience without you all. A special thank you to Christopher Janover, who was my colleague back in New York prior to coming here and who convinced me that Caltech was the place to be. To Andres Goza, Tess Saxton-Fox, Alex Zelhofer, Grant Hollis, Arnar Bjornsson, Ramses Mourhatch and Abel Dizon, who have all been fantastic researchers and people to bounce ideas off. Additional thanks to Kenny Buyco for being a fantastic lab mate to share thoughts with daily.

To my parents, who have been my supporters my entire life. From hockey practices to engineering school, you have always encouraged me to keep doing what makes me happy, and your enduring support of my endeavors has been a truly precious gift. To my brother, Seaman Jonathan Massari of the United States Coast Guard, you have been an inspiration and friend in more ways then I can say.

Lastly, to my fiancé Bailey, whom I can not wait to share the rest of this life with. Your unwavering support through this has meant the world to me. I can't wait for what lies ahead for both of us as we continue our adventure together.

A b s t r a c t

The integration of sensor technology into the built environment has created an opportunity for a new approach to infrastructure development and management. Using collected data and principles of general physics, we discuss means and methods of using low cost dense instrumentation to perform damage detection, structural identification, and the benefits of cyber physical systems to community resilience. A nonlinear damping strategy for braced frame structures is introduced incorporating capped levels of damping forces. The study shows the effect of having control of damping forces in nonlinear analysis and the importance of limiting energy dissipation to rational levels. The issue of sliding mass is also studied to determine the contribution to energy loss and the effect to overall response. The results indicate a need to incorporate this effect in stiff structures with intentionally decoupled mass such as data centers. Finally, a discussion on dual system structures under plastic deformation in a post event deformed configuration is presented. A suggested displacement based method for design is suggested for implementation into future editions of the building code.

Introduction

Structural health monitoring is a highly studied field of engineering that spans various types of infrastructure (buildings, dams, bridge, planes, etc.). Due to the restrictions of a fully sensored system, many methods of evaluation contemplate sparse instrumentation concerns in order to develop more fine levels of detail of a structures state. However, with affordable technology becoming more accessible, instrumentation density is increasing throughout the built environment. This level of concentration of instruments presents a new field of problems in data interpretation and utility. Chapter 1 focuses on contributions of the Community Seismic Network (CSN), which is responsible for distributing and interpreting this new type of data in order to prepare for large scale events in the future.

Damping strategies used in nonlinear structural analysis contribute significantly to the computed responses in a building type structure. Chapter 2 explores commonly used damping strategies and their shortcomings (e.g. lack of physicality). They are compared with a variation of nonlinear damping that incorporates a plastic capping force on a particular story based on the local plastic shear capacities of the structure. The study is complemented with computational design information associated with application to a brace frame structure. To help bridge the gap between research and application, the brace frame with capped damping is then modeled in a software platform, Perform 3D, the industry standard for performance based design. Finally, to understand the effect of varied levels of capping force, a sweep of practical levels of damping maxima's is conducted to show the sensitivity in this analysis parameter.

Nonstructural components in buildings are known to contribute to the dynamic response of a structure. In particular, the effect of partitions and rigid connections of a building to components have been studied extensively. However, little has been done to address or quantify the potential for nonstructural components sliding in a building and the effect of mass mobility on overall dynamic response and energy dissipation. In certain applications, this behavior can have significant effect on the dynamic response of a structure, particularly when sliding is intentionally implemented in industrial applications (e.g. data centers, storage facilities, nuclear power plants, etc.). Chapter 3 is a computational study that quantifies the potential effect of sliding mass on the overall response of occupied structures based on a series of building heights and relative potential sliding masses.

U.S. building codes mandate the use of a dual lateral system in braced frame building structures over a certain height in high seismic regions. This dual system requirement, which incorporates an additional intermediate moment frame, is meant to provide added ductility during a seismic event, as well as maintain stability of the braced frame structure after it has been weakened by large scale shaking. The standard for design of this secondary frame is such that 25% of the effective earthquake force is used to develop the design level forces. Chapter 4 challenges the code based design metrics and their validity in satisfying the code intent for stability in the inelastic post event state. A proposed modification to the design procedure that is consistent with the intent of the code is also discussed.

Table of Contents

List of Figures

List of Tables

Chapter 1

CONTRIBUTIONS TO THE COMMUNITY SEISMIC NETWORK, STRUCTURAL HEALTH MONITORING, AND DAMAGE DETECTION INITIATIVES

1.0 Introduction:

Common forms of structural health monitoring (SHM) rely on routine or scheduled inspection of critical infrastructure. In general, these types of practices are embodied in all civil engineering projects. Those with higher risk or more prone to defects typically have more rigor and frequent evaluation. A common example of this type of inspection strategy is the New York City program for buildings that fall under the Façade Inspection and Safety Program (FISP or Local Law 11). This program requires all buildings over six (6) stories to be inspected every five (5) years for defects, indications of settlement, and water infiltration. The program works to prevent conditions of falling debris on streets as well as address any potential unrecognized water intrusion that can lead to damage over time. These inspections are often only visual (sometimes performed from street level with a pair of binoculars) and are a practical, if not overly simplistic, way of evaluating the potentially hazardous condition.

Methods such as these are simple and can suffice in many different forms of hazard; however, more complex forms of damage which are not necessarily visible from the exterior of a structure require the use of nondestructive means and methods. Various forms of these types of nondestructive methods exist and are excellent means of evaluating structures at a localized level (welds, connection, fractures, etc.). One of the most common forms of localized nondestructive testing is ultrasonic testing. Ultrasonic testing makes use of transducers that convert electrical energy into acoustic signals (and vice versa) that seek to locate discontinuities using a pulse like signal that reflect portions of energy at discontinuities. The reflections create arrivals at intervals and amplitudes that are used to investigate flaws within a material. These types of methods are often not required and are only implemented when included in the specifications of a project. Further, their implementation on a large structure over many thousands of potential damage locations is not a practical means of determining where flaws and/or damage may be located.

Given the impracticality of localized damage detection strategies on a full scale structure, techniques based on overall structural response have been studied for many years in the field of

monitoring. Making use of various techniques, the fundamentals of structural identification aid in determining dynamics properties (eigen functions, frequencies, damping, etc.) (Goel, 1997) that can be used for model verification and tracking variations to assess levels of damage over time (whether prior, during, or after an event) (Bradford, 2006). Many of these solutions work to overcome a common issue in modern structural health monitoring systems' sparseness of instrumentation/measurement.

The Community Seismic Network (CSN) at the California Institute of Technology has developed a framework that directly addresses the concerns of sparse instrumentation, facilitating a new opportunity in how to better assess the built environment at a scale that is unprecedented. Key to this network's functionality is low-cost instrumentation and cloud-based data management, which allows for a robust, scalable network with continuous data collection. Working with data from CSN, as well as developing synthetic information similar to CSN type collections anticipated from the field, a series of studies and implemented technology based on dense instrumentation are presented. The net result of this body of work is to show the utility of this type of data collection, as well as what types of computational tools and resources are useful a priori.

1.1 Current City-Scale Building Infrastructure Monitoring:

Structural monitoring platforms and regulations exist throughout many cities in the United States as well as the rest of the world. An example is the current requirements of structures designed using performance based techniques (or more generally nonlinear response history procedures) in Los Angeles that are subject to special station deployment rules and regulations (Information Bulletin P/BC 2014-117). These are summarized below in Table 1.1.

Number of Stories Above Ground	Minimum Number of Channels
6-10	12
11-20	15
21-30	21
31-50	24
> 50	30

Table 1.1 Los Angeles Department of Building and Safety information bulletin/public – building code document P/BC 2014-117 (LABC 1613.10.2) minimum number of channels based on number of stories above ground

Instrumentation programs similar to those found in Los Angeles have become more common place in recent years, but still lack the density of instrumentation on every floor. The sparseness of this data over the height of a building creates issues with determining the total response of the structure. Further, the processing of this type of information is not common to engineers, and so the utility of the data in the building industry has been lacking. As recently as 2017 this type of data was mined by two independent researchers for damping properties in buildings (Cruz, et al., 2017 and Xiang, et al., 2017), for which the disparity of inferred damping values was vast between the studies.

Making use of this type of data requires a better understanding of what types of information are imbedded in measurements, as well as a means and method to resolve the measured signals to understand the structural response in a useful way.

1.2 Alternative Computational Method for Condensed System Models

Computational modeling of building type structures is common practice in modern construction of mid to high-rise buildings. While not required in all jurisdictions, various nations require the submission of finite element models to building departments for final approval of a given piece of infrastructure. These models are typically complex, full of many degrees of freedom (D.O.F.), and offer little opportunity for a jurisdiction to make use of the information provided.

While complexity in computational models in design of a structure is merited, and jurisdictional review of these models is encouraged, the resources afforded to many building departments are not sufficient to facilitate the potential usage of these types of complex models in response to any form of shock event (earthquake, flood, hurricane, etc.) on a large scale. Further, running simulations of an event without verification of the behavior has the potential to compound an error in on itself.

An alternative to these high fidelity models is to create lower order models based on the fundamental mechanics of a building type structure. Buildings tend to have a significant portion of the mass of the structure placed at the floor level of a building. As such, a common practice in structural engineering is to lump mass at the story level, creating a more discrete model of the system. Taking advantage of this characteristic of a structure, another common practice is to extract the fundamental motion of the structure for a reduced order system. This reduced order system contains only the massed degrees of freedom, but requires mathematical rigor to accurately describe the structure for the dynamic problem.

Reducing the higher order problem to only include the dynamic degrees of freedom is a process known as static condensation. Static condensation is simply the reduction in order of a numerical problem of many degrees of freedom to one which is dependent only on the degrees of freedom where forces can be applied. In a dynamic system, this is accomplished by a series of routine matrix manipulations. See Appendix A for details.

These types of models are considerably more manageable; however, they require access to the computational matrices of the structure to develop the reduced order models. Getting a handle on these components of the structure is difficult and often not available in many cases using commercial software. Further developing these types of reduced order models from scratch for complex structures can often be an unreasonable task. This creates a need for a modeling strategy to extract this type of information from a computational model to develop these reduced order systems.

The main objective of static condensation is to produce the stiffness matrix for which only the degrees of freedom of interest (dynamic degrees of freedom) are present. This can be done effectively within the framework of a finite element program by making computational use of the basic premise of the "pop and lock" structural analysis technique. By selecting the degrees of freedom of interest in the computational space, and restraining all but one of those degrees of freedom, an analysis can be performed systematically where under a given force, the displacement can be measured directly to determine the structural stiffness along the stiffness matrix diagonal. Furthermore, the reactions at the constrained degrees of freedom can be used to construct the remaining components of a single column of the stiffness matrix.

Suppose the size of our reduced system is to have only N degrees of freedom. At any degree of freedom within the set N, we want to run a specific analysis where a single degree of freedom n is free, while all other degrees of freedom of the condensed system are constrained. By applying a force at degree of freedom n, and analyzing the structure, we can determine the displacement u_n at degree of freedom n. Knowing the force applied at the floor, we can infer the stiffness for this constrained structure. This single value can be processed for each and every degree of freedom of interest and will populate the diagonal of the stiffness matrix.

$$k_{n,n} = \frac{F_n}{u_n} \tag{1.1}$$

The rest of the column of the stiffness matrix is a result of examining the reactions at all subsequent degrees of freedom (R_l) and dividing by displacement magnitude at degree of freedom n.

$$k_{l,n} = \frac{R_l}{u_n} \tag{1.2}$$

Each of these values combined into a column array would make the n^{th} column of the stiffness matrix. This column is size N x 1:

$$k_{:,n} = \begin{pmatrix} k_{1,n} \\ \vdots \\ k_{(n-1),n} \\ k_{n,n} \\ k_{(n+1),n} \\ \vdots \\ k_{N,n} \end{pmatrix} \tag{1.3}$$

Executing this process for every degree of freedom desired in the model, one can construct the fully reduced stiffness matrix from the computational model:

$$\boldsymbol{K_{red}} = \begin{pmatrix} k_{1,1} & \cdots & k_{1,n} & & k_{1,N} \\ & \ddots & \vdots & & \\ & & k_{(n-1),n} & & \\ \vdots & & k_{n,n} & & \vdots \\ & & k_{(n+1),n} & & \\ & & \vdots & \ddots & \\ k_{N,1} & & k_{N,n} & \dots & k_{N,N} \end{pmatrix} \tag{1.4}$$

This numerical process is susceptible to round-off error and therefore requires regularization to construct a truly positive definite matrix. This is overcome by simply averaging all off diagonal terms:

$$\boldsymbol{K}_{l,n} = \frac{\boldsymbol{K_{red}}_{l,n} + \boldsymbol{K_{red}}_{n,l}}{2} \tag{1.5}$$

The reduced system has a complimentary mass matrix, that has the equivalent story mass at every floor of the structure associated with translation. While not done for this particular study, torsional modes and effects could also be included in this reduction. This would require the determination of the polar inertia about the reference point in the story and the adoption of a rigid diaphragm in the structure. In a general sense, the polar inertia (I_n) is described by Eq. 1.6 where I_n is the polar inertia of story n, r_i is the radius from any i^{th} mass on the story of interest ($m_{n,i}$), and j is the total number of masses on the floor.

$$I_n = \sum_{i=1}^{j} r_i{}^2 m_{n,i} \tag{1.6}$$

Oftentimes programs default to reporting the polar moment inertia about the vertical axis at the origin of a model. If polar inertia is provided this way, the parallel axis theorem can be used to translate the coordinates of interest in the model by the distance d.

$$I_{n\_adj} = I_{n\_provided} - m_n d^2 \tag{1.7}$$

Next a linear damping matrix consistent with the intended behavior of the structure is constructed. There are many potential linear damping strategies used in the development of computational models. One of the most common is Rayleigh damping, discussed later in this thesis (Section 2.1), and implemented in subsequent studies using reduced order models.

This application of computational condensation was implemented for a 52 story building model (Section 1.4.1) for translational degrees of freedom at every floor of the structure. Table 1.2 shows a comparison of the reduced system and the full systems modal frequencies. In this particular case, the model has 29,538 degrees of freedom and was reduced to contain only the dynamic degrees of freedom associated with translation in the North-South and East-West leading to a 104 D.O.F system. This reduced system was able, with a high level of accuracy, to mimic the linear dynamic properties of the system.

	East-West Periods(s)		North-South Periods (s)	
Mode	ETABS Model	Reduced Order Model	ETABS Model	Reduced Order Model
1	5.903	5.903	5.574	5.572
2	1.673	1.673	1.642	1.642
3	0.872	0.871	0.909	0.908
4	0.597	0.598	0.686	0.684
5	0.471	0.471	0.564	0.563

Table 1.2 Comparison of finite element model modal properties to reduced order model

These reduced order models are more tangible, and, with torsion included in the analysis, only require 3N x 3N (N = number of stories of the structure) matrices to describe the system. This allows for a more reasonable computational framework for building departments to manage as a network of structures. Given these reduced order models and data about the ground excitation, building departments could run an analysis on every building structure in the built environment to determine how much linear

deformation was expected. This linear deformation can be analyzed to see if nonlinear actions are likely to have occurred in the system. This information can then be translated into potential inspection protocols after a significant event, or more importantly, into potential reaction metrics for first responders in a large scale earthquake.

Further, this type of analytical response could be coupled with instrumentation response, where resultant displacement fields from computational analysis can be compared with those received from a network of instrumentation throughout a building's structure. While it is unlikely that the forward model would be 100% accurate, large dispersions from these forward models relative response to the measured data could also be used as a metric for resilience after an event.

When evaluating a reduced order model, the main metric that could be extracted to determine if local deformation exceeded anticipated values would be localized story drifts. This drift can be translated into strains of objects used to span the space (braces, columns, walls, etc…) between floors, as well as be used as an indicator for local strains. These local strains can be used to determine the general state of an object's health (ex. Immediate Occupancy, Life Safe, Collapse Prevention), similar to the performance objectives described in documents such as ASCE 41-13.

Measurement of these types of local strains require instrumentation networks to be dense enough to make the measurements of interest. In Los Angeles, the current mandates for instrumentation in structures designed using nonlinear analysis roughly translate to a single three (3) components sensor every four to five stories of the building (See Table 1.1). This mandate greatly improves upon previous instrumentation requirements but still does not provide sufficient information for localization of drift at a story by story level. This is mainly due to the expense of instrumentation, and imparting that cost to developers is unreasonable at the price point of modern strong motion instrumentation.

1.3 The Community Seismic Network (CSN)

The USGS network of seismic instrumentation has a density of approximately 10-20km in the Los Angeles basin. This is much less then the desired level of density for refined seismology in urban monitoring. The variability of ground motions recorded by nearby stations is high and not easily estimated unless the station spacing is reduced to about 1 km or less (Instrumentation Guidelines for the Advanced National Seismic System, 2007). This variability is critical from the standpoint of critical facilities, first responders, and infrastructure management.

ShakeCast (ShakeCast User Guide, 2017) is an example of a product developed by the USGS which relies of local measurement data. ShakeCast is a program that leverages the output of ShakeMaps (ShakeMap User Manual, 2016) after a seismic event and uses local mapped values of peak ground motion characteristics to determine probabilistic evaluations of existing structures. The estimation of conditions of these structures are based on archetype fragility curves of buildings, but can also be based on custom fragilities of a particular structure. Figure 1.1 shows the form of typical fragility curves used in the ShakeCast program. Critical to the evaluation of the structure is the peak ground characteristic used on the x-axis to define the seismic hazard exposure to the structure. The level of accuracy of these measurements is ambiguous at best with the sparse instrumentation that is currently available in many of the high seismic regions of the United States making use of significant averaging and smoothing algorithms in-between stations to develop a consistent map.

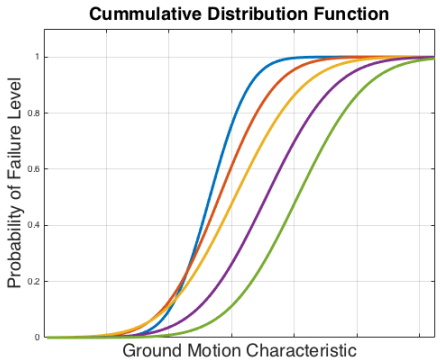

Figure 1.1 Sample of fragility curves used in ShakeCast to determine the probability of any failure level (Immediate Occupancy, Life Safe, Collapse Prevention, etc…)

To overcome these shortcoming of the current network, a sufficiently robust instrument is needed to perform local measurements in a reliable manner. The Community Seismic Network was created to address this problem, making use of community-hosted instrumentation deployed throughout the built environment to develop a densely instrumented Los Angeles basin. These instruments were originally meant for home owners and were deployed by connecting a small accelerometer via USB to a desktop computer and permanently affixing these instruments in a home or office. With the increased use of laptop computers, this method of deployment was found to be unsustainable. Now a more robust system inclusive of an accelerometer and onboard computer is used to assemble a self sustainable instrument. These instruments work on local Ethernet network connection and power, and provide a platform for

deployment that is more consistent with the community at large. When compared with typical seismic instruments, the CSN seismometer is developed at a fraction of the price (anywhere from $1/10^{th}$ to $1/100^{th}$ of the cost). This allows for the development of a much denser network that is better able to contribute to the various seismological initiatives of the USGS and others. More about this technology can be found in Clayton et al (2016) and references therein.

By having these low cost instruments available at a reasonable price point, it is possible that this type of sensor could be placed in the basement of every built structure in the city-scape. Having measurements made locally at a structure, the need for interpolation of values is reduced; creating an opportunity for a more accurate assessment of infrastructure in the field. ShakeCast is an example of one such program used today.

These locally collected waveforms at the base of a structure also offer a unique opportunity for a prepared city with reduced order models of structures. These waveforms could be passed directly into a database of computational models for local, on site assessment. The information can then be pushed out to interested parties (building departments, emergency services, insurance agencies, etc…) to assess the structural response at a higher order then typical fragilities allow.

Further, CSN instrumentation is deployed in building structures not only at ground level, but also at elevated stories. This use of the instrumentation allows for building response to be measured directly as opposed to forward modeled using computational frameworks. These responses and measurements over the height of a building can be used for various means of damage detection, structural identification, and potentially other forms of analysis.

To better understand building structure response after a significant event, instrumentation on every floor of a building is required to localize potential damage at a story by story level. Furthermore, if torsional characteristics play a significant role in the response, localized drifts at the extremities of the floor would require an inferred torsional response, necessitating at least two instruments on a floor level. This increase in instrumentation and cost would be a significant burden on owners and developers, creating the need for low cost solutions like CSN to develop seismic networks inside building type structures.

Figure 1.2 is an example of an response from the 2014 La Habra earthquake where a comparison was performed between a linear finite element model and the measurements made by the CSN network

on the 12th story of a building. A general agreement is observed between the model for amplitude and frequency content. While these two are likely to never be perfectly correlated, this type of information gives added confidence in our model for future studies and evaluation. Alternatively, if the responses were drastically different, one would presume that the model is poorly defined. If in future events a significant disparity arises, one might attribute this as an indicator of damage in a structure (more on this in later sections).

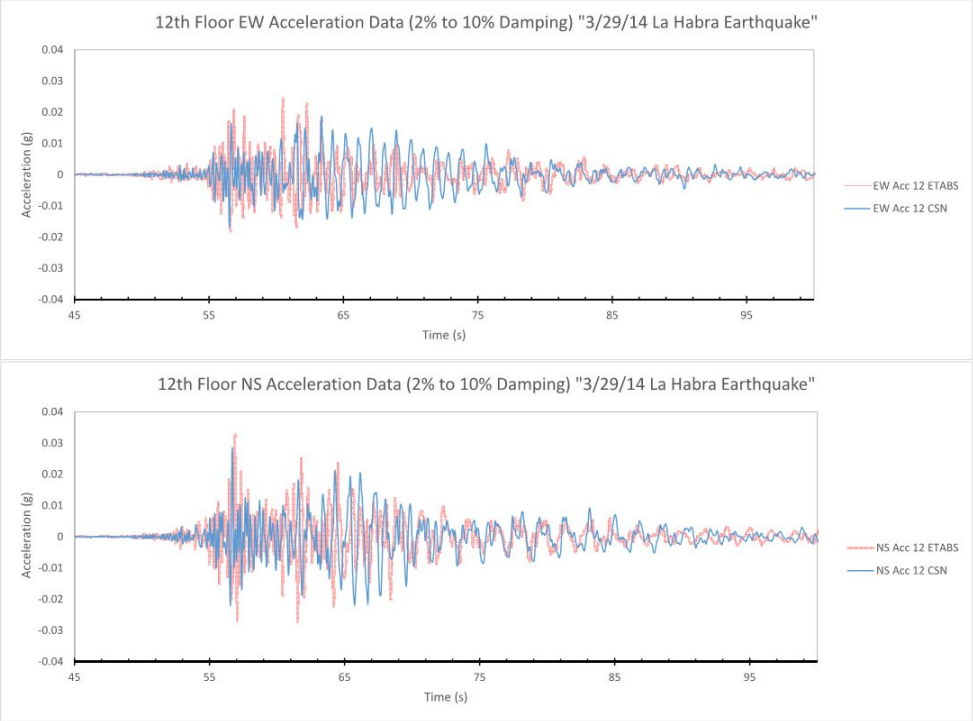

Figure 1.2 La Habra earthquake comparison of simulation vs measured accelerations during the La Habra earthquake in 2014

1.4 Buildings Models Developed for Studies of the CSN network

All buildings contained within this section were modeled using the finite element program ETABS by Computers and Structures Incorporated. The software is a standard of industry in the United States and around the world, and allows for this work to be directly translatable into the engineering community. ETABS offers many different analysis methods (linear, nonlinear, buckling, etc.) and element types, but for the purposes of these studies, we restrict our analysis to linear beams, columns, and shells (ETABS,

2016). These models were developed to perform computational studies based on real structures where CSN data is being collected.

Due to confidentiality restrictions, building information with respect to location is omitted when necessary per M.O.U. agreements made with respective owners/operators. Buildings will be referenced as A through D with minimal details with elaboration on Building A.

1.4.1 Building A - 52 story building in Downtown Los Angeles

Building A is a 52 story dual system structure in downtown Los Angeles that was constructed and designed in the late 1980's. The core of the structure is primarily made of a braced frame from the ground floor to roof, which then transitions to a moment frame at the crown portion of the structure. The columns of this braced core are cruciform in shape and offer similar bending inertia properties about either orthogonal axis. These cruciform column elements are connected throughout the height of the structure by continuous deep beam objects. These continuous or fixed beams act to outrigger the core to the peripheral columns, and contribute significantly to the overall stiffness of the building.

The effect of these continuous outriggers is substantial to the overall behavior of the structure. Releasing these objects over the height of building by pinning the ends of moment frame beams lengthens the fundamental period of the building from 5.903s to 9.302s (a 57.5% increase), indicating the importance of these moment frame connections over the height of the tower.

Building A, and other buildings like it, have many potential locations where damage could potentially exist or develop over time. The main potential failure mechanisms in this structure are associated with brace frame objects (buckling, yielding, gusset failure, etc…) and moment frame connections, as well as a combination of either over the height of the building. Based on the building's age of construction, it is particularly susceptible to the pre-Northridge earthquake moment connection issues, which are a well studied phenomena and a property of older moment frames (SAC Joint Venture).

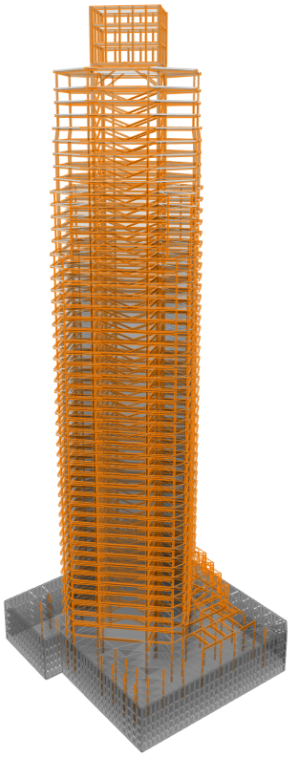

Figure 1.3 ETABS computational model of Building A

The structure is instrumented on every enclosed floor and allows for data to be collected for various events. One such event was the Castaic earthquake on January 4th, 2015 (M4.2). Acceleration data for this earthquake was collected on nearly every floor of the structure (See Figure 1.4). This same data was then brought from the time domain into the frequency domain to examine modal properties of the structure (See Figure 1.5). Here one can observe what floors have response at particular frequencies. Examining the zero crossings of the figure, one can determine the mode shapes of the structure by looking directly at these spectral maps. This type of data can be used for model verification when examining the dynamic properties of our ETABS models. As an example, a previous event (La Habra earthquake, M5.1 3/29/14) was used for initial verification of model behavior (See Figure 1.2). This image shows a strong correlation with the linear model and the response of the structure throughout.

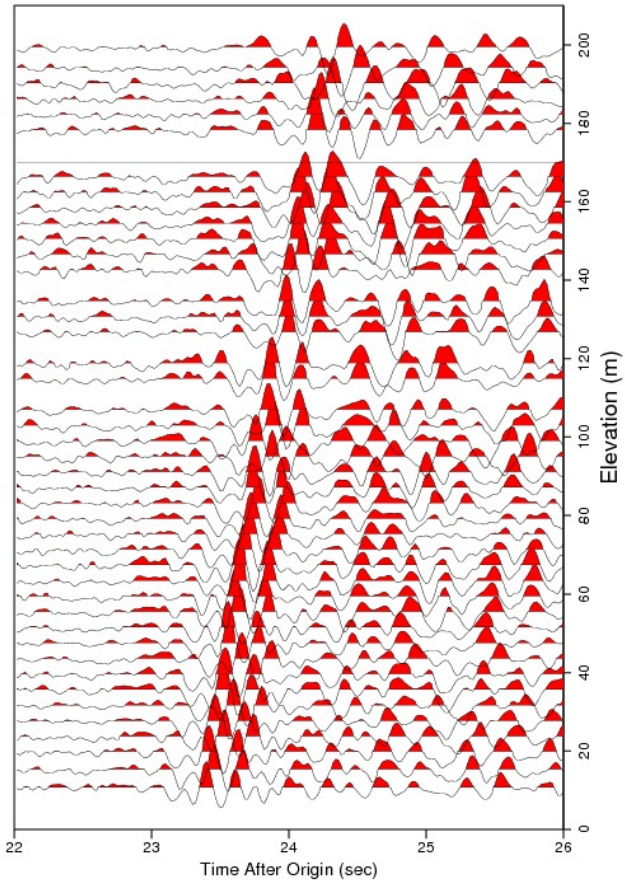

Figure 1.4 Castaic earthquake (M4.1 Jan 4th, 2014) time history of every measured floor (Clayton et. al. 2015)

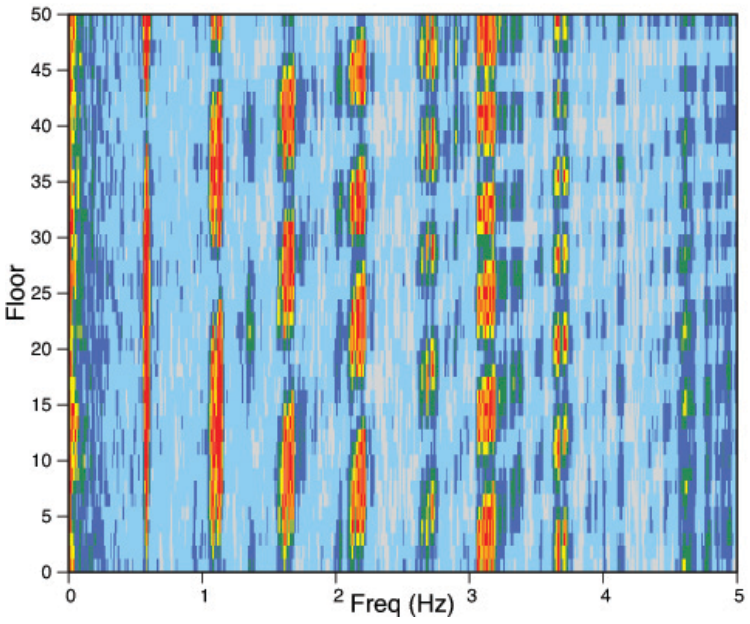

Figure 1.5 Spectra of Building A from the Castaic earthquake (M4.1 Jan 4th, 2014) . Shown are the floor-by-floor amplitude spectra of the east components of acceleration due to the 4.1 Castaic earthquake. The primary eigen modes can be resolved noting the zero crossings of the spectra at any particular frequency (Clayton et. al. 2015)

The computational model from ETABS was initially modeled with flexible diaphragm action to better account for the total physics of the structure. When these results were compared with the modal properties observed from data, the frequencies of the ETABS model were found to be a slightly low, indicating a lack of stiffness in the model. A simple revision of switching to rigid diaphragm action led to a more consistent set of modal frequencies compared to the data collected (Figure 1.5).

Dynamic studies were conducted in the modal coordinate frame, allowing for expedited solution time and control of modal damping ratios directly. Damping was assigned to 1% for the first 17 modes, and all subsequent modes were given 10% damping (the cutoff frequency being 1.5 Hz). Computational results were compared with measurements in the field for a series of events (ex. Figure 1.2 and Figure 1.4). The first five (5) translational modes shapes are shown in in Figure 1.6 and Figure **1.7**, and the first primary periods are shown in Table 1.3.

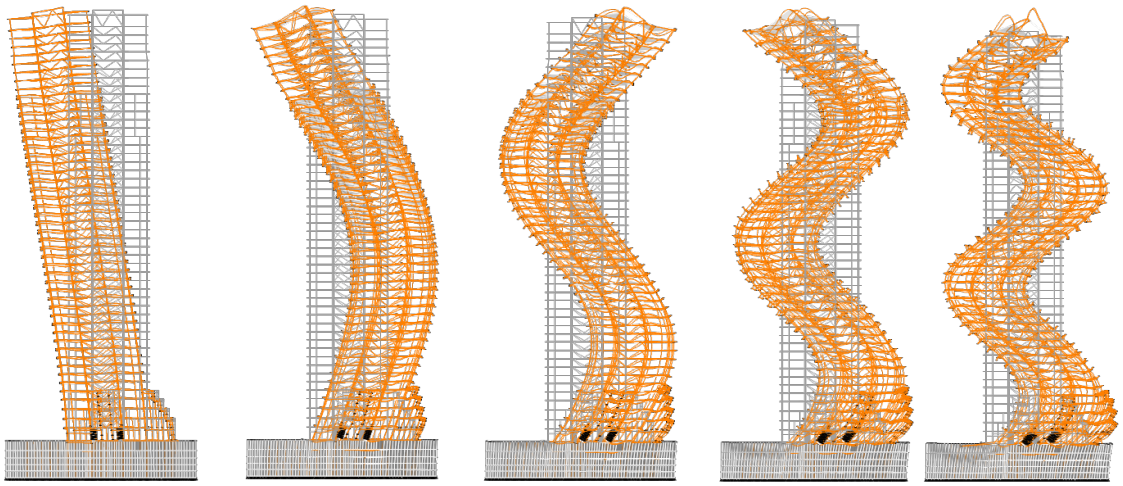

Figure 1.6 Building A East-West mode shapes (Kohler et. al. 2016)

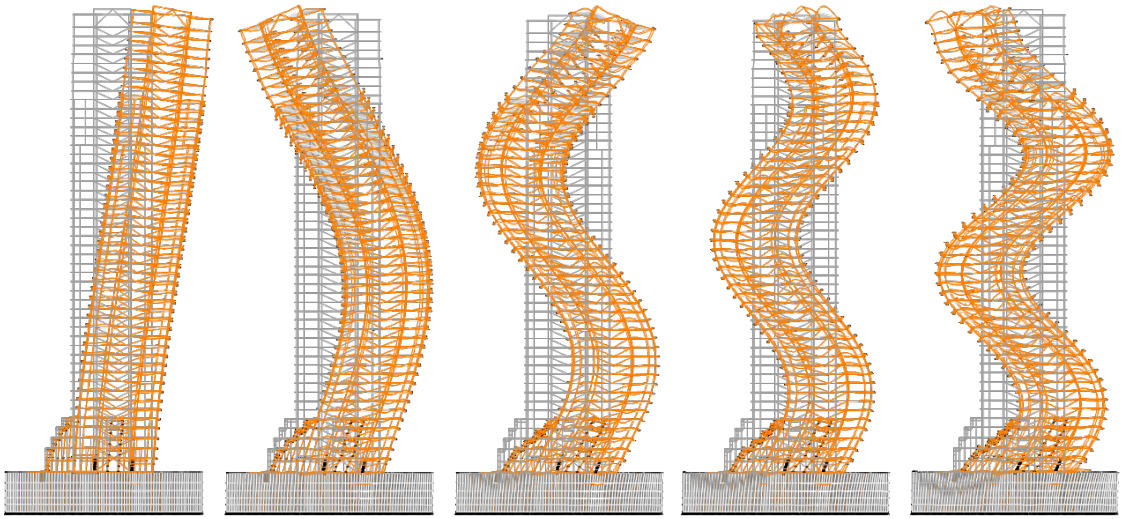

Figure 1.7 Building A North-South mode shapes (Kohler et. al. 2016)

Building A Modal Properties

Mode	E-W	N-S	T
1	5.903s	5.574s	5.252s
2	1.673s	1.642s	1.870s
3	0.872s	0.909s	1.134s

Table 1.3 Building A modal properties based on ETABS model

1.4.2 Building B

Building B is a nine story building constructed in the 1960's at NASA's Jet Propulsion Laboratory and serves as the main administration building on campus. The building's lateral system consists of moment frames in either direction that share a common column (enforcing bi-direction bending in all primary columns). Unique to this structure are the beams of the moment frame, which are truss structures assembled from C-channels, WT sections, and double angles. These trusses offer a unique opportunity to examine truss beam type failure that can involve buckling of local slender objects throughout the span. These susceptibilities associated with slenderness of components are a very different mechanism from the damage studies possible in Building A.

Similar studies into the dynamic properties and time series information that were performed on Building A were also performed for this model. A summary of the modal periods is provided in Table 1.4.

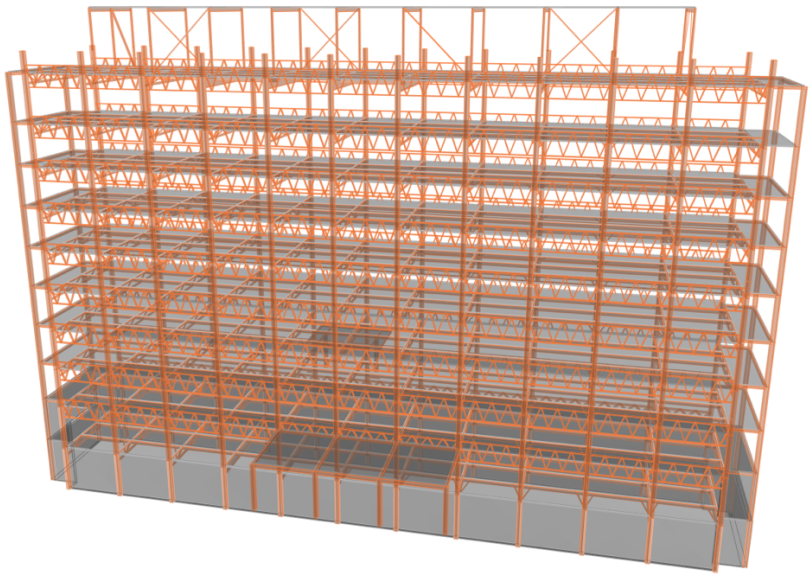

Figure 1.8 Building B ETABS model

Building B Modal Properties

Mode	E-W	N-S	T
1	0.900s	1.117s	0.945s
2	0.307s	0.352s	0.292s
3	0.200s	0.300s	0.187s

Table 1.4 Building B modal properties based on ETABS model

1.4.3 Building C

Building C is an eight story building constructed in the 1960's with a lateral system of intersecting moment frames (traditional steel beams in the North-South direction and truss moment frames in the East-West direction). Unique to the structure is the the addition on the east side of the building that is connected through the podium structure, but decoupled with an expansion joint at the floors above. This creates a unique appendage type behavior of the addition, and leads to interesting behavior in the frequency content of the structure overall.

Similar studies into the dynamic properties and time series information that were performed on Building A were also performed for this model. A summary of the modal periods are provided in Table 1.5.

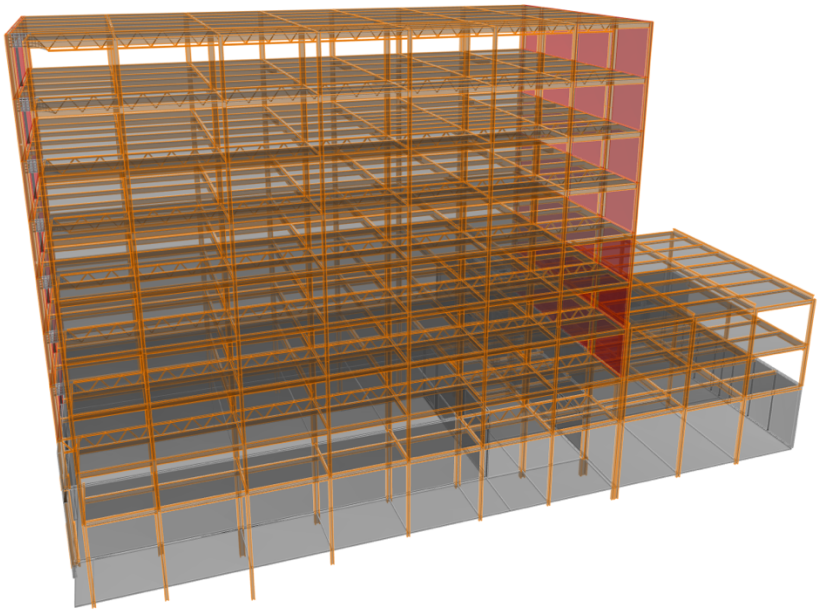

Figure 1.9 Building C ETABS model

Building C Modal Properties

Mode	E-W	N-S	T
1	1.467s	0.806s	0.492s
2	0.506s	0.382s	0.364s
3	0.296s	0.172s	0.265s

Table 1.5 Building C modal properties based on ETABS model

1.4.4 Building D

Building D is a 15 story building in downtown Los Angeles. The moment frame structure was constructed in the 1960's, making it susceptible to pre-Northridge moment connection failures. The building has a unique tall first story which relies on a concrete core wall structure to stiffen the lower level.

Similar studies into the dynamic properties and time series information that were performed on Building A were also performed for this model. A summary of the modal periods is provided in Table 1.6.

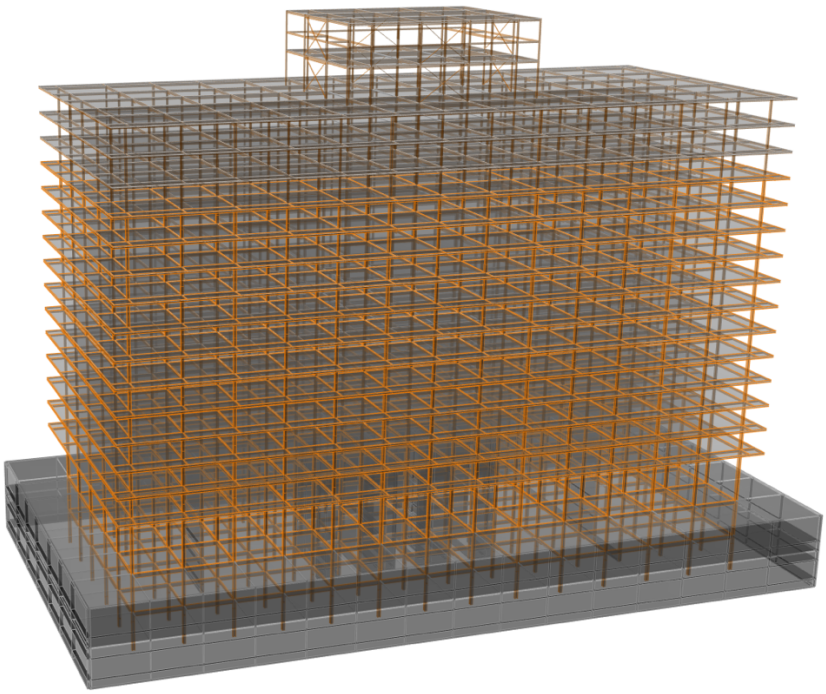

Figure 1.10 Building D ETABS model

Building D Modal Properties

Mode	E-W	N-S	T
1	3.189s	3.189s	3.290s
2	1.236s	1.208s	1.231s
3	0.786s	0.770s	0.730s

Table 1.6 Building D modal properties based on ETABS model

1.5 Forward Modeling Coupled with Recorded CSN Data

While examples of reduced order models in a city-wide array are of significant interest (Section 1.2) there is also potential for an owner to make use of computational models that were developed for a particular structure and then verified with instrumentation. Well formulated forward models present an opportunity for assessment of a structure at an element by element basis. These forward model results can then be used as a means of behavioral assessment after a significant event to determine if any component neared a failure state.

In the case of Building A, there are two main components to the lateral system where intended nonlinear mechanisms exist. They are the braces of the core and the beam ends of the continuous outrigger/moment frame. Given a ground motion, the verified forward model response can be used as a benchmark for potential damage prior to any nonlinear events.

The LA Habra earthquake event (M5.1 3/29/14) was measured by CSN instrumentation at the ground level, as well as throughout the building height, and used for verification of the forward model. From this event, the ground motion data was used as input for the finite element model to assess the potential for damage in the structure on an element by element basis. This relatively insignificant event produced minimal stress on the system, but offers insight into how assessment from a computational model could be used to do a higher order evaluation of a structure as opposed to reduced order systems mentioned earlier.

As stated, Building A has two primary nonlinear mechanisms that will be assessed. This assessment is based on *design* strength as apposed to *expected* strength. This is a conservative approach, as expected strengths are often higher then design strengths; however, this approach assesses the stress in the system relative to the intent of the design (and not to assess nonlinear behavior directly).

To evaluate the brace sections, we assume that all connections are sufficient to develop the strength of the section in tension and compression, and merely apply the AISC design equations for design in compression and tension. Tension strength is based on the yield strength of the material (in this case, A992 steel is used with Fy=50ksi). For compression strength, inelastic and elastic buckling limits are investigated based on AISC provisions.

To evaluate the outrigger beam elements, all beams are assumed adequately braced by the concrete floor slab such that full plastic capacity is reached in the beam. No composite action or gravity preload is taken into consideration for the evaluation.

After analysis, it was found that for the La Habra event, a maximum interaction of 8.9% was found in the brace frame of the structure on the 43rd floor. In this location, a W14x120 beam spans 9.5m leading to a KL/r of approximately 100. This relatively slender brace had a force time history shown in Figure 1.11. This same force is converted to stress and shown in Figure 1.12 relative to the limits states of tension yielding and compression buckling. A peak interaction of 3.5% was found in the moment frame on the same floor (See Figure 1.13 and Figure 1.14). This upper level peak response can be associated with the higher mode effects of this high rise building, creating an amplified force profile in the upper levels (See Figure 1.15).

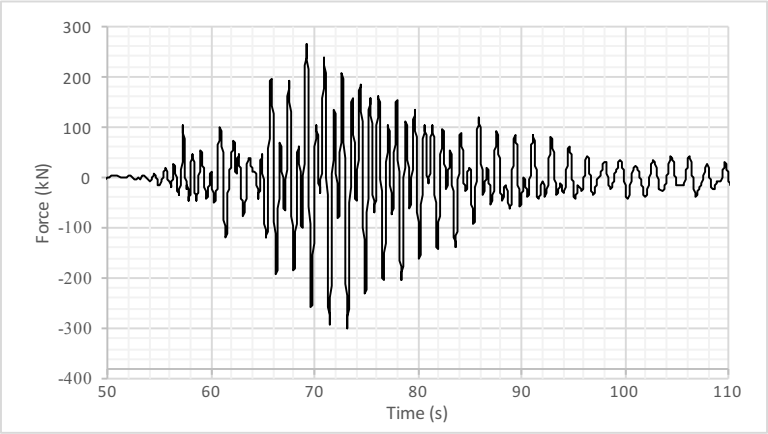

Figure 1.11 Time history for brace at level 43 with peak interaction axial force

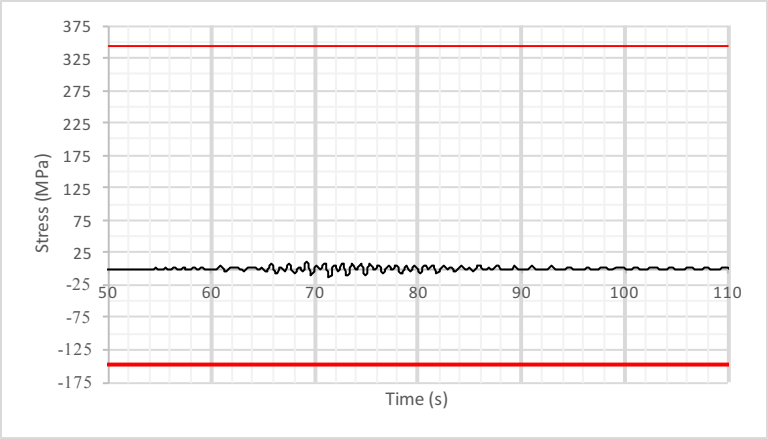

Figure 1.12 Time history for brace at level 43 with peak interaction of axial stress relative to peak design forces for tension yielding and compression buckling

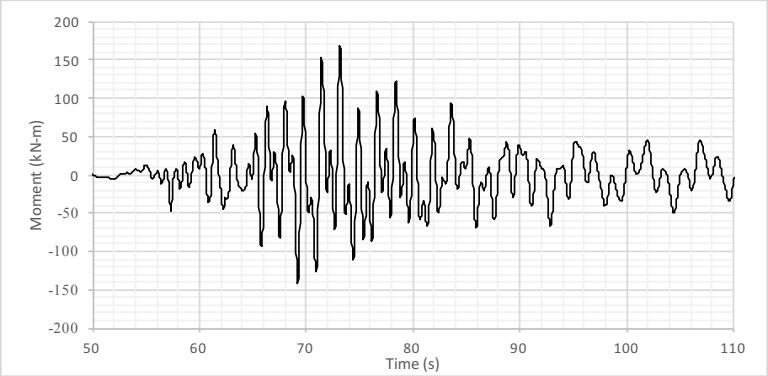

Figure 1.13 Time history for brace at level 43 with peak interaction end moment

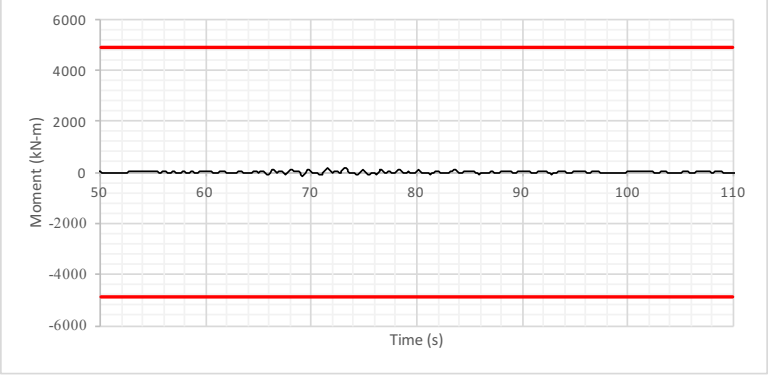

Figure 1.14 Time history for beam at level 43 with peak interaction of bending moment relative to plastic design moment capacity

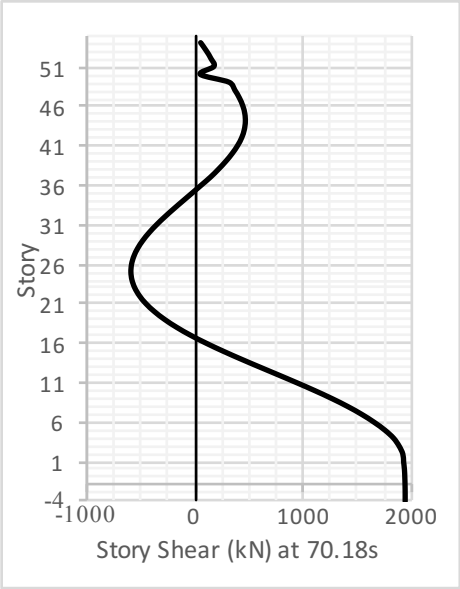

Figure 1.15 Story shear at time step of peak element interaction

These types of post event evaluations can be done independent of seismic instrumentation on a floor-by-floor basis. Critical to this procedure is a good physical model of the system and a reasonable understanding of the ground motion input. As stated in previous portions of this section, the value of having the dense instrumentation is in the validation of the model and the overall response.

This level of detailed analysis is also not feasible in the reduced order systems mentioned earlier (Section 1.2). Reduced order models do not have the element by element information to allow for the detailed level of element level performance shown here, but would rather offer a story level response (drift) that would need to be used to infer element strain indirectly.

1.6 Display

CSN measures acceleration data serves many uses in both ground and building arrays. For ground arrays, this type of information can be used for input ground motions in analysis. In particular pick data associated with thresholds is used for programs like Earthquake Early Warning (EEW) and ShakeCast.

In the building arrays, acceleration data is also useful and often used as a metric for nonstructural components damage (Taghavi, 2003). Here peak floor accelerations are used with fragility curves to determine the state of these secondary components. Similarly, this type of data, coupled with a

distribution of mass in the system, can be used to determine time history information of the structural demands associated with shear and overturning moment.

While acceleration data is useful, displacement data is often used as a primary metric for structural response. Given the displacement in a building over time at every floor, secondary calculations such as inter-story drifts are also useful to determine local shear strains within a structure. These drift values can be used as a valuation of damage in a structure from both a structural and nonstructural components perspective.

CSN has developed a web based display that broadcasts this data to the end user via their web browser. The acceleration response of each floor is double integrated to develop the displacement response over time of the structure. These displacement responses are used at every time step to calculate localized story drifts (γ) in the system

$$\gamma = \frac{u_i - u_{i-1}}{h_i} \tag{1.8}$$

For the real-time display, this type of information is not particularly useful, as it requires the user to be watching the display during a significant shock event. There are instances, however; where this type of data might be useful directly (windy days and associated complaints with potential sea sickness) and also indirectly (the display acting as a network health monitor). Unfortunately, the collected data for these types of low intensity events are often found to be noisy and give little confidence into the actual response of the structure.

To deal with this issue, we provide a modal fit to collected data which smoothens the structural response between floors based on a number of modes used in the fit. While this creates a level of abstraction from the data during the real time display, this fit is only used to make the display appear more realistic. All local measurements associated with peak values (drift, acceleration, etc.) are independent of these results, and are based on the raw analytics and stored with peak values over predetermined time intervals.

To develop the modal fit, we take results from the eigen analysis of any ETABS model and store the mode shapes of interest. For the purposes of numerical orthogonality, the mass matrix is also extracted from ETABS to aid in our fitting method. The displacement field at any time can be formulated as the summation of the eigen vectors with a certain contribution as follows:

$$u(t) = \sum_{i=1}^{m} q_i \phi_i \tag{1.9}$$

where $u(t)$ is a vector of the entire displacement field at any particular time, q_i is the i-th integer modal coordinate, and ϕ_i is a vector representing the i-th mode shape of the structure. To determine the modal coordinate, we multiply both sides by the Mass matrix and a particular mode of interest.

$$\phi_k{}^T \boldsymbol{M} u(t) = \sum_{i=1}^{m} q_i (\phi_k{}^T \boldsymbol{M} \phi_i) \tag{1.10}$$

Based on modal orthogonality principles, for all modes where i≠k, the quantity on the right hand side is zero, and therefor we can drop the summation sign and only work with mode k.

$$\phi_k{}^T \boldsymbol{M} u(t) = q_k (\phi_k{}^T \boldsymbol{M} \phi_k) = q_k M_k \tag{1.11}$$

where M_k is the modal mass. We can now solve for the modal coordinate.

$$q_k = \frac{\phi_k{}^T \boldsymbol{M} u(t)}{M_k} \tag{1.12}$$

Therefor every mode's contribution to the measured displacement field $u(t)$ is the summation of m modes multiplied by there modal coordinate q_k.

To implement this technique on various structures, the display requires knowledge of the mass matrix of the structure as well as the mode shapes. Given this information, this method is easily implemented and offers the opportunity to determine other modal contributions to responses as opposed to a general poly fit (which would not contain this type of information). To minimize computational effort of the display interface, pre-multiplication of every mode shape (ϕ_k), mass matrix ($\boldsymbol{M}$), and modal mass (M_k) is stored such that the routine for any modal coordinate is a only 2N operations.

This technique of data regularization has been implemented on Building A. Figure 1.16 shows collected data by the CSN network over the height of the structure for a wind event on Feb 17, 2017. The blue and red dots are the measured data, whereas the green dots represent a summation of 5 modes to fit the data best. The modal fit smoothens the data and provides a more realistic deformation over the height of the structure. Figure 1.17 is a top down view of the structure that shows the noise in the response, as well as how the modal fit creates a more realistic deformed shape of the structure in this low amplitude event.

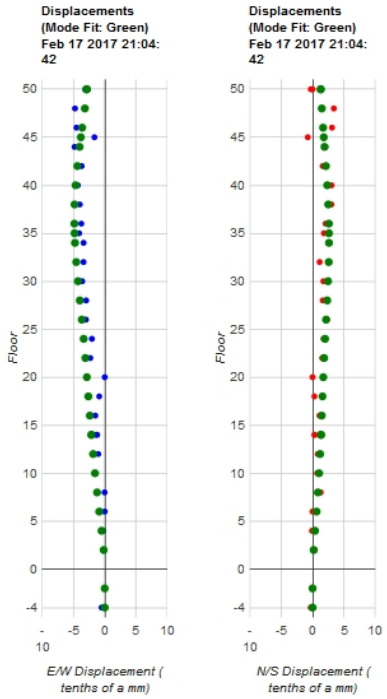

Figure 1.16 *Modal fit of displacement data in during wind event over the height of the structure. Green dots represent the modal fit while blue and red dots show East-West and North-South unfiltered measurements*

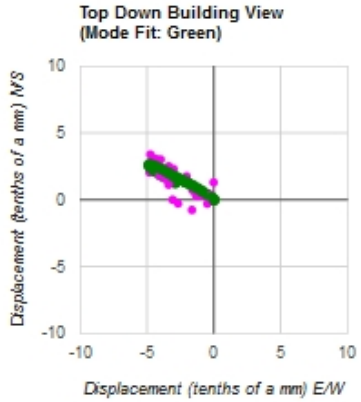

Figure 1.17 *Modal fit of displacement data during wind event from a top-down view. Green dots represent the modal fit while purple dots show the combined East-West and North-South displacements field unfiltered measurements.*

1.7 Blast

This is a summary of work from the paper "Downtown Los Angeles 52-Story High-Rise and Free Field Response to an Oil Refinery Explosion" published in Earthquake Spectra in August of 2016. This will specifically focus on the computational aspects associated with the tools mentioned prior being used to quantify a blast pressure field over the height of Building A.

On February 18th 2015, an ExxonMobil Corp oil refinery station in Torrance California experienced a system failure which led to an explosion. This explosion sent energy into the ground as an elastic seismic energy and into the air as a pressure wave. Even though Building A is 22.8 km from the location of the blast (See Figure 1.18), the CSN team hypothesized that the far field pressure wave resulting from the explosion could be observed in the acceleration data of the tower.

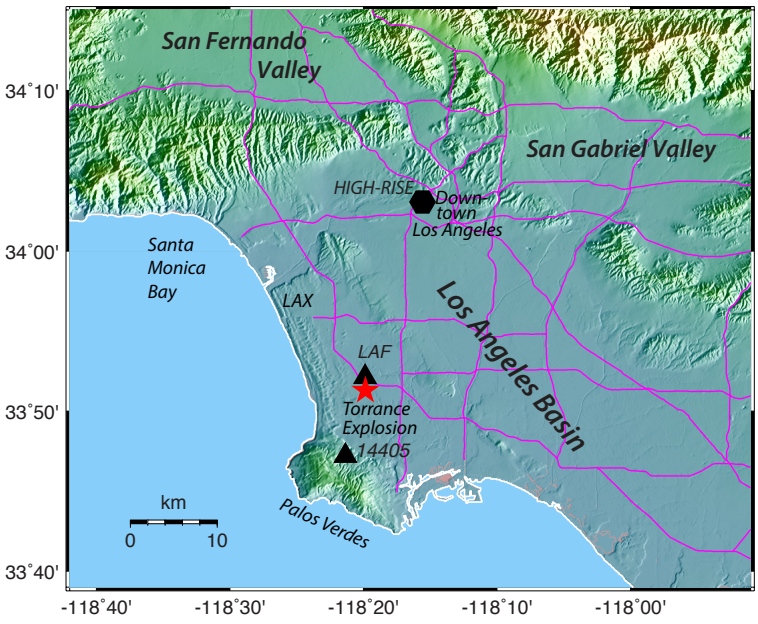

Figure 1.18 Location of blast relative to Building A (Kohler et. al. 2016)

After reviewing the seismograms from Building A, a simultaneous arrival of an anomalous signal was identified which corresponded to an arrival time similar to the speed of sound and distance relative to the source explosion (see Figure 1.19). After filtering, the measurements had peak acceleration amplitudes of 0.02%g and corresponded to a maximum displacement of .03mm. Based on this, an attempt was made to quantify the blast pressure wave over the height of the structure.

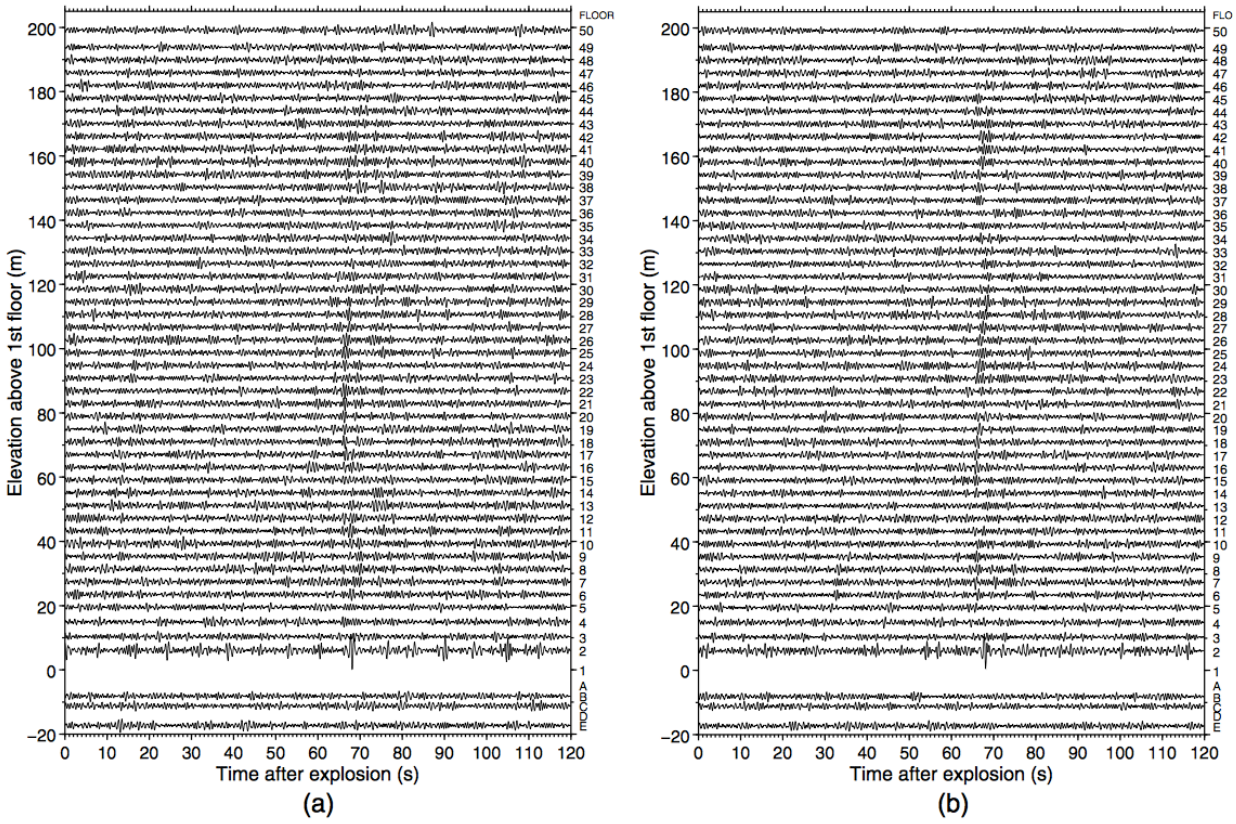

Figure 1.19 Acceleration time series from the north-south (a) and east-west (b) components recorded at Building A in downtown Los Angeles. The simultaneous arrival of the signal at approximately 65s is attributed to the blast wave moving through the city (Kohler et. al. 2016)

We first revisit the general equations of a linear dynamical system

$$\boldsymbol{M}\ddot{u}(t) + \boldsymbol{C}\dot{u}(t) + \boldsymbol{K}u(t) = P(t) \tag{1.13}$$

In this equation, it is assumed that all relative acceleration, velocity, and displacement information is measured from our system, and simply look to determine the vector P(t) over time. To do this, a reduced order model of Building A (as described in Section 1.4.1) was developed to capture the dynamics of the building and work with the measurements directly. The first five mode comparisons of the system were shown in Table 1.2 and have sufficient accuracy to develop the forcing function further in the modal coordinate frame.

Given a well defined stiffness and mass matrices, a Rayleigh damping strategy was implemented to develope the damping matrix.

$$\boldsymbol{C} = a_0\boldsymbol{M} + a_1\boldsymbol{K} \tag{1.14}$$

where a_0 and a_1 were chosen such that the first and fourth natural frequencies of the system had 1% damping.

With the entire dynamic equation defined, a final filtering process was implemented on the recorded data. Due to the low signal amplitude, the signal to noise ratio of the data was quite low; however, a rational pattern of behavior was evident in the collected data set. To resolve some of the signal to noise issues, a modal fit over the spatial domain of the structure was applied to the displacement, velocity, and acceleration data to smooth the signal. This process is identical to what was described in Section 1.6 and the modal fit for the real-time display. For this particular study, the data was spatially filtered with the first five modes of the structure and was found to give a reasonable fit over the portion of the signal of interest (See Figure 1.20).

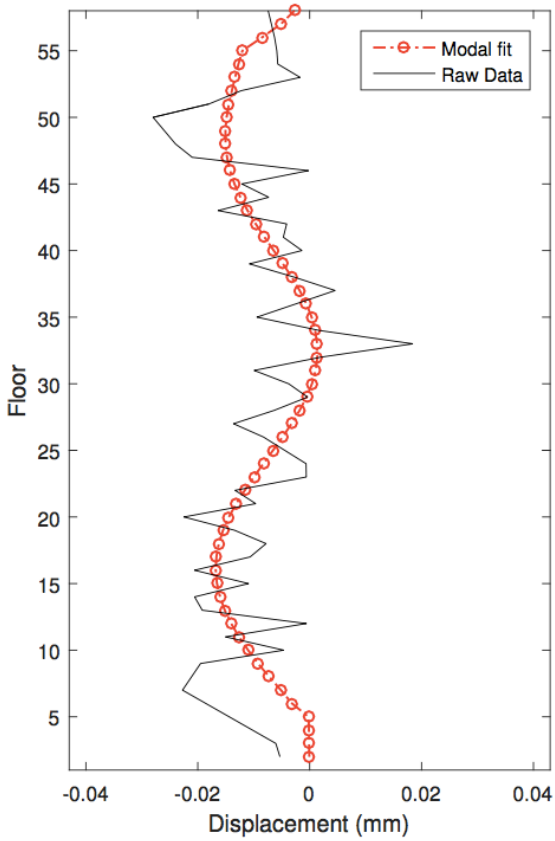

Figure 1.20 Modal fit to the displacement field in the north-south direction during the pressure wave excitation (Kohler et. al. 2016)

With this refined data, the fully formed dynamical system was used to determine the forcing function P(t). The maximum amplitude of this applied force vector on any floor was 1.42 kN (0.32 kips). Distributing this force over the projected area of the floor corresponded to an average pressure of 5.8 Pa.

To better quantify this pressure and relate the fluid dynamics of the problem, we apply Bernoulli's equation, which describes the conservation of energy in fluid mechanics.

$$P_1 + \frac{1}{2}\rho {v_1}^2 + \rho g h_1 = P_2 + \frac{1}{2}\rho {v_2}^2 + \rho g h_2 \tag{1.15}$$

In the case of wind, the kinetic energy of the wind particles is converted directly into a pressure, reducing Eq. 1.15 to

$$\frac{1}{2}\rho {v_1}^2 = P_2 \tag{1.16}$$

Having solved for the pressure P_2 via structural dynamics, we can now solve for the equivalent wind speed of the pressure wave on the building. Assuming standard atmospheric conditions and density of air

$$.591 {v_{m/s}}^2 = P_{pa} \tag{1.17}$$

This resulted in a wind speed of 3.6 m/s (8 mph). This overall methodology was validated for a wind data collected on March 24th of 2015, and was compared with measurements made by an independent weather organization, Wunderderground. In this secondary study, we found agreement between our approach in developing the wind speed for this event. More information on this and the rest of this study can be found in Kohler et. al. 2016.

1.8 Linear Damage Detection Scenario Developments – ETABS Damage Generation Tool

Damage detection in structural health monitoring is the focus of many studies in the research community. Various computational techniques have been explored and developed to ascertain damage from various means and methods. The following is a series of techniques based on linear analysis of structures.

Ideally, a rich database of damaged structures would be available for study of damage detection techniques; however, the practicality of destroying or damaging existing structures and then subjecting

them to some form of input is not feasible. Ergo, it is common practice to develop computational results for testing damage detection strategies.

To facilitate rapid creation of damage scenario data, a tool was developed (in conjunction with Computers and Structures Developer Dr. Christopher Janover) leveraging a computational model developed in the ETABS program to modify stiffness of objects to represent a pseudo damaged structure. These pseudo damaged structures were then run through a series of ground motions for computational study.

Figure 1.21 shows the graphical user interface of the program. The program is developed such that for a series of runs, any group of objects in the model can be modified independently. These modifiers are varied depending on the type of object in the group (whether shell of frame object type). For shell objects, the f11, f22, and f12 modifiers are means of changing the thickness (t) of the shell in terms of in-plane stiffness. The m11, m22, and m12 modify the stiffness terms associated with the cube of the thickness (t^3). For frame objects, the Area, Shear 2 and Shear 3 allow for reduction of the axial stiffness and shear stiffness of the frame object independently. The Torsion, I2, and I3 parameters similarly allow for manipulation for the torsional and bending stiffness about the axis of interest.

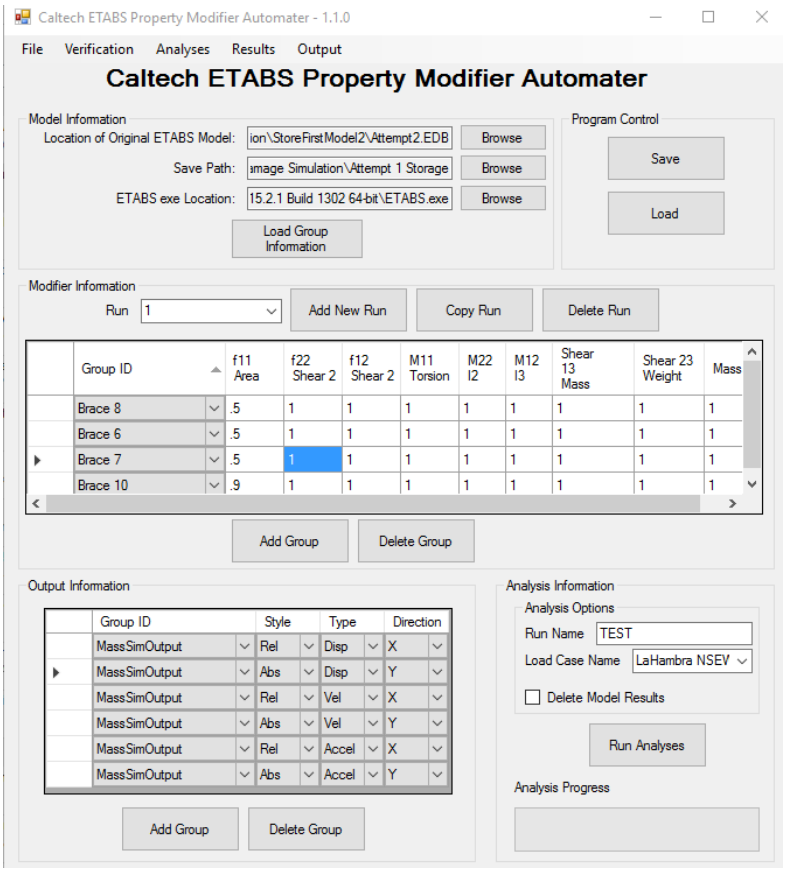

Figure 1.21 Custom software for mass simulation to vary computational properties (Massari et. al. 2017)

Additional control on specific output from simulations is controlled by using group information associated with nodes of interest and the type of output requested. Currently the program only offers deformation information (relative and absolute displacement, velocity and acceleration) for output.

This tool was used to developed a series of damage scenarios used in studies to be mentioned using Building A. These scenarios are shown in Table 1.7. In all current cases, the manipulation of brace type of brace type objects was made by lowering the axial stiffness of the section. These reductions were meant to represent various levels of brace buckling and/or gusset damage after a significant event. This data is available for use in future studies and is the backbone of a series of studies to be presented.

Damage Scenarios	Floor Levels Damaged-(set max to 5)					Residual Stiffness	Localization
1	20	21	22	23	24	0.001	Large Multi Story Mechanicsm
2	25	26	27	28	29	0.001	
3	30	31	32	33	34	0.001	
4	35	36	37	38	39	0.001	
5	40	41	42	43	44	0.001	
6	20	21	22	23	24	0.1	
7	25	26	27	28	29	0.1	
8	30	31	32	33	34	0.1	
9	35	36	37	38	39	0.1	
10	40	41	42	43	44	0.1	
11	20	21	22	23	24	0.5	
12	25	26	27	28	29	0.5	
13	30	31	32	33	34	0.5	
14	35	36	37	38	39	0.5	
15	40	41	42	43	44	0.5	
16	20	21	22	23	24	0.8	
17	25	26	27	28	29	0.8	
18	30	31	32	33	34	0.8	
19	35	36	37	38	39	0.8	
20	40	41	42	43	44	0.8	
21	20	21				0.001	2 story Mechanisms
22	30	31				0.001	
23	40	41				0.001	
24	20	21				0.1	
25	30	31				0.1	
26	40	41				0.1	
27	20	21				0.5	
28	30	31				0.5	
29	40	41				0.5	
30	20	21				0.8	
31	30	31				0.8	
32	40	41				0.8	
33	25					0.001	Single Story Mecahnisms
34	35					0.001	
35	45					0.001	
36	25					0.1	
37	35					0.1	
38	45					0.1	
39	25					0.5	
40	35					0.5	
41	45					0.5	
42	25					0.8	
43	35					0.8	
44	45					0.8	
45	25	45				0.001	Spreadout Damage
46	25	35				0.001	
47	25	45				0.1	
48	25	35				0.1	
49	25	45				0.5	
50	25	35				0.5	
51	25	45				0.8	
52	25	35				0.8	
53	25	45				.001/.0005	Varried Damage States
54	25	45				.0005/0.001	
55	25	45				.1/.05	
56	25	45				.05/.1	
57	25	45				.5/.25	
58	25	45				.25/.5	
59	25	45				.8/.4	
60	25	45				.4/.8	

Table 1.7 Damage scenario data created by simulation tool

1.9 Damage detection techniques

Dense instrumentation offers a unique opportunity to assess traveling wave phenomena through buildings at a very high resolution. The following is a sample of previous and ongoing work making use of these types on new observations that set the stage for more techniques to be developed.

1.9.1 Radon Transform

With dense instrumentation, clear variations in wave propagation are often observable when there is significant impedance introduced to a structure. These variations (or reflections) become less and less obvious when the level of damage is reduced. Figure 1.22 shows the response of a structure where damage is isolated to one floor, but where the level of reduction in stiffness is continuously reduced. Observe that this reflection is always present; however, the reduction in damage results in a lower amplitude reflected wave. With this in mind, techniques of evaluating waveforms over the height of a structure are of interest, with the particular goal of isolating damage locations via imaging techniques.

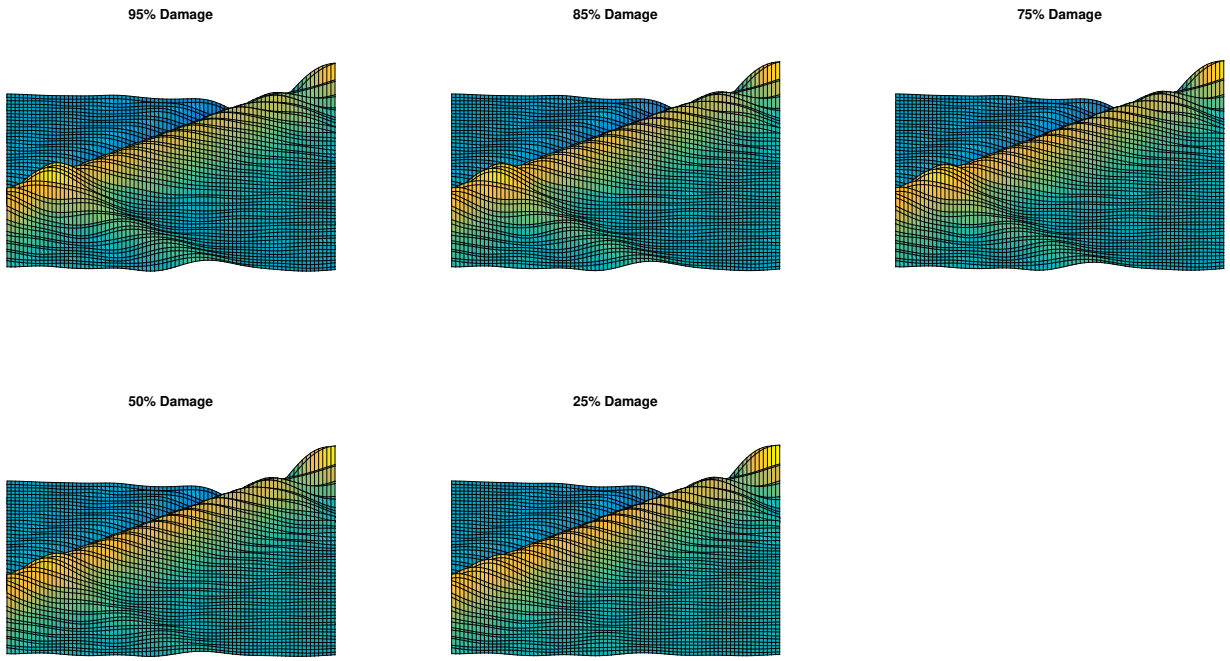

Figure 1.22 Varied damage levels by reducing floor level effective stiffness show reflections of varied amplitude in the down-going wave. This shows how larger levels of imparted damage increase the reflected energy

One technique explored was inspired by methods used in medical imaging that also uses changes in impedance of wave forms to create images of structure. Radon transforms are a technique for

measuring impedance within a body when direct measurements can not be made. This transform integrates a three-dimensional space ($f(x,y)$) via a defined path of straight lines (S). For a given line S, the radon transform $R(S)$ is given by

$$R(S) = \int_S f(x,y) \tag{1.18}$$

Seismograms from each individual level are used to form $f(x,y)$, where x is time and y is floor elevation and the functional value is the amplitude of the seismogram. The sequence of integration lines S are defined such that they span the space of the image at angles which are representative of rational slowness (μ). These slowness values values are plotted relative to the image centerline to construct the radon transform image R(t, μ). This radon image (R(t, μ)) can be compared for damaged vs undamaged structure (See Figure 1.23). The introduction of damage in the general function $\mathrm{f(x,y)}$ creates a series of reflections that create variations in the transform itself. These variations in slowness and the patterns observed in the higher velocity reflections are one such way dense instrumentation data can be used to detect variations in damage.

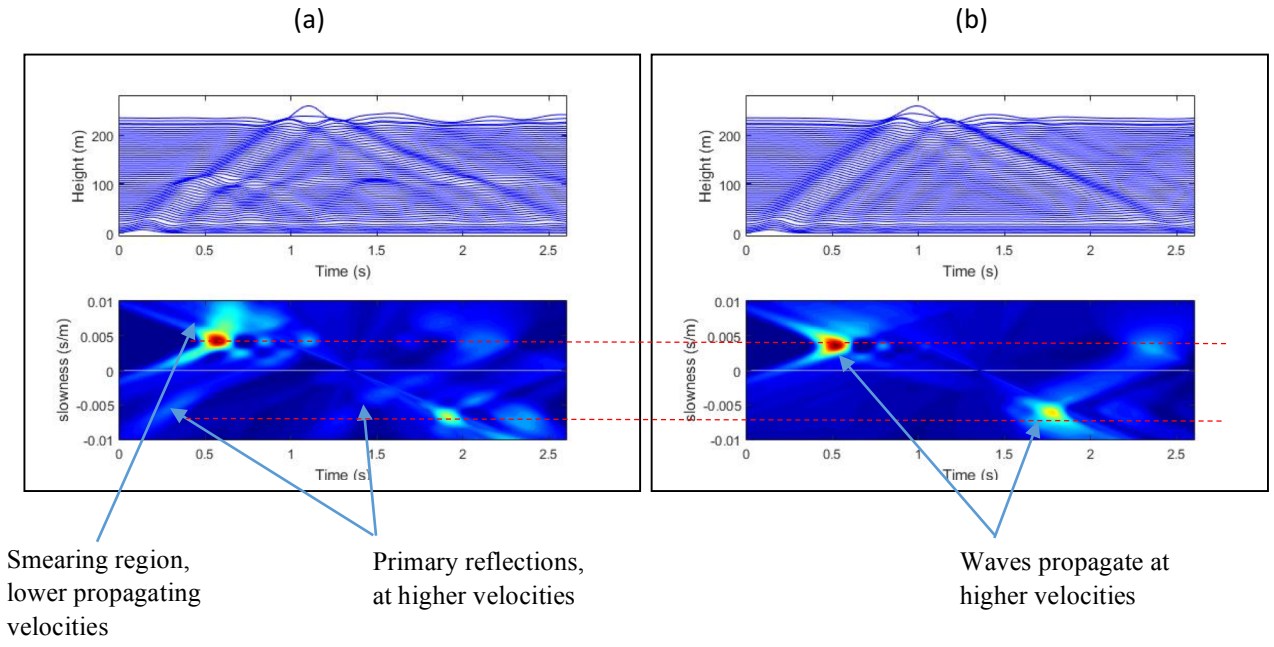

Figure 1.23 Radon transform of displacement data collected from a damaged (a) and undamaged (b) finite element model of a 52-story building subjected to a Gaussian input (Massari et. al. 2017).

While this transform method offers potential in damage detection, it is used as inspiration for a more direct method of determining where and when damage may occur in a structure. Knowing that these reflections exist and that integration along various angles create variations in the radon image of the structural response, a more refined method is presented later.

The radon transform indicates that a majority of the information available about the reflections and variations in overall amplitude of the image center about the slowness of the structure that the primary wave travels. This offers insight into the reflected wave structure and inspires us to instead search for specific line integrations which match the reflected information propagates.

1.9.2 Template Matching

Treating damage/impedance contrast as a potential scatterer of a wave, the following is a technique using template matching to isolate reflections within a structure. When a wave travels through a body and reaches an impedance, there is a transference of the wave through the impedance and a reflection due to the slowing of the wave itself (see Figure 1.22). This is well understood from general wave mechanics. This reflected wave and the slowing of the upward-going wave offer an opportunity for a unique signature in a wave form.

Figure 1.24(a) and (b) shows a minimally damaged and undamaged structure response with a broadband Gaussian input at the base. When the level of damage is low, it is difficult to observe the difference between these two structures. However, if one subtracts the undamaged case from the damaged case, a clear image of a reflected wave at the location of damage (Figure 1.24(c)), as well as a variation in behavior of the up going wave can be observed. This characteristic signal source appears to be from the location of damage and gives inspiration for a new technique in damage detection.

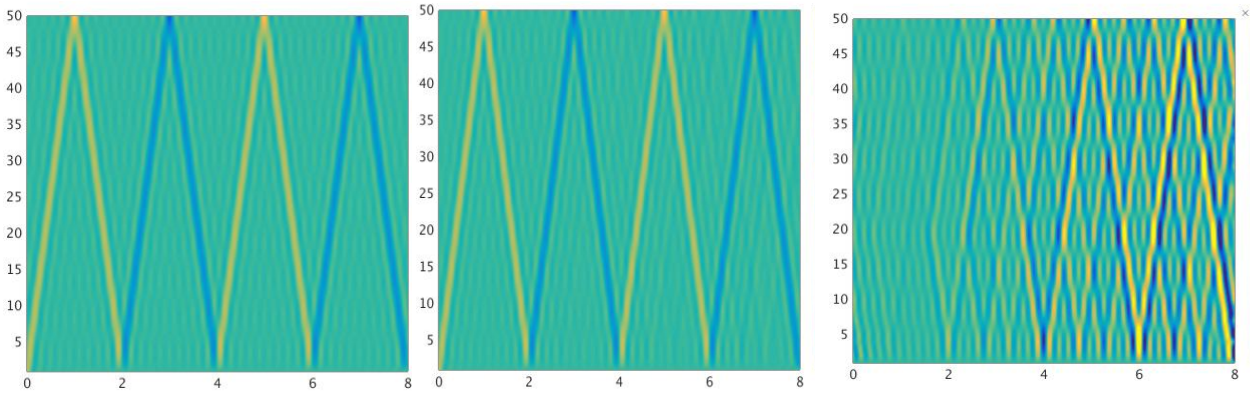

(a) (b) (c)

Figure 1.24 Undamaged(a), damaged(b), and difference(c) of Gaussian input to Building A. [correspondence with Clayton 2015]

Consider the damage location as a source from which acceleration information is propagated throughout the structure and received at various locations. If that source were a true delta function, the receiver responses to that source would be the Greens functions of the structure relative to the initial source.

While the reflected wave itself is not a Greens function, its trajectory through the structure has similar content, albeit over a less robust frequency domain. This similar content is the rational approach of the presented strategy. If Greens functions where available throughout the structure between every potential source of damage and a receiver array throughout the system, they could be used to match with reflected waves to determine if a correlation was present. In a physical model, creating all the potential Greens functions for every possible damage location would be a daunting task; however, in a computational framework, the work is relatively straightforward.

For Building A and Building B, synthetic Greens functions were computed for every foreseen damage location in the structure of interest. These locations included brace, weld, and truss component failures. At each joint/location where a damage location of interest was considered, an impulse function was applied to the structure and responses were measured where CSN array data was, or will soon be collected. These locations are shown in Figure 1.25 and Figure **1.26**, as well as the location of receivers/sensors. The responses represent the Greens functions of the structure throughout the system, and when used for every receiver for a particular damage location, make up a single damage template of the structure (See Figure 1.27 for a selection of Building A templates). For Building A this corresponded to 588 templates and for Building B 192 templates.

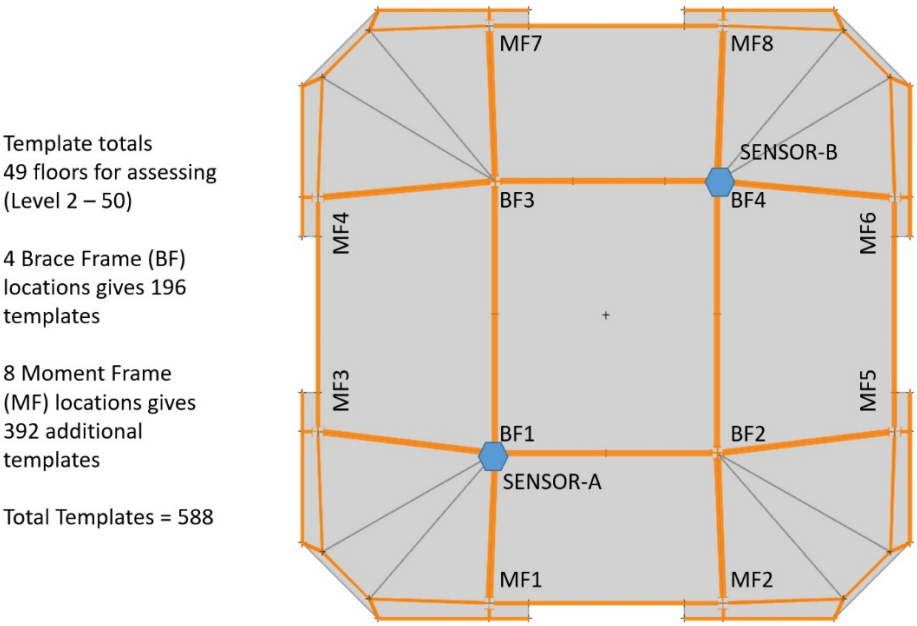

Figure 1.25 Building A sensor and damage Locations

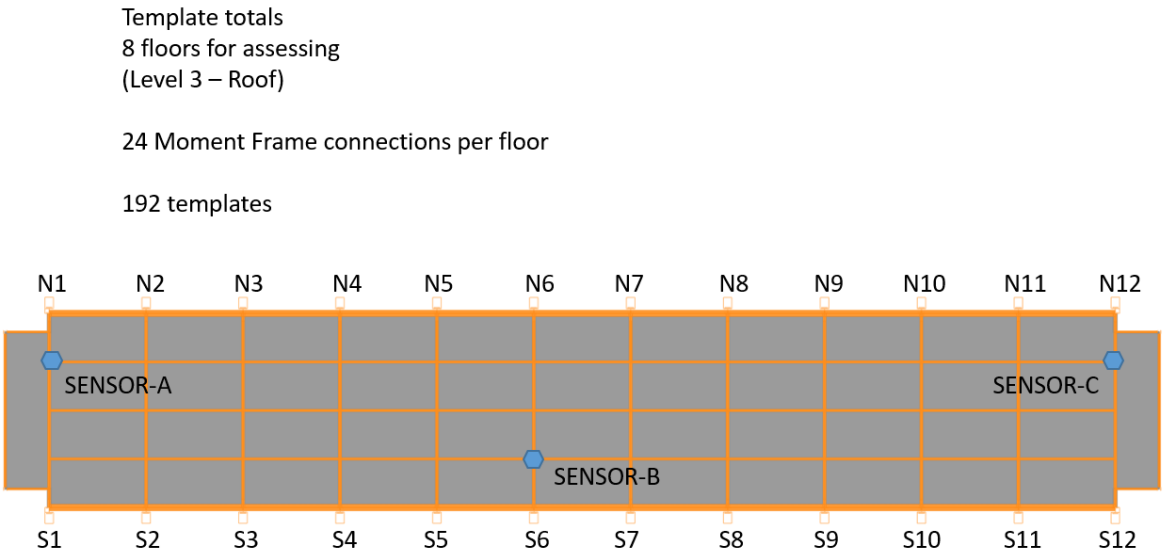

Figure 1.26 Building B sensor and damage locations

Each template represents a computational response to an impulse function applied at each source or damage location of the undamaged model. From the source, one can observe an outward response between floors that represents the traveling waves through the structure to the set of distributed

receivers. These templates very closely resemble the reflected wave pattern of a traveling wave through a damaged structure (Figure 1.24). This characteristic is enhanced when the damaged response is subtracted from the undamaged response. This characteristic is what we seek to isolate in our template matching strategy.

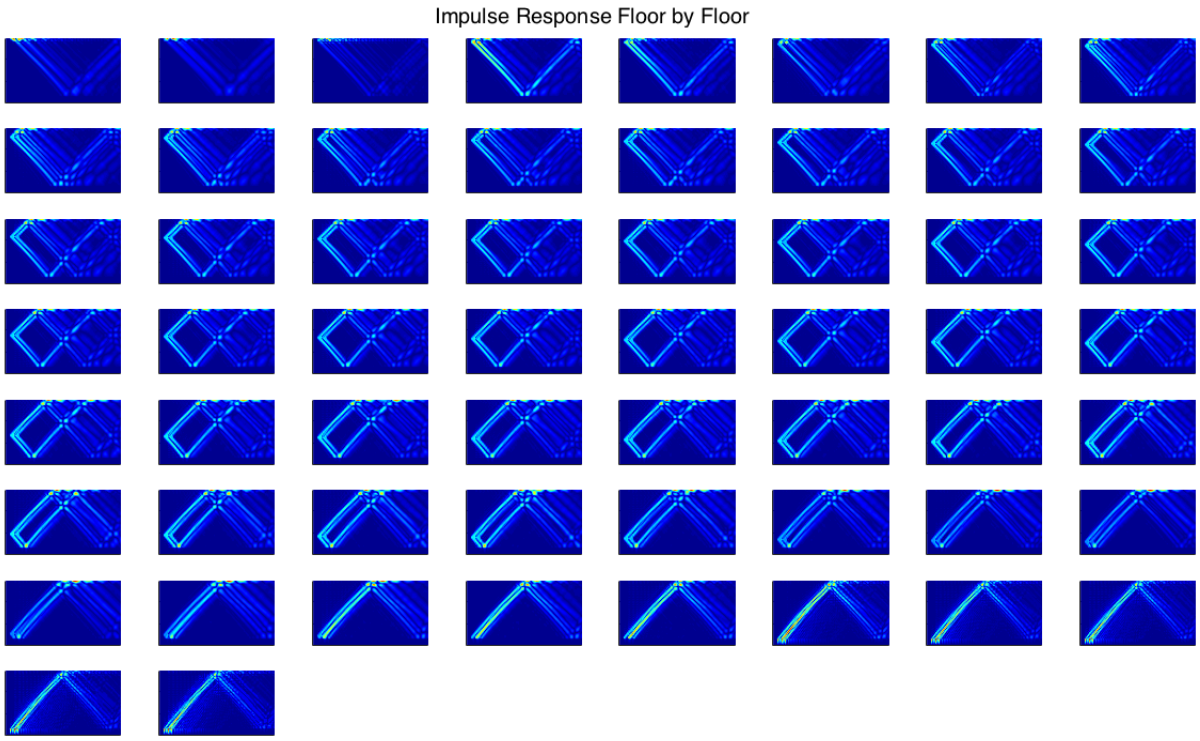

Figure 1.27 Building A impulse response plots for BF4 at Sensor-B

The templates themselves are unique and offer orthogonality characteristics. This can be observed by simply taking any template pair and correlating them with each other in the time domain (See Figure 1.28 and Figure 1.29). The banded nature of the correlations indicate that damage templates are less correlated with floors that are geometrically farther away (floor to floor). This lack of correlation is critical to successfully using template matching as a method to assess the location of damage. The orthogonality of the set of templates enables us to isolate correlations along the band, translating to a stronger ability to pin-point damage.

In Building A, we show only the correlations between the BF4 (Figure 1.25) over the height of the structure measured at Sensor A for clarity (Figure 1.28). The diagonally banded nature of this correlation demonstrates the relative orthogonality of one template from another.

In Building B, we show a similar correlation of all the templates on each floor and further separate into X and Y components (Figure 1.29). As a results we see a similar banded structure, but with greater width then observed in Building A. Enhancing level 7 Y-direction only correlations (Figure 1.30), we observe the correlation between co-linear damage sources on opposite sides of the building. This explains the increased width of the band and correlation in the Y-direction. The main reason for this increase is that there is not full coupling due to the torsion aspects of the narrow building structure. This suggests that resolution of the damage may be restricted to a particular gridline as opposed to a precise location (due to the coherence of templates along any North-South gridline). Similarly, in the X-direction we see very similar correlations for all the sensors on the same floor level. This is due to the rigidity of the structure in the East-West direction and the minimal amounts of torsion experienced.

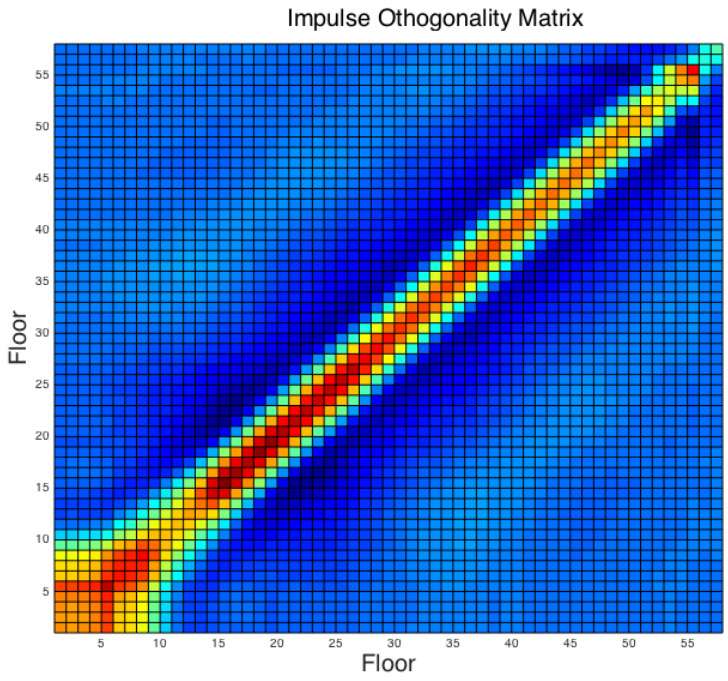

Figure 1.28 Building A Sensor-A template correlations over height of building for damage at location BF4

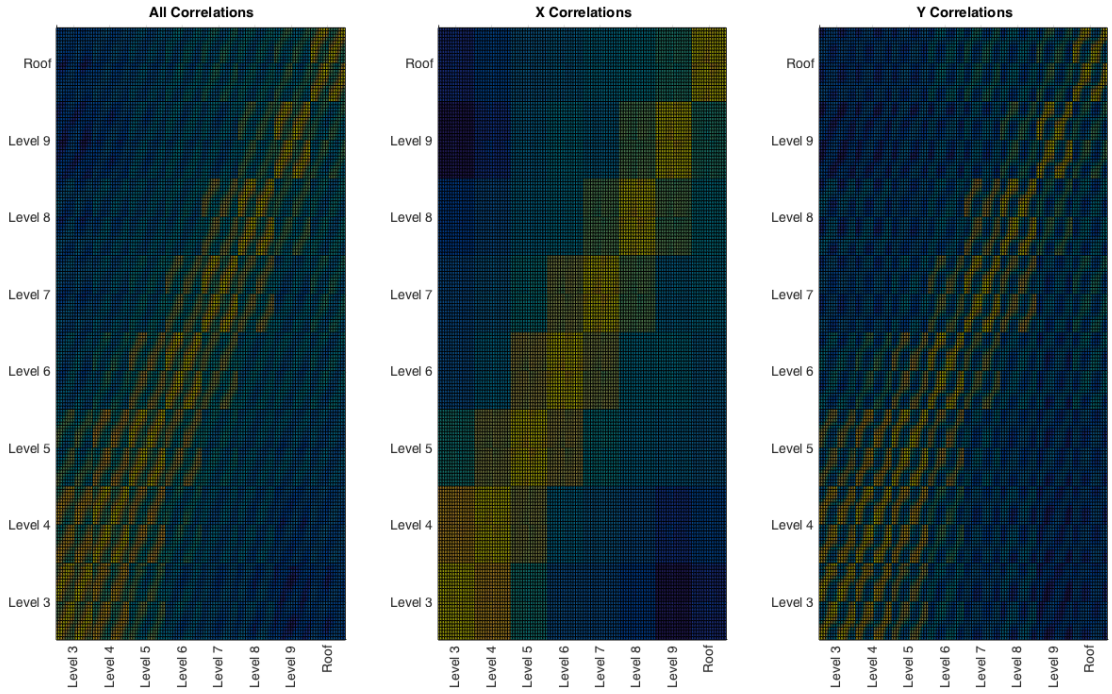

Figure 1.29 Building B all template correlations. Of note is the banded nature and torsional effects on the overall correlation images in the Y-direction correlations

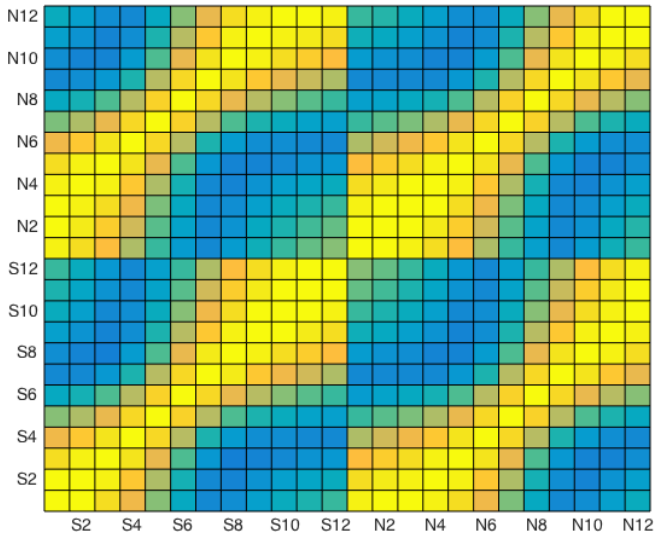

Figure 1.30 Building B enhanced 7th floor only correlations in Y-direction

1.9.2a Examples in Building A

Building A's relative stiffness of braced core to moment frame suggests a precursor to further damage that would result from initial brace damage (as was seen in Section 1.5). As such, all damage

studies presented for Building A will be based on a reduction in stiffness of the brace axial degree of freedom to mimic a post yielded/buckled frame or softened connection damage state.

For Building A, all of the 588 templates are correlated to the simulated response of the structure at every receiver and the value of correlation is stored for each unique location. Figure 1.31 shows an example of these correlations over the height of the building for every distinct location of damage for a model where damage was introduced at the 35th floor. These correlations were computer for the precise time when the reflected wave reaches the damage location. While it is clear that there is a strong correlation at level 35, it is visually not clear whether the maximum correlation is there or at any of the nearest neighbors. To increase the clarity of these correlation results, integration of all the template corellations at a particular level is performed. This offers a single response at a floor by floor level and consistently creates a more obvious location of peak response (See Figure 1.32). This strategy is implemented throughout the subsequent results for Building A.

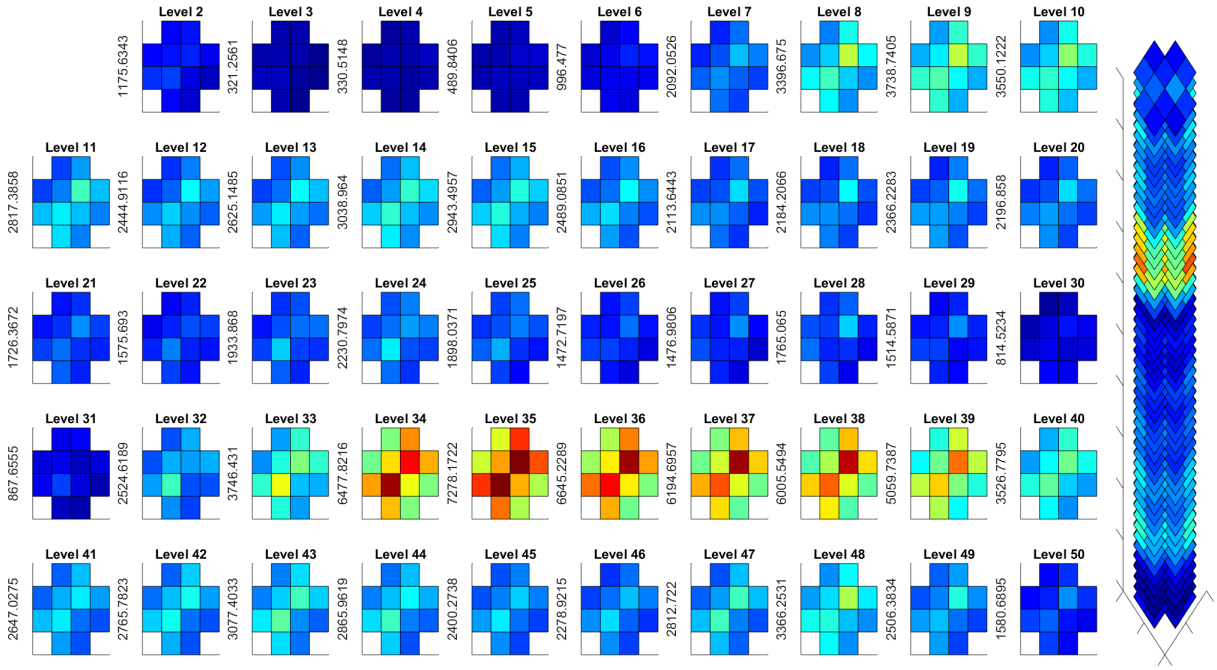

Figure 1.31 Damage correlation of every template at level 35 at time of reflection with every floor instrumented with no noise

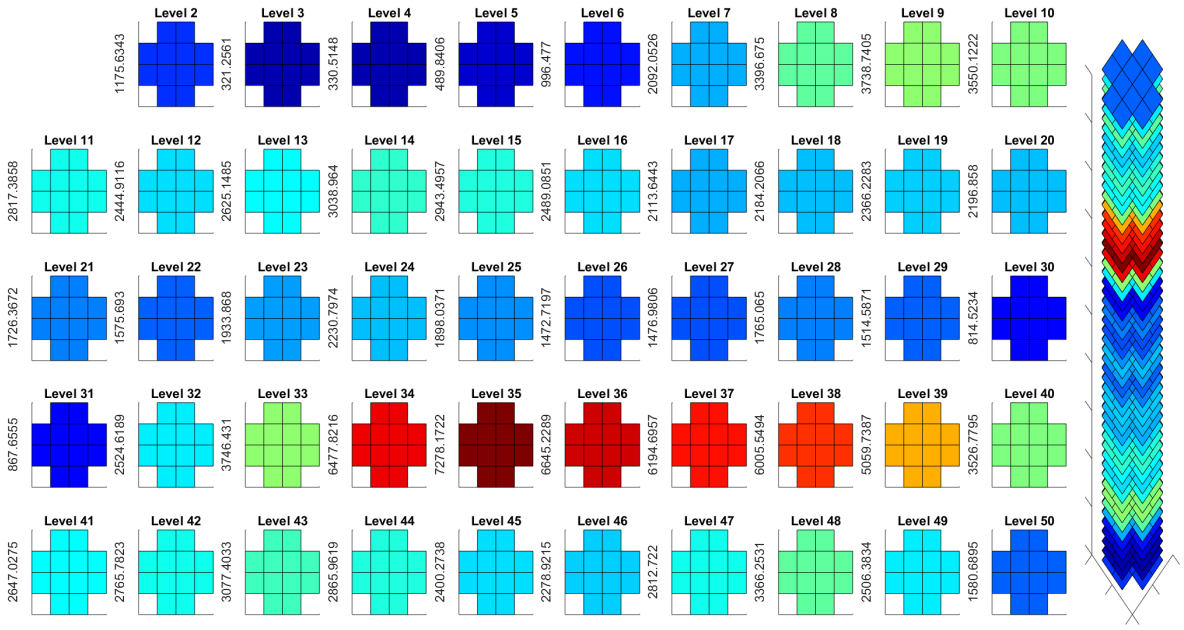

Figure 1.32 Damage correlation of every template summed at the floor level creates a clearer image with every floor instrumented with no noise

Using this floor level integration of correlations, we then explore a series of damage scenarios, amplitudes of damage, numbers of sensors and noise levels. Table 1.8 explains all the studied damage scenarios. In all cases damage was introduced by selecting all brace levels at the floor level of interest and changing the axial stiffness modifier to 75% of its original stiffness. Damage scenario 1 will be presented in detail, while other scenarios will be part of a paper currently in development.

Damage Scenario Information

Scenario	Damage applied
1	Level 35 reduced to 75% of its area
2	Level 35 and 20 reduced to 75% of its area
3	Level 35 through 33 reduced to 75% of its area
4	Level 20 reduced to 75% of its area
5	Level 25 reduced to 75% of its area

Table 1.8 Building A damage scenarios used for template matching study

The correlations shown previously were done at a specific instance of time where the correlation would be strongest at the floor of interest for demonstration purposes. However, at any point in time, a subsequent template might have a larger correlation than the damage location of interest. This is observed in Figure 1.33. Here we see that every template has a point in time where its correlation is

largest; however, there is an overall stronger correlation of the up-going waves that intersects the peak correlation. To account for this, all templates are shifted in time such that the initial arrival time of the up-going wave matches the initiation of the Greens function templates. This shifting in the time domain gives increased weight to lower correlation templates, but more accurately represents the correlation amplitude relative to other templates.

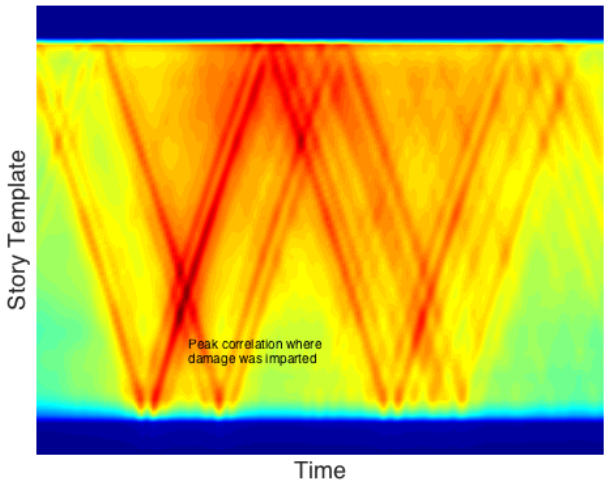

Figure 1.33 Correlation of templates over time

Using Damage Scenario 1, we first investigate the variation in total number of sensors used in this template matching scheme. Figure 1.34 shows the correlation image for sensors at every 1, 2, 5, 10 and 20 floors and how it effects the correlation image. While the image is promising in most of the cases (except for 20 floor separation), it does not reflect more realistic conditions where noise is added to the system. If we add white nose with an amplitude of 10% of the peak amplitude of response, the image becomes distorted (See Figure 1.35).

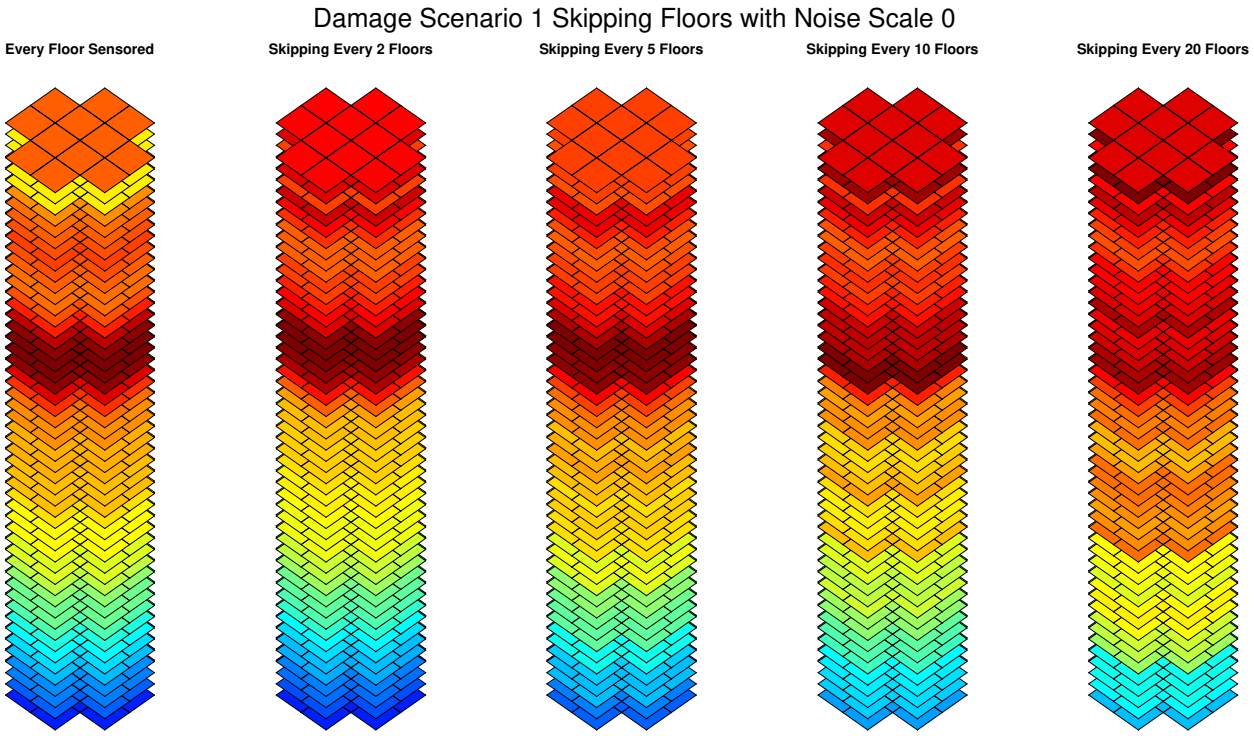

Figure 1.34 Damage scenario 1 with no noise skipping floor levels

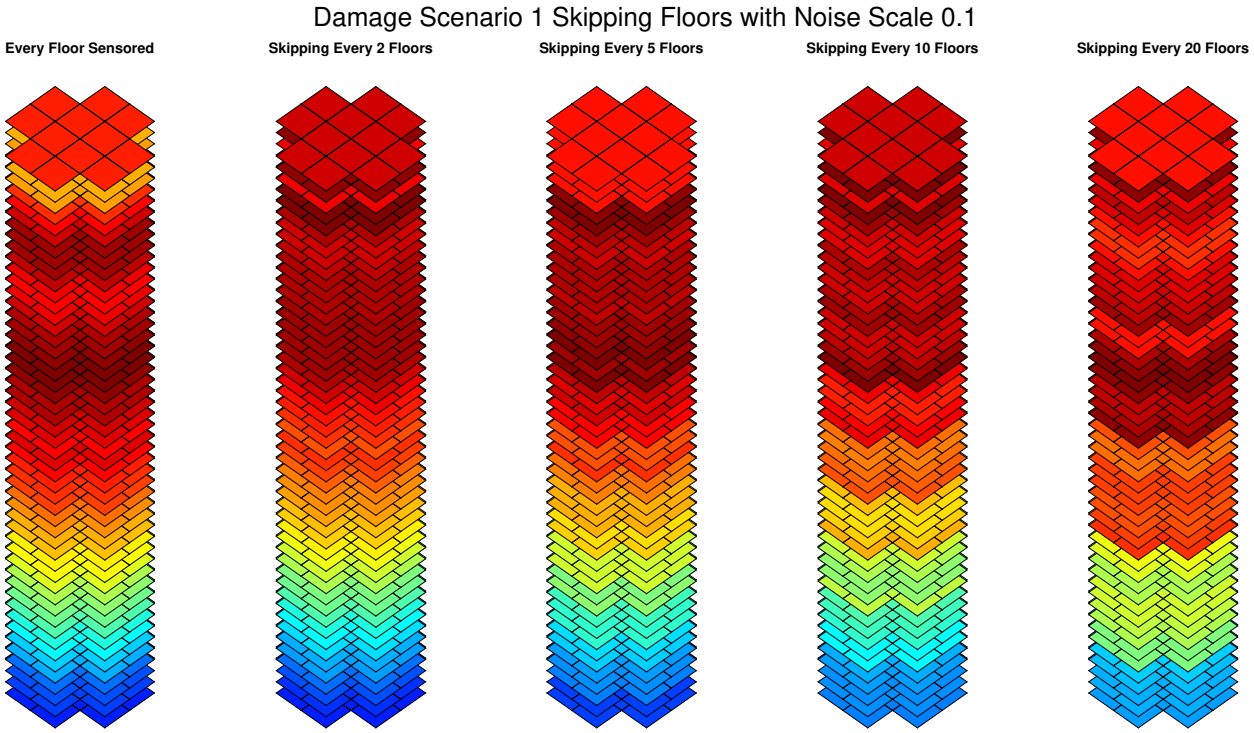

Figure 1.35 Damage scenario 1 with 10% noise added

1.9.2b Examples in Building B

For Building B, a similar study was conducted where damage was placed between the 6th and 7th floor of the structure (bottom flange of trusses), but at different bays and in different directions (See Table 1.9). The torsional aspects of Building B (being long and slender) allow for the potential localization to be determined at a more spatially refined level.

Damage Scenario Information

Scenario	Damage applied
1	Location S6 in the X direction
2	Location S6 in the Y direction
3	Location S3 in the X direction
4	Location S3 in the Y direction

Table 1.9 Building B damage scenarios used for template matching study

Figure 1.36 shows each correlation separately for the 4 damage scenarios. For damage scenarios 1 and 3 (X-direction damage), there appears to be a stronger correlation with damage location than in scenarios 2 and 4 (Y-direction damage). Upon deeper analysis, we see less pronounced correlation when the damage was placed further away from the center of the structure (scenarios 3 and 4).

Even more revealing is when correlation in the X and Y directions are separated (See Figure 1.37 and Figure **1.38**). While it is clear that damage was introduced near the 6th floor in the X-only correlations, it would be difficult to determine at what particular location. However, in the Y-only correlations, the strength in the torsional component of the scenario indicates along which potential gridline there may in fact be damage.

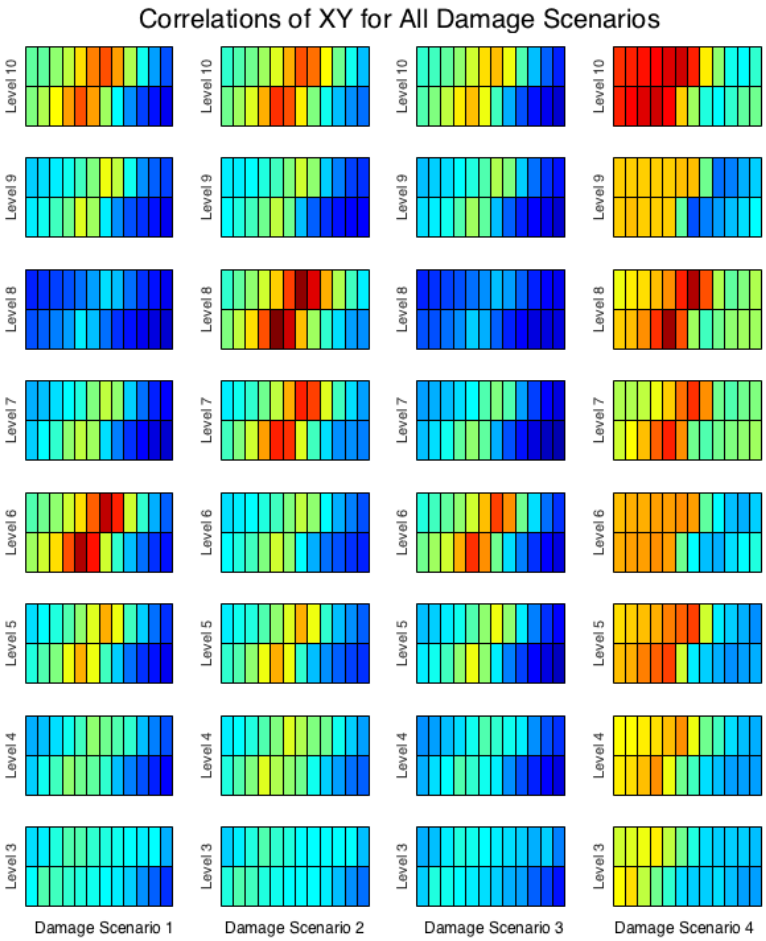

Figure 1.36 Correlations in X and Y directions summed together for all Building B damage scenarios

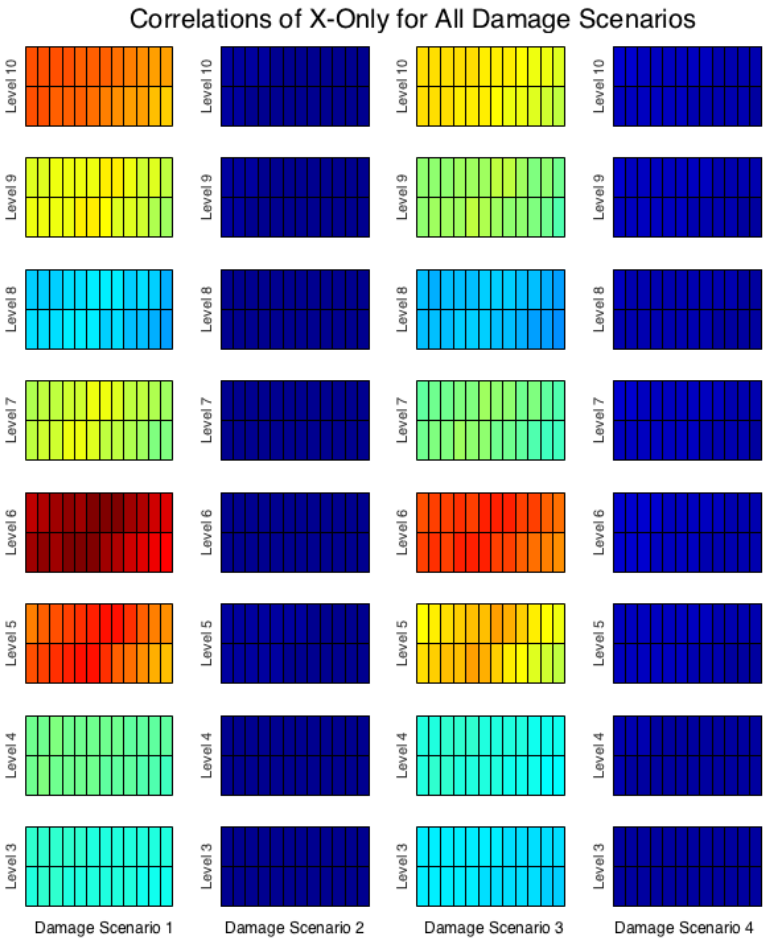

Figure 1.37 X-only correlations for all Building B damage scenarios

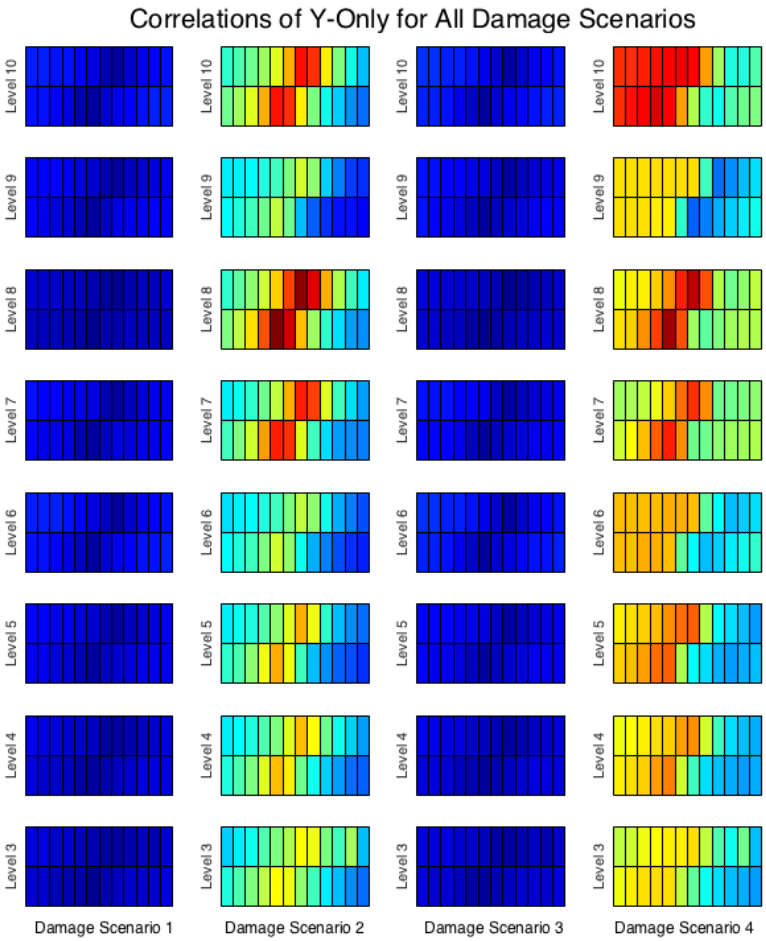

Figure 1.38 Y-only correlations for all Building B damage scenarios

1.10 Conclusion

Dense structural instrumentation is paving the way for new technologies and methodologies in civil engineering. The development of tools to process and evaluate measured responses and learn potential means and methods that are most feasible is critical to being prepared for the future of infrastructure. Put forth were a series of computational developments exploring these new rich data sets.

Reduced order models are key to working with collected data and inverting for potential solutions. By means of computational static condensation, complex structures can be reduced to the measured dynamic degrees of freedom to create a linear system that is more manageable from the scale of a city-

wide evaluation. These types of reduced order dynamic models can be used to solve various forms of problems, such as the blast pressure wave discussed.

To help advance assessing new analytical techniques, a database of damaged computational models was developed as a test bed for innovative ideas. Additionally, a tool for rapidly making more computational damage scenario data was co-developed in an effort to increase this database for future needs and new structures. The data from these analyses is already being used by other researchers to implement new potential forms of damage detection. Internal to Caltech, we have used this for wave propagation techniques associated with template matching and radon transform methods. These methods offer promise, and will be developed further in future work.

1.11 References

Cruz, C., Miranda, E., Damping Ratios in Tall Buildings Inferred from Seismic Records Obtained in Instrumented Buildings in California, *Los Angeles Tall Buildings Structural Design Council*, Proceedings of the 2017 Annual Meeting, pg. 65-80, 2017

Xiang, Y., Harris, A., Naiem, F., Zareian, F., Identification and Validation of Natural Periods and Modal Damping Ratios for Seismic Design and Building Code, *Los Angeles Tall Buildings Structural Design Council*, Proceedings of the 2017 Annual Meeting, pg. 81-97, 2017

Hutt, B., et al., Instrumentation Guidelines for the Advanced National Seismic System, <https://earthquake.usgs.gov/monitoring/anss/docs/ANSS_WGD_InstrGuideline_June2007.pdf> *USGS,* 2007

New York City Department of Buildings, New York façade Ordinance – Façade Inspection Safety Program <http://www.facadeordinance.com/facade-ordinances/new-york>

Moehle, J., et al., PEER/ATC-72-1 Modeling and Acceptance Criteria for Seismic Design and analysis of Tall Buildings, *Applied Technology Council*, 2010

Lin, K., Wald, D., Turner, L., ShakeCast User Guide (Draft), *U. S. Geological Survey*, 2017

Worden, C.B., Wald, D., ShakeMap Manual Online Technical Manual, User's Guide, and Software Guide, *U. S. Geological Survey*, usgs.github.io/shakemap. DOI: 10.5066/F7D21VPQ., 2016

Taghavi, S., Miranda, E., Response Assessment of Nonstructural Building Elements, *Pacific Earthquake Engineering Research Center*, PEER 2003/05 ,2003

Los Angeles Department of Buildings, Structural Monitoring Equipment in Buildings Design with Nonlinear Response History Procedure (LABC 1613.10.2), *Department of Building and Safety*, 2014

ETABS, Analysis Reference Manual Computers and Structures, Inc., Berkeley, CA*, www.csi.berkeley.com,* 2016

Clayton, R., Heaton, T., Chandy, M., Krause, A., Kohler, M., Bunn, J., Guy, R., Olson, M., Faulkner, M., Cheng, M., Strand, L., Chandy, R., Obenshain, D., Liu, A., and Aivazis, M., Community Seismic Network, *Annals of Geophysics 54*, doi: 10.4401/ag-5269., 2011

Clayton, R. W., Heaton, T., Kohler, M., Chandy, M., Guy, R., and Bunn, J., Community Seismic Network: A dense array to sense earthquake strong motions, *Seis. Res. Lett*. 86, 1354–1363, doi: 10.1785/0220150094., 2015

Kohler, M. D., Heaton, T. H., and Cheng, M. H., The Community Seismic Network and Quake-Catcher Network: Enabling structural health monitoring through instrumentation by community participants, *Proceedings of the SPIE Smart Structures/Non-destructive Evaluation Conference*, 10–14 March 2013, San Diego, CA., 2013

Kohler, M. D., Heaton, T. H., Cheng, M. H., and Singh, P., Structural health monitoring through dense instrumentation by community participants: The Community Seismic Network and Quake-Catcher Network, *10th U.S. National Conference on Earthquake Engineering (NC10EE)*, 21–25 July 2014, Anchorage, AK. 2014

Kohler, M. D., Massari, A., et al., Downtown Los Angeles 52-Story High-Rise and Free-Field Response to an Oil Refinery Explosion, *Earthquake Spectra*, Volume 32, No. 3, pages 1793–1820, August 2016; *Earthquake Engineering Research Institute* 2016

Bradford, S. C., Time-frequency analysis of systems with changing dynamic properties. Dissertation (Ph.D.), California Institute of Technology, 2007

Clayton, R W., Heaton, T., Kohler, M., Chandy, M., Guy, R., Bunn, J. Community Seismic Network: A Dense Array to Sense Earthquake Strong Motion., *Seismological Research Letters*, 86 (5). pp. 1354-1363. ISSN 0895-0695., 2015

SAC Joint Venture, Recommended Seismic Design Criteria for New Steel Moment-Frame Buildings, *Federal Emergency Management Agency*, FEMA 350, 2000

Chapter 2

IMPLEMENTATION OF VISCOUS CAPPED DAMPING IN BRACED FRAME BUILDINGS

2.0 Introduction

Prior to recent years, most dynamic analyses were done linearly, and nonlinear responses were estimated by magnifying the linear response by inelastic coefficients (ASCE 7, 2010). However, with the increase in computational power and speed, nonlinear analysis is coming more to the forefront of industry. Further, the increased reliance on performance based design in determining the resilience of structures in the built environment has led to a shift in the paradigm of engineering building structures, with nonlinear analyses becoming the standard of practice for significant structures in hazard prone regions.

Damping in inelastic systems is a complex field of study that is often simplified mathematically in convenient ways to either create a suitable solutions strategy, or to mitigate certain concerns in developing response time histories. Engineers often reason through structures dynamically in the modal coordinate frame, and proceed to construct a damping matrix to achieve a prescribed level of damping in each mode. Rayleigh, Modal, and Caughey damping models are among the more recognized linear methods involving stiffness and mass proportioning; however, other linear models for damping exist.

The shift from linear to nonlinear analysis has increased research into more elaborate elements, more realistic nonlinear geometric methods, and more robust solutions. In developing many of these solutions, the effect of damping on the overall nonlinear response has frequently been a source of contention. Studies have shown that there are certain constraints and issues with the use of linear damping matrices in nonlinear analysis ((Hall J. F., 2006) (Charney, 2008) (Hardyneic, 2015)) that need to be monitored closely. Hall introduced the use of a capped damping element as a remedy to many concerns associated with linear damping strategies, which is studied and implemented in this research. Other long standing nonlinear damping strategies typically use various forms of tangent stiffness matrices in developing the damping model. These tangent stiffness matrices have issues onto themselves which will be addressed briefly.

Presented here is an implementation of a series of damping schemes for a braced frame structure using Perform 3D, an industry standard platform for performance base design. We highlight how the use of various damping schemes affects the performance of a modern 6 story braced frame building (See Figure 2.1). To better understand where energy is stored or dissipated in the system, particular care was taken to observe the variations in force distribution over time. Additionally, work was done to curtail the properties of capped viscous dampers in order to understand how sensitive the analysis results were to this unique parameter.

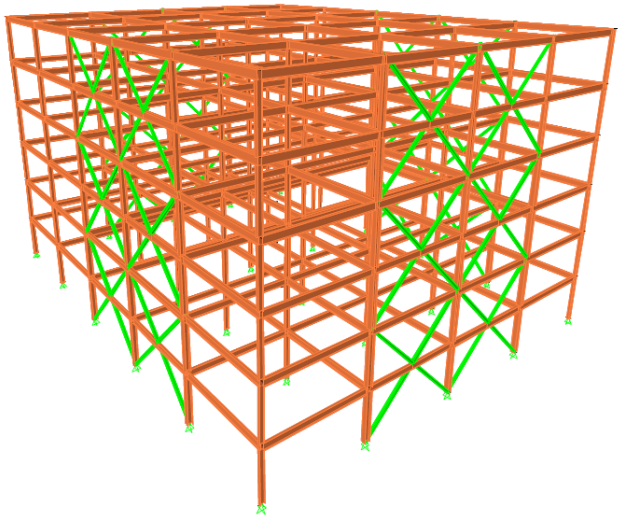

Figure 2.1 ETABS model of a 6 story braced frame structure used in this study. More information on this model can be found in Appendix B.

2.1 Various Damping Strategies

Damping is a complicated component of analysis in a structural system that is often difficult to computationally define from physical parameters. This has led to simplified mathematical interpretations of physical damping components being implemented in many finite element codes. In particular, the Rayleigh and Modal damping methods are often implemented in commercial software used by engineers to investigate the nonlinear performance of structures. Both methods have strengths and weaknesses that will be discussed in detail later in this paper. However, one shared weakness involves how they provide very large damping restoring forces in highly nonlinear conditions. In particular, most nonlinear responses are meant to dissipate a majority of the energy through hysteretic response of elements; however, during these nonlinear excursions relative velocities tend to significantly increase the viscous damping forces in the system (Hall J. F., 2006). These forces have a stabilizing effect which needs to be monitored and understood.

One of the most elementary and common means of implementing damping in an analysis is the Rayleigh damping matrix. The Rayleigh damping matrix is constructed by summing relative quantities of the mass and stiffness matrices of the system at hand.

$$\bar{C} = \propto \bar{M} + \beta \bar{K} \tag{2.1}$$

This way of constructing of the damping matrix, in a modal framework, provides precise damping at two design frequencies (here titled ω_1 and ω_2), and varying levels of damping for all others though the damping between the chosen frequencies is practically speaking constant (assuming both targeted frequencies had the same damping). For frequencies outside the bounding values, larger damping is seen.

The main concerns with Rayleigh Damping can be best described graphically in Figure 2.2. The two coefficients α and β are used to weigh how much mass and stiffness proportional damping is being applied to the system respectively.

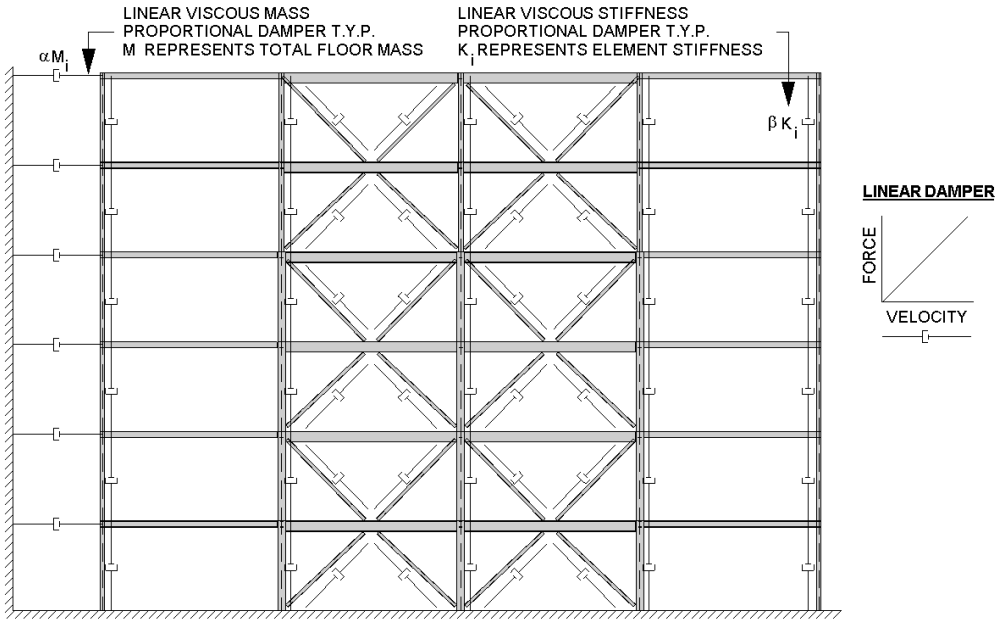

Figure 2.2 Physical interpretation of Rayleigh damping

In the case of mass proportional damping, a typically diagonal mass matrix is multiplied by a damping coefficient (α) which is directly related to the absolute velocity of the mass itself. This is equivalent to every mass having a damper connected to a wall at every degree of freedom. This physically can be interpreted as the building moving through a viscous fluid, creating a drag force over the height. This is neither truly physical nor representative of what actually happens in a typical building.

Stiffness proportional damping involves the variation of velocities between elements, which is a more physical approach to the problem, but is often not used exclusively for fear of over damping higher modes in a system. Mass and stiffness proportional damping are typically used in tandem to create the control necessary for a wider array of degrees of freedom, which is precisely what Rayleigh Damping is (See Figure 2.6).

Modal damping, another method of construction of the damping matrix, is mathematically expressed in Eq. 2.2. This damping model is based on the initial mode shapes of a system and is completely linear. The most notable disadvantages of this formulation is that it is does not assemble a banded damping matrix, but rather a full matrix, and that it only damps the modes which are directly prescribed. Therefore, higher modes may have no damping at all if an insufficient number of modes are used in its construction. It is often recommended with this type of damping that a small percentage of Rayleigh damping be added to the system to avoid undamped modes or degrees of freedom from being unconstrained (Powell, 2011). This damping model is completely linear and is based on the initial mode shapes of the system.

$$\bar{C} = \sum_{n=1}^{N} \frac{4\pi}{T_n} \xi \frac{(\bar{M}\phi_n)(\bar{M}\phi_n)^T}{{\phi_n}^T \bar{M}\phi_n} \tag{2.2}$$

where ϕ_n is the nth mode of the system, T_n is the nth mode period and ξ represents the target damping ratio.

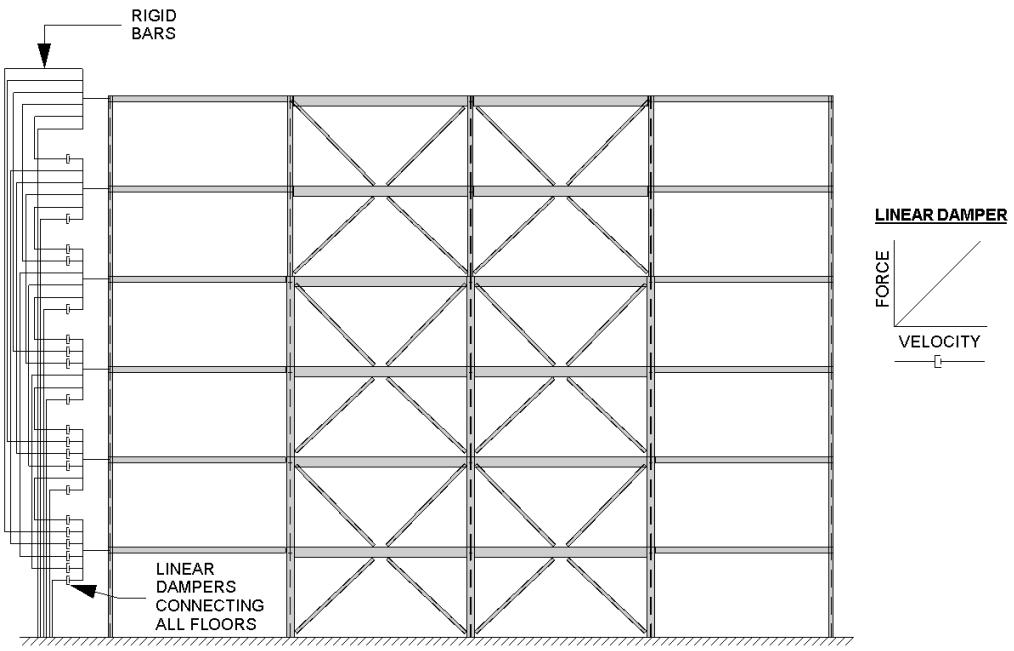

Figure 2.3 Simplistic physical interpretation of modal damping implementation assuming only horizontal degrees of freedom and highlighting the implied interconnectivity of all degrees of freedom to each other.

Modal damping creates a rather unphysical system as well, as the fullness of matrix implies dampers which connect every degree of freedom to one another. To demonstrate this, Figure 2.3 assumes that there are only horizontal degrees of freedom in the system. A full damping matrix connects all floors, not just adjacent floors. An example of the unphysical nature of modal damping can be seen when a damper spans directly from degrees of freedom at the roof to the base of the building.

Another nonphysical component of the modal damping matrix is that the formulation implies dampers can have negative coefficients. This means that instead of removing energy from the system, they are in fact increasing the applied forces in the system. Simplistically, if dampers in a shear structure were positive (created a resisting force under inter-story velocity demands) then the values of the off diagonal terms should be negative (See Figure 2.4). If all the modal vectors of a system are not used when constructing the modal damping matrix, positive off diagonal terms can appear.

For the building used in this study, assuming only horizontal degrees of freedom, the damping matrix is developed in Table 2.1. Note that if only 4 translational modes for our 6 floor building are used to construct the damping model, positive off diagonal terms are observed. If all the available modes up to the 50th mode (a limitation in Perform 3D) are used in this model, the resulting final damping matrix is

shown in Table 2.1b. Note that this matrix still has positive off diagonal values due to vertical and torsional modes not contributing to the horizontal degrees of freedom. We highlight the positive values in these matrices in order to indicate that negative dampers are another nonphysical element of this mathematical model that naturally occur. It is worth noting that if all mode shapes are included in this formulation, no off diagonal positive values would exist for translational degrees of freedom. This is often impractical in taller structures which require more than 50 modes to fully describe the structure, not to mention spurious modes that tend to occur in more elaborate structures.

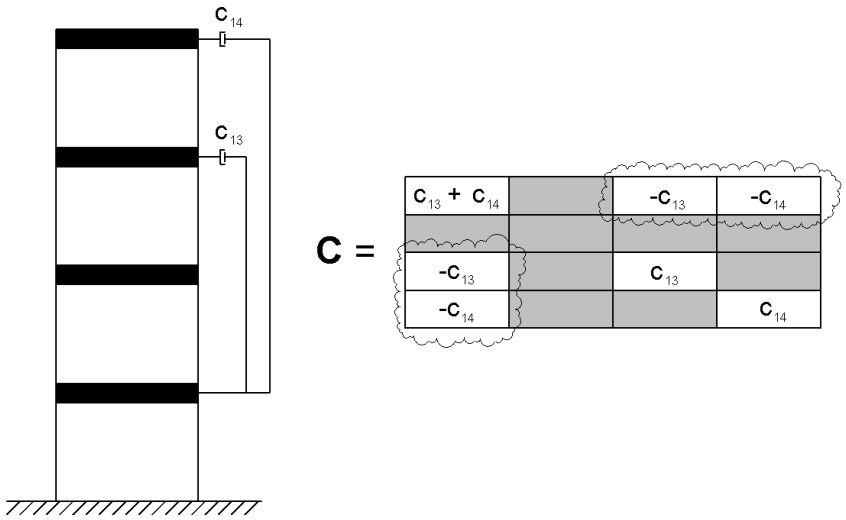

Figure 2.4 Inter-story shear damper proxy model showing off diagonal negative coefficients for positive values damping coefficients.

	Damping Matrix with 4 Translational Modes					
Level 1	4.102	2.714	-1.793	-1.781	1.602	-0.392
Level 2	2.714	2.848	0.502	-1.169	-0.679	0.354
Level 3	-1.793	0.502	3.825	1.562	-2.945	0.331
Level 4	-1.781	-1.169	1.562	2.600	0.705	-1.487
Level 5	1.602	-0.679	-2.945	0.705	4.876	-1.783
Level 6	-0.392	0.354	0.331	-1.487	-1.783	3.525

(a)

	Complete Model Damping Matrix					
Level 1	10.367	-3.258	-0.299	-0.166	0.039	-0.054
Level 2	-3.258	9.692	-3.099	-0.428	-0.235	-0.070
Level 3	-0.299	-3.099	8.930	-3.164	-0.430	-0.210
Level 4	-0.166	-0.428	-3.164	8.542	-2.915	-0.580
Level 5	0.039	-0.235	-0.430	-2.915	7.523	-2.941
Level 6	-0.054	-0.070	-0.210	-0.580	-2.941	4.591

(b)

Table 2.1 Simplified 6 story braced frame damping matrix in primary direction. The damping matrix constructed with only 4 translational modes (a) has a series of off diagonal terms which are indicative of negative damping. Even when all the modes of the system are taken into account, there may still be off diagonal terms which are positive (b).

A third type of damping implementation is presented that involves not only the direct modeling of damper elements, but also imposes a cap on the damping force corresponding to the assumed plastic capacity of the floor. Specifically, we focus on a braced frame structure with linear visco-elastic damping prescribed in tandem with column elements axial deformation, and nonlinear visco-plastic damping prescribed in tandem to the bracing elements. These elements allow for controlling the maximum shear force at any floor by anticipating where nonlinear events will occur. While the structure remains linear, this is simply a reduced form of stiffness proportional damping, as we are not applying dampers to every degree of freedom of the structural elements (such as rotational). In a braced frame structure, a majority of the strain energy is in the brace and column elements axial deformation. Therefore we intend to capture a very similar response to an overall stiffness proportional damping strategy while the structure remains linear.

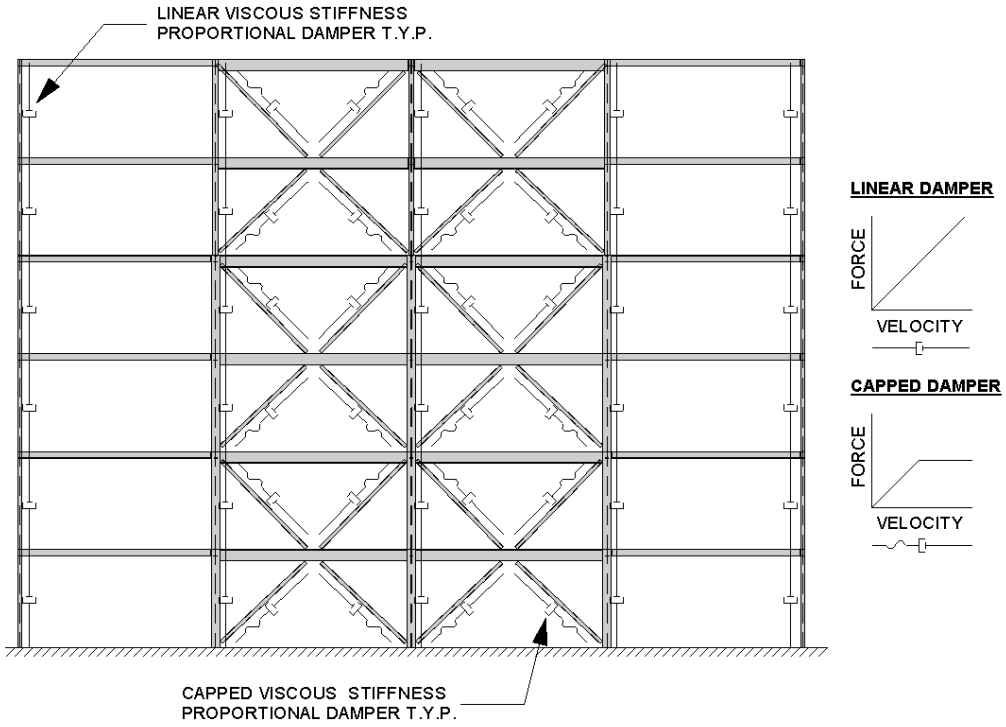

Figure 2.5 Physical interpretation of viscous capped damper implementation in this study

The benefit of this modeling strategy is that it prevents over reliance on viscous damping forces, which can become excessively resolving, as has been explored in special cases in Hall 2006. This is done by capping the applied damping forces of the bracing elements (the primary shear stiffness components) to a percentage of the floor level plastic capacity of the model. This capping force has a direct implication on the behavior of the structure in the nonlinear regime, and will be examined further here.

It is of note that other researchers have worked on implementing other nonlinear damping strategies, most notably the tangent stiffness damping matrix, and have done comparisons with linear Rayleigh damping schemes (Jehel, Leger, & Ibrahimbegovic, 2014). While these tangent stiffness methods resolve some issues associated with mass proportional damping, as well as over damping spurious deformation characteristics, it does so in an unphysical way. When a structure yields, it is most likely to begin to develop its most significant velocity differentials and/or damping forces. In the tangent stiffness based formulation, damping resistance is reduced at the point of plastic yielding, which is when damping forces are expected to be the largest as relative velocities increase. This nonphysical approach to resolving the problems associated with elastic damping matrices leads to underdamping in the overall system in a nonlinear excursion.

2.2 Implementation of damping strategies in this study

All computations are conducted with the commercially available software Perform 3D to benchmark our study and show the implementations in an industry standard platform; however, the various types of damping models can be implemented in most nonlinear finite element codes. To apply the proposed damping strategies in Perform 3D, we use suggested and implemented damping strategies in the software (Rayleigh, Stiffness Proportional and Modal), as well as develop a custom damping strategy by creating fluid damper elements with nonlinear properties. For all aforementioned methods, our goal is to match the fundamental mode period damping ratio and free vibration response, as well as show variations in forced vibration response.

In the Rayleigh damping implementation, we assign 2% damping in the first mode (T_1), and at 20% of the first mode ($0.2xT_1$), which results in the damping distribution shown in Figure 2.6. Note that for the periods between the targeted damping values, the damping ratio is slightly lower than 2%, and beyond this range damping is higher.

Next, we remove the mass component of Rayleigh damping strategy, and enforce 2% damping at the first mode by means of stiffness proportional damping. This results in a higher damping ratio for all other modes of the linear system (See Figure 2.7).

Modal damping is enforced by including the first 50 modes of the structure and targeting 2% damping for all modes considered. Note, 50 modes are included in an attempt to capture the 6 primary translational modes contribution to the damping matrix in both directions. An additional .02% Rayleigh damping term is applied to the system to constrain potential spurious deformations not included in our

modal damping matrix formulation (Powell, 2011). All the mentioned damping schemes described thus far are standard methods implemented in Perform 3D, and are summarized in Figure 2.7.

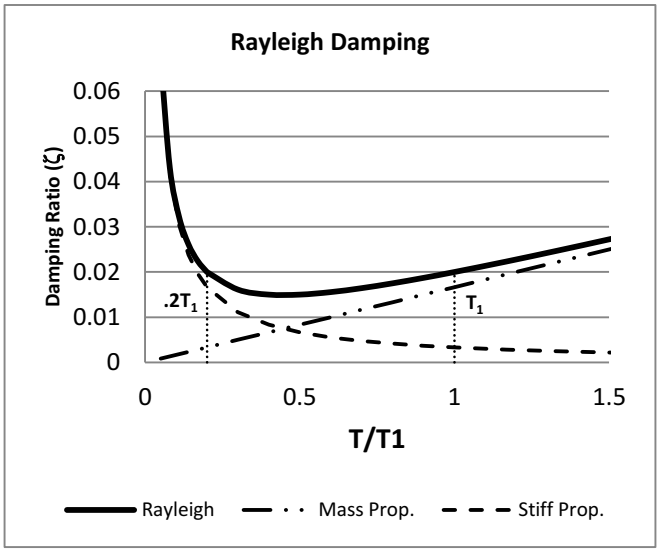

Figure 2.6 Rayleigh, mass, and stiffness proportional damping.

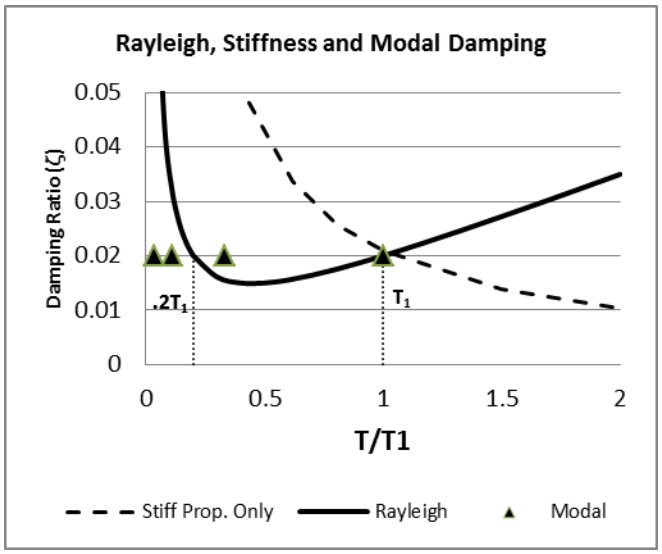

Figure 2.7 Rayleigh, stiffness proportional, and modal damping

The proposed viscous capped damping scheme is atypical, primarily in its nonlinearity, from the previously described implementations. An initially linear velocity dependent stiffness needs to be developed, which is then reduced to zero after a capping force is reached. This is an analog to an elastic

perfectly plastic element formulation with respect to nonlinear stiffness applications. To establish this velocity dependent stiffness, we target a specific damping ratio at a specific period of the structure. In our computational experiment, we use the first fundamental translational mode for tuning our dampers to 2% equivalent damping. This is done by using a purely stiffness proportional approach to the axial components of the braced frame system. We refer to this linear form of damping as "Beta-K damping" by setting α to null (See Eq. 2.1) and solving for β (See Eq. 2.3).

$$\beta = \frac{2\xi}{\omega_1} \tag{2.3}$$

where ω_1 is the first fundamental frequency of the building.

Once β is determined, we develop the initial damper stiffness of each element by multiplying the element stiffness matrices by the resolved coefficient. Note, in this particular implementation of a braced frame, we did not use all of the terms in the element stiffness matrix and focused only on the axial terms. This is appropriate for a braced frame system where a majority of the strain energy is stored in axial deformation. This simplification makes the implementation of the physical dampers quite trivial (simple bar damper elements) with a value of linear damping stiffness shown in Eq. 2.4.

$$C_o = \beta \frac{AE}{L} \tag{2.4}$$

For this particular implementation, we also limited our damper types to linear for column elements and nonlinear for brace elements. This is done to simplify the quantification of damping capping forces for this study, and allow for physical intuition into the behavior. Capping forces could similarly be applied to other components (such as the columns and beams) and also to other deformation contributions (such as bending and shear), but are not implemented for clarity.

To develop the capping forces of each individual brace, we seek to determine the anticipated failure mechanism of brace elements working in tandem. This is appropriate for a chevron or inverted chevron system as will be explained. To implement the intended relative capping forces, it is necessary to determine at what force the floor yields in shear, and then limit our floor dampers to a force which is a percentage of this yield force.

If we assume a simplistic form of the failure scenario in which the braces themselves give way and a story mechanism forms, a specific yield force can be quantified for a given floor. In the case of co planar brace elements, there are only so many ways the floor can fail. We assume in this study that if a brace buckles, it loses all of its capacity, and its symmetric counterpart is in tension at the same force. After buckling, the load is assumed to be redistributed to the tension brace, and if the brace has a tension yield

strength greater than two times the buckling strength of the buckled section, the floor does not form a mechanism until the total shear demand exceeds a single brace tension yield force. Otherwise, the floor yields immediately after initial buckling of the compression section as the tension brace does not have sufficient capacity to resolve the compression force. This all assumes the beam, connections, and other supporting components, are sufficient to take the shifted demand. This logic was applied in this study and is explained using a single bay braced frame in Chart 2.1. More elaborate schemes, such as using residual buckled strength of the braces, are possible, but the general concept is to determine a logical yield force of the floor and use it as a point of reference. A floor by floor pushover analysis of the structure could also be used to determine a logical yield value as well.

Once the yield force of the floor is known, a rational yield percentage is used to determine the maximum relative velocity of the damper before reaching the plastic plateau. In all comparisons between the various damping methods shown, 10% of the plastic yield force of the floor was chosen as the cap of the individual damper element forces. We later perform a comparison of performance with varied levels of yield capacity in the dampers themselves. Once the floor level yield force percentage is determined, the damper element yield force (F_{DY}) is calculated individually.

$$F_{DY} = \frac{Portion\ of\ Floor\ Yield\ Force}{Number\ Of\ Dampers\ Per\ Floor} \tag{2.5}$$

To develop the nonlinear damping element in Perform 3D, we need to prescribe a damper stiffness (C_o) and yield deformation rate (velocity). To determine the yield velocity of the element, we take each individual damper's contribution to the floor yield force percentage (rotated by inclination angle) and divide by linear damping stiffness parameter C_o.

$$v_{yield} = F_{DY\_rot} * \frac{1}{C_o} \tag{2.7}$$

This yield velocity, along with the initial damping stiffness, fully defines the nonlinear damping element that is perfectly plastic after reaching the yield velocity differential (and subsequent yield force). Calculations for these element stiffness parameters are summarized in Table 2.2.

The viscous capped damper element stress-strain relationship is significantly different than traditional tangent stiffness strategies. At a specific yield velocity, the capped damper yields and provides constant restoring force. This is in contrast to a tangent stiffness that (in the case of an elastic plastic

stiffness element) reduces to zero force at an arbitrary velocity. This nonlinear coupling of viscous forces with nonlinear damping does not make for a physically consistent model. As an example, if a building were being pushed over slowly with a tangent stiffness damping model, inter-story velocity differentials would be near zero, translating to zero damping forces. Upon yield of the structure, when relative velocities begin to increase for the first time, there would be no restoring force available as the dampers force versus velocity ratio would be nil as the stiffness terms are now zero. This inconsistency between the damping forces and a critical velocity creates a variability in the damping yield force and velocity that is dependent on ground motion, and less dependent on the structure itself (See Figure 2.8).

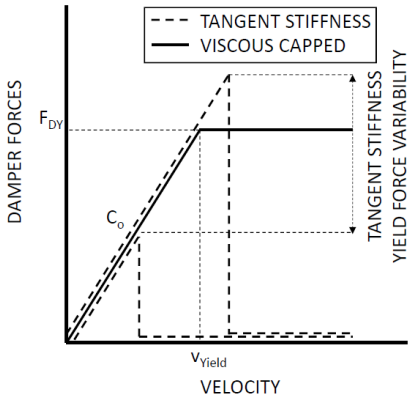

Figure 2.8 Variation between tangent stiffness and viscous capped damping.

`

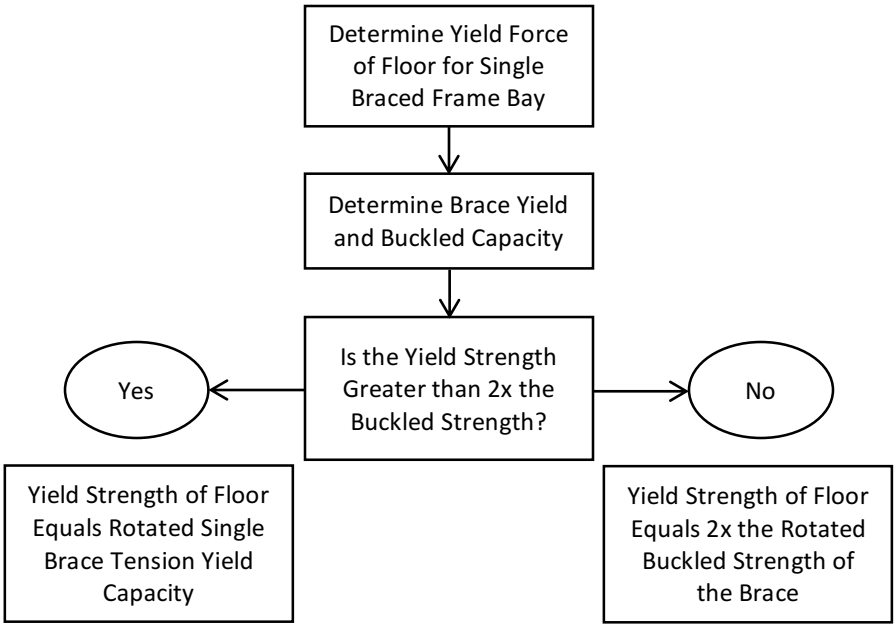

Chart 2.1 Determining total floor yield strength of a single bay braced frame

Floor Level	Brace Size	Braced Bays	Angle of Braces from ground	Buckled Stress	Tension Yield Stress	Area	Buckled Brace Strengh	Yield Brace Strength	Failure Mechanism
			(deg.)	(Mpa)	(Mpa)	mm^2	(kN)	(kN)	
6	HSS6x6x1/2	4	45	172	445	6284	1083	2794	Tension Brace Failure
5	HSS6x6x1/2	4	45	172	445	6284	1083	2794	Tension Brace Failure
4	HSS7x7x1/2	4	45	226	445	7484	1690	3328	Failure at First Buckling
3	HSS7x7x1/2	4	45	226	445	7484	1690	3328	Failure at First Buckling
2	HSS7x7x5/8	4	45	220	445	9032	1985	4017	Tension Brace Failure
1	HSS7x7x5/8	4	45	220	445	9032	1985	4017	Tension Brace Failure

	Single Tension Yield	2x Buckled Strength	Floor Design Shear Capactiy	Shear Damper Yield Force	Axial Yield Force in Damper	Single Brace Stiffness	Co Single Brace	Yield Velocity
	(kN)	(kN)	(kN)	(kN)	(kN)	(kN/mm)	(kN-s/mm)	(mm/s)
6	7904	6127	7904	790	**1118**	275	1.30	107.30
5	7904	6127	7904	790	**1118**	275	1.30	107.30
4	9413	9562	9562	956	**1352**	327	1.55	109.00
3	9413	9562	9562	956	**1352**	327	1.55	109.00
2	11361	11230	11361	1136	**1607**	395	1.87	107.30
1	11361	11230	11361	1136	**1607**	395	1.87	107.30

Table 2.2 Capped damper element calculations

2.3 Free vibration results

A simple test is performed to compare free vibration properties of various damping strategies where our 6 story structure is accelerated to a deformed configuration over a time duration of 15s and then released. While this is not a perfect first mode shape of the structure, it is similar, and creates an initial condition of displacement for us to examine the free vibration response of the structure from a similar configuration. Here we compare the various damping strategies and the free vibration decay of the model by examining the roof displacement response history.

Examining Figure 2.9, a near equivalence in the damping strategies for free vibration from the initial deformed shapes is observed. This is intentional as all proposed methods are meant to have similar damping in the first mode shape. Any inconsistencies are attributed to the fact that the deformed shape is not exactly a first mode deformation and the various methods have different effective damping for each of the subsequent potential modes as explained previously.

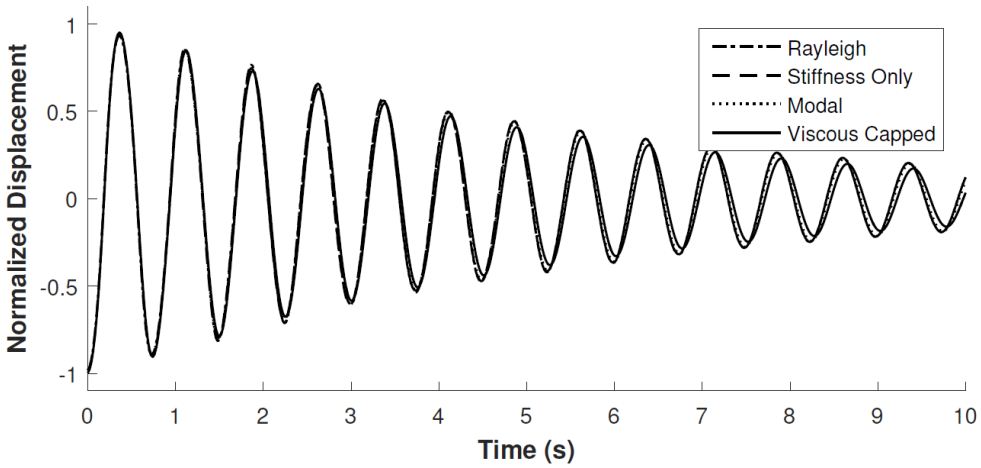

Figure 2.9 Damped free vibration comparison of pseudo first mode damping showing near equivalence in response

2.4 Forced vibration results

We next examine each of the four implemented strategies for the Rinaldi Station ground motion from the 1994 Northridge earthquake to observe variations in the response based on the damping assumptions.

Figures 2.10 through 2.13 represent various response history plots on every floor of the 6 story building modeled for comparison. The left side of each plot shows simplistic story responses over the height of the building (displacement, drift, and shear force), while the right side shows a breakdown of damping forces in the system. Note that the upper right corner represents the "total damping forces" on a story by story case, and the components below represent the Rayleigh elements of damping (stiffness and mass proportional) which are portions of the total.

We start by looking into traditional Rayleigh methods and the responses shown in Figure 2.10. At the main nonlinear excursion in the system, total damping forces are more than 31% of the yield force of the base of the building (See Table 2.2). This large restoring force during the event helped maintain stability and reduced the overall response. This highlights the concept under dispute: are damping forces of up to 31% of the structural capacity of the building reasonable? In this example we see an unphysical component of the damping strategy overall where the mass proportional term is a majority of the peak shear force resistance.

The next analysis implements stiffness proportional damping, known to provide excessive damping in the higher modes of a linear structure. As expected, Figure 2.11 shows damping forces that

are much larger than Rayleigh, reaching 59% of the anticipated base strength of the structure at its peak. This shows how having mass proportional damping in the system helps alleviate systemic over damping in the model. Note in this result that the mass proportional term has zero contribution.

The recommended method for implementing damping in Perform 3D is Modal Damping, the subject of the third analysis. Figure 2.12 shows a significantly reduced set of damping forces that correspond to approximately 11% of the design plastic shear. For complete transparency, we implement an additional .02% Rayleigh damping for computational concerns (discussed earlier). This explains the small portion of stiffness and mass proportional forces observed over time.

Finally, our implementation of linear viscous capped damping yields the responses observed in Figure 2.13. As constructed, no damping shear force exceeds 10% of the plastic shear capacity of any floor. As one might expect, this results in higher drifts, flat-lined total damping shear force observed over time, and lack of mass or stiffness proportional resistance.

Figure 2.14 shows the effective roof displacement of every floor over time, the peak values of which are summarized in Figure 2.15, along with other critical response characteristics. As expected, deformation based responses are higher when viscous capped damping is used. This expresses the critical nature of understanding and implementing an appropriate damping strategy.

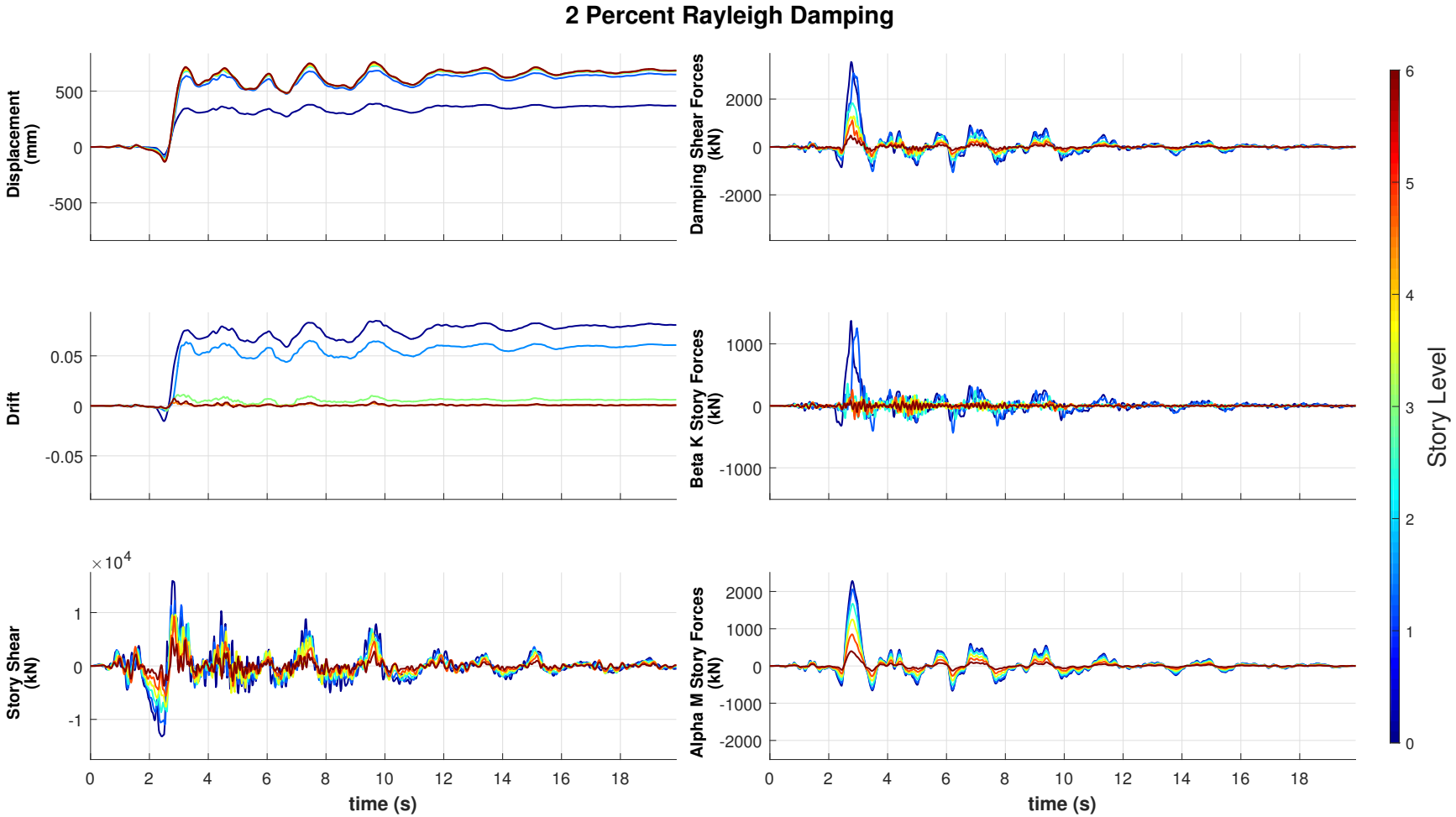

Figure 2.10 2% Rayleigh damping for 1994 Northridge earthquake using Rinaldi Station input

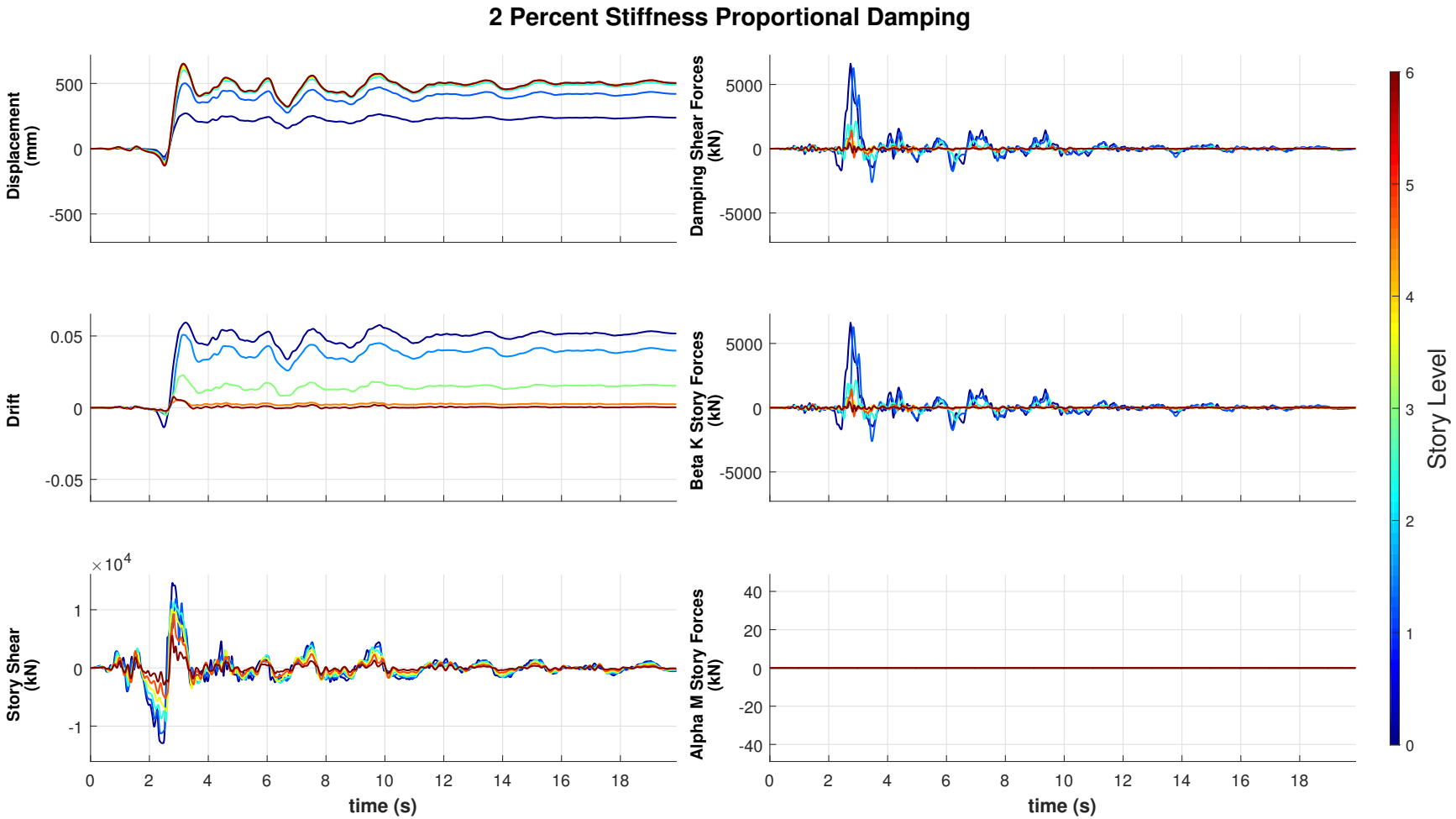

Figure 2.11 2% Stiffness proportional damping for for 1994 Northridge earthquake using Rinaldi Station input

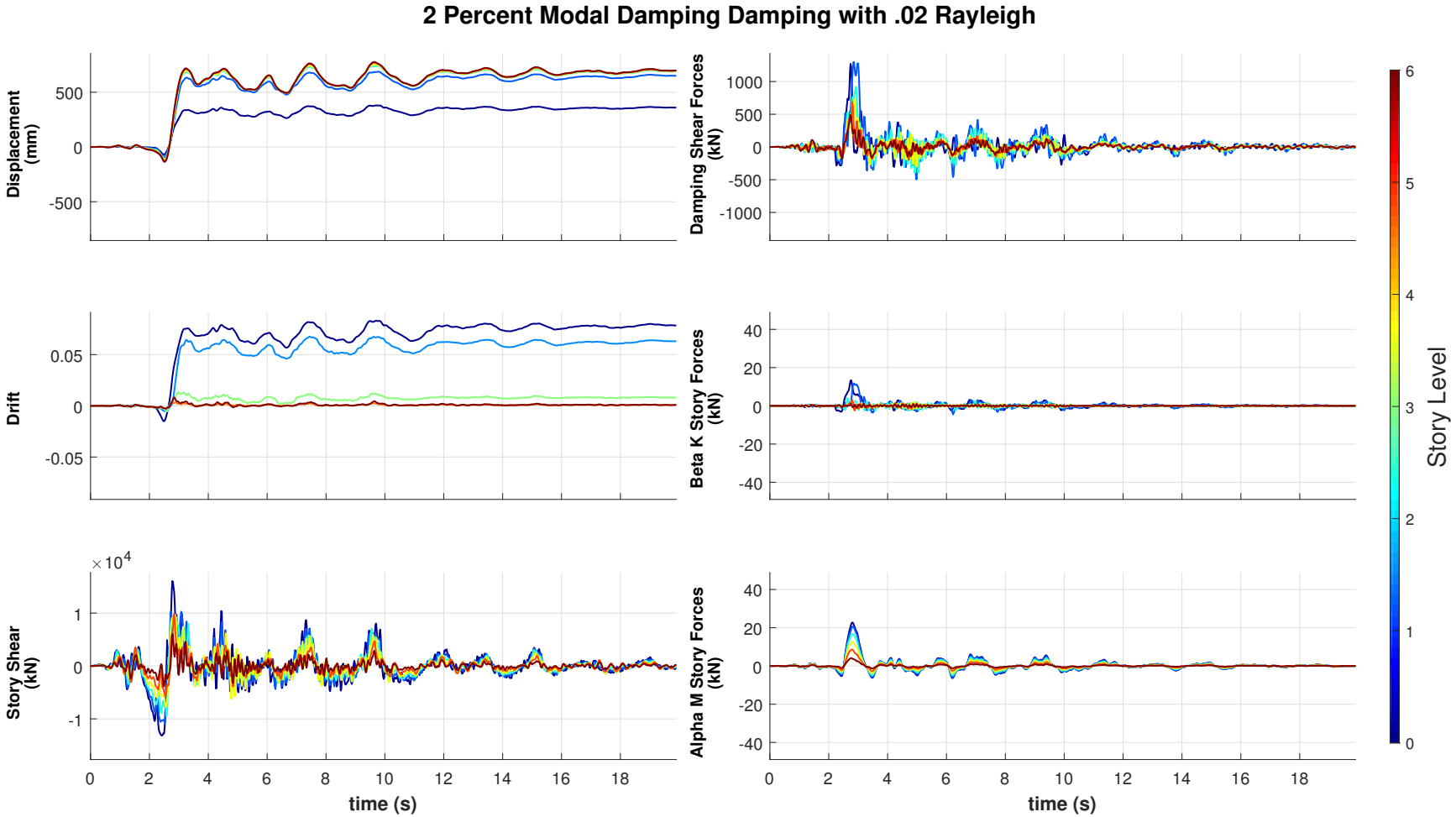

Figure 2.12 2% Modal damping for 1994 Northridge earthquake using Rinaldi Station input

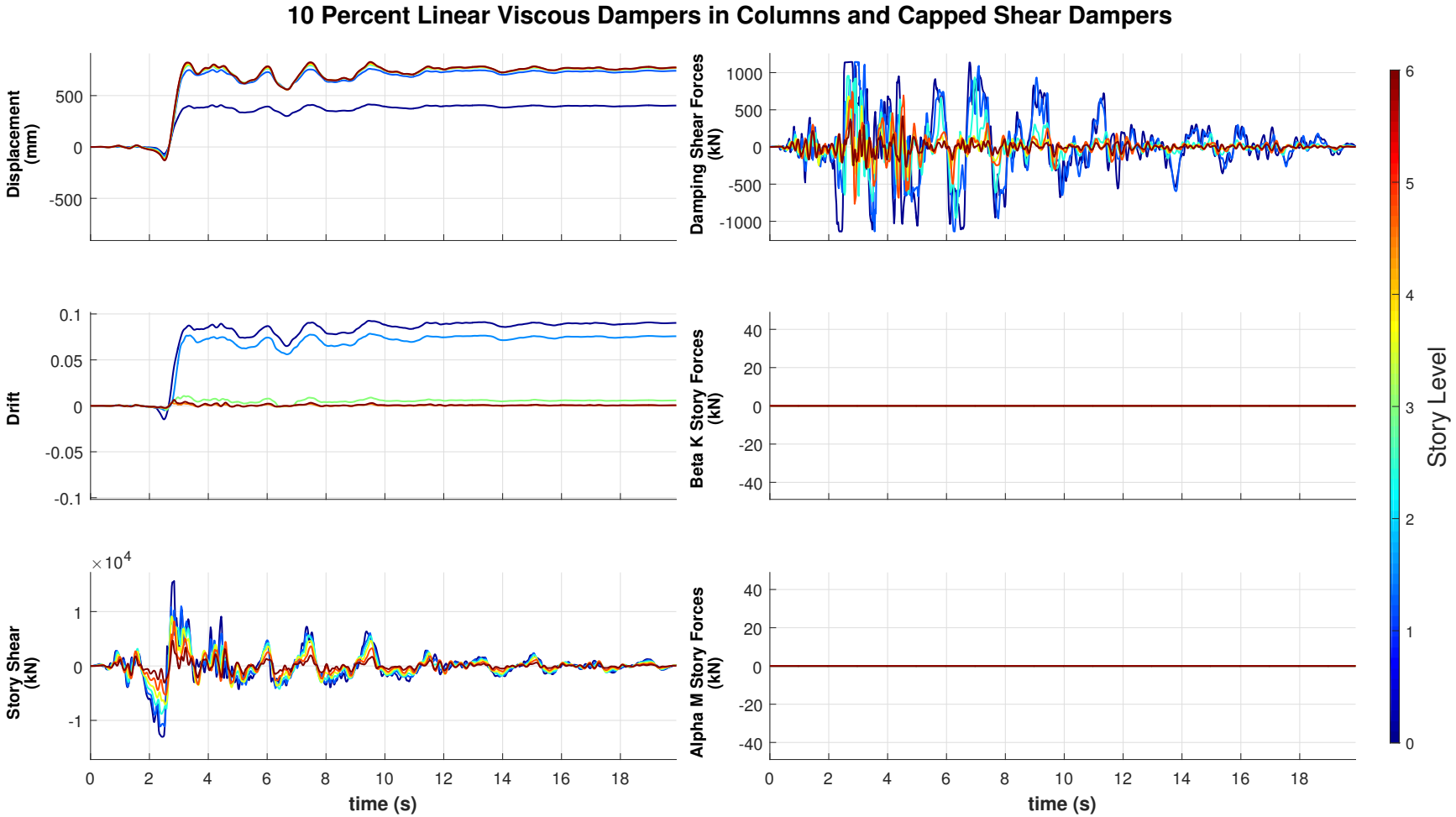

Figure 2.13 10% Linear viscous capped 2% damping for 1994 Northridge earthquake using Rinaldi Station input

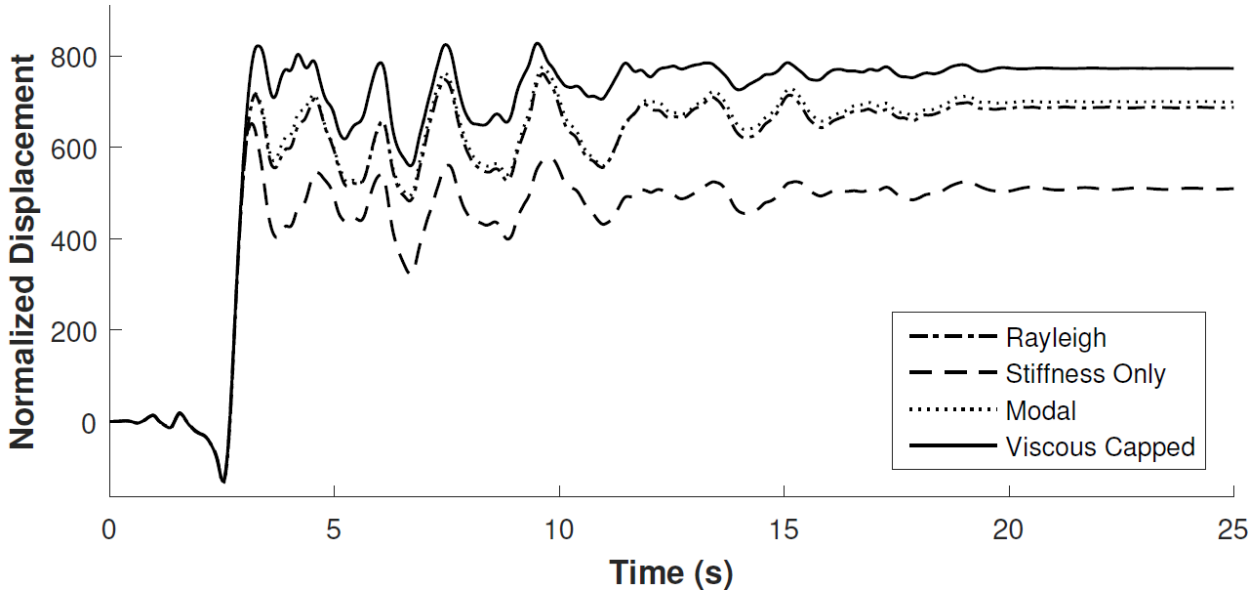

Figure 2.14 Roof displacement of varied damping strategies for Rinaldi Station, Northridge

	Peak Responses						
	Displacement	Drift	Shear	Beta Shear	Alpha Shear	Damping Shear	Damping Shear/Plastic Capacity
	(mm)		(kN)	(kN)	(kN)	(kN)	
Viscous Capped	828	0.093	15,633	-	-	1,144	10%
Modal	777	0.083	16,082	-	-	1,300	11%
Rayleigh	761	0.085	15,922	1,372	468	3,553	31%
Stiffness Proportional	652	0.059	14,623	6,622	-	6,622	59%

Figure 2.15 Peak responses from various damping strategies highlighting the variation in the total damping shear force relative to the plastic capacity of the building itself.

2.5 Varied capping levels

From an engineering perspective, it is critical to explore various capping force levels and to understand the impact on response, as the capping level chosen for prior comparisons is seen by the authors as reasonable, yet arbitrary. The proposed capped damping system has its basis in stiffness proportional damping. As such, until the capping force is set to 59% of the shear capacity of the floor, there will always be some level of capped forces in this particular system based on our previous results (See Figure 2.15). Put forth are variations between what are believed to be practical constraints on the damping force and the structural responses to the Rinaldi Station, Northridge ground motion. Specifically adding to our previous studies of a 10% plastic limit, the capping force is varied additionally between 4%, 15%, and 20%. The results are presented and summarized in Figures 2.16 through 2.19 Figure 2..

The results shown demonstrate the importance of the capping value itself. Focusing on the variation in damping shear force over time for each, one observes a variance in the volatility in the damping shear forces over time. When the capping force is set very low (see Figure 2.16), the lower floor dampers repeatedly cap throughout the duration of the ground motion. Alternatively, when the capping force is set higher (See Figure 2.17 and Figure 2.18), the dampers hit their capping value during the first impulse of the system and then resume a traditional linear damping. The peak response characteristic variations are considerable (See Figure 2.19) and illustrate the importance of the prescribed limits of capped damping forces.

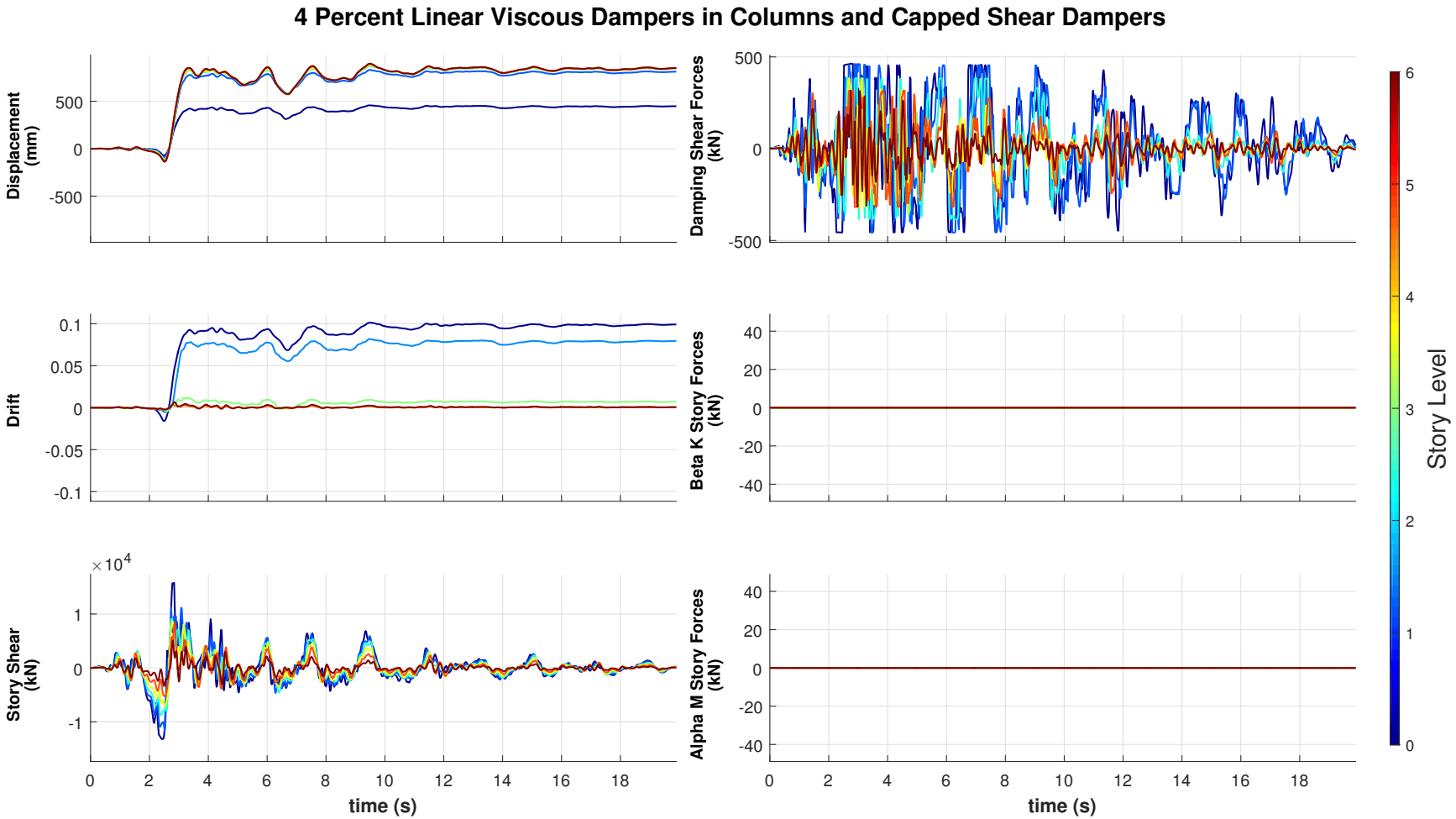

Figure 2.16 4% Linear viscous capped 2% damping for 1994 Northridge earthquake using Rinaldi Station input

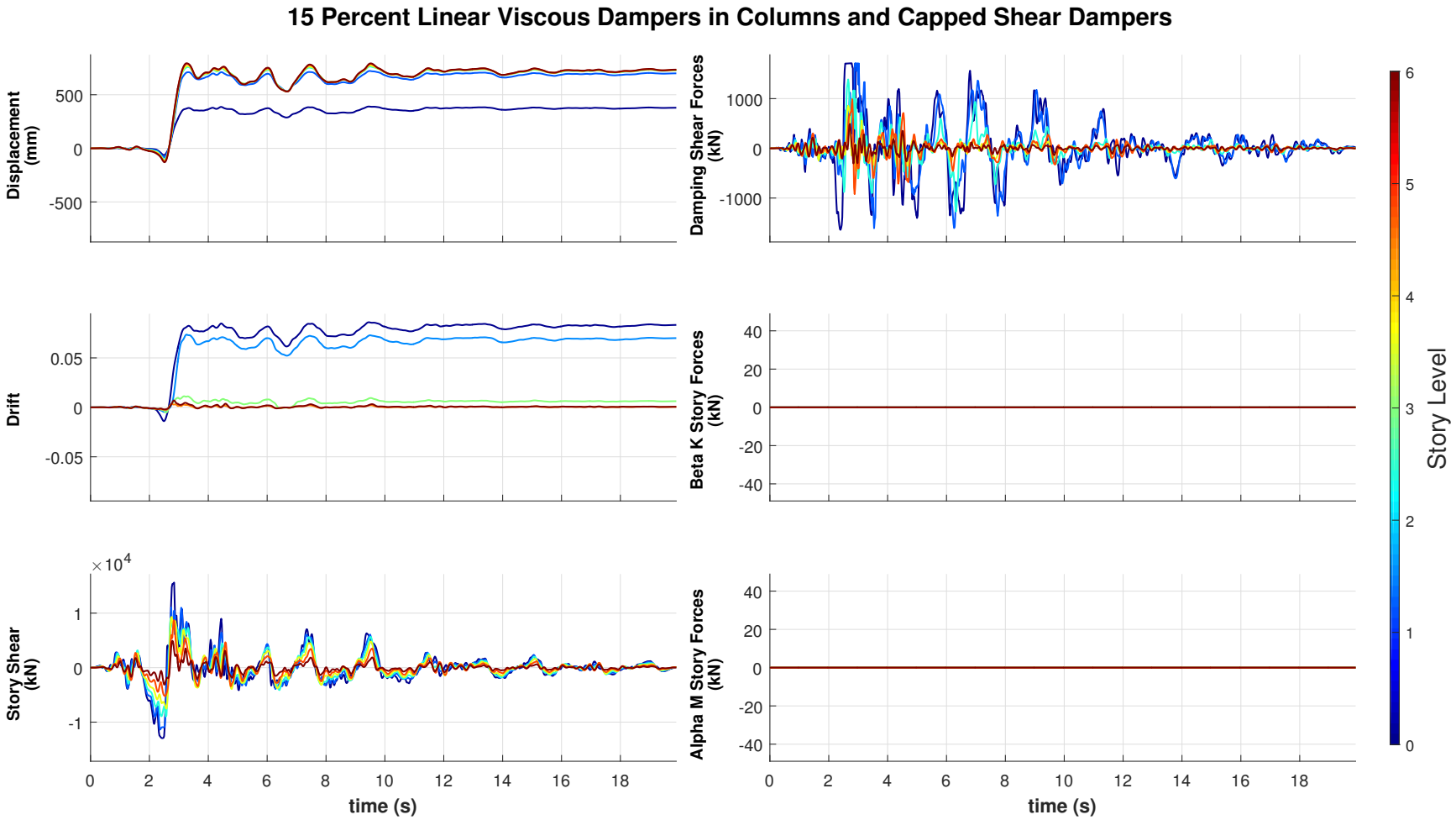

Figure 2.17 15% Linear viscous capped 2% damping for 1994 Northridge earthquake using Rinaldi Station input

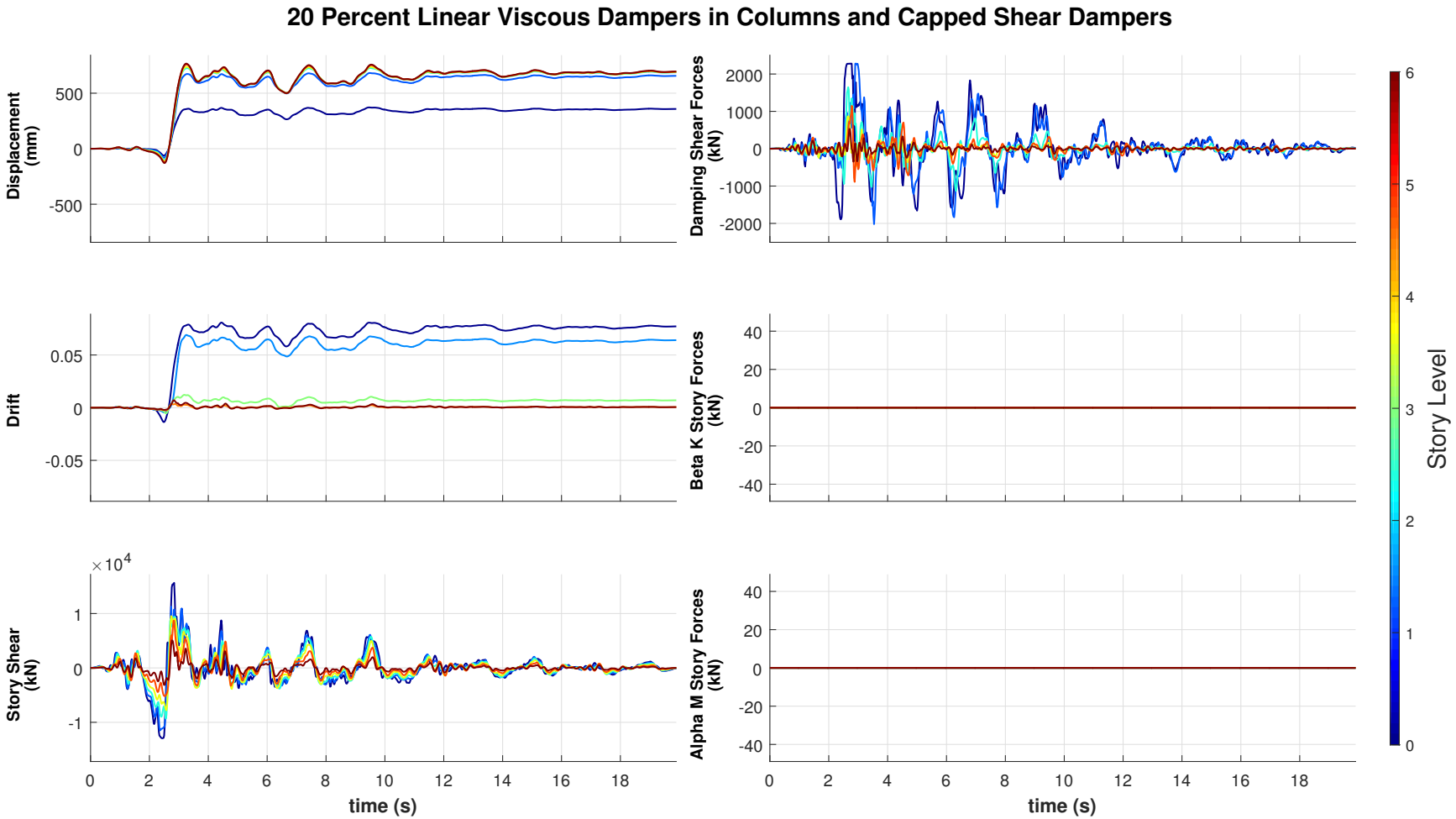

Figure 2.18 20% Linear viscous capped 2% damping for 1994 Northridge earthquake using Rinaldi Station input

Peak Responses							
	Displacement	Drift	Shear	Beta Shear	Alpha Shear	Damping Shear	Damping Shear/Plastic Capacity
	(mm)		(kN)	(kN)	(kN)	(kN)	
4% Max Damp. Shear	897	0.101	15,782	-	-	463	4%
10% Max Damp. Shear	828	0.093	15,633	-	-	1,144	10%
15% Max Damp. Shear	794	0.086	15,616	-	-	1,712	15%
20% Max Damp. Shear	766	0.081	15,641	-	-	2,278	20%

Figure 2.19 Peak responses from varied capping forces demonstrating a nonlinear relationship between the characteristic responses of the structure and the level of prescribed capping forces.

2.6 Conclusion

The work presented in this chapter shows how various damping strategies compare to one another, and advocates the use of a nonlinear damping solution that maintains constant force after achieving a capping value. The purpose of this was to demonstrate how the use of viscous capped damping can be incorporated into readily available industry tools, and further the understanding of the effects it has on overall response. We began by showing an equivalence of the damping strategy in the linear range for any specific mode shape prescribed, and then proceeded to show the variation of each strategy in the nonlinear regime.

An exploration into the variation in capping forces relative to the plastic capacity of the structure was also explored. Note the nonlinear shift in peak responses based on varied capping force levels. This is done to represent the significance the percentage variations can have on overall behavior to a particular response.

While the presented nonlinear damping implementation overcomes many of the concerns associated with other linear and nonlinear damping methods, the question remains as to what level of force should damping forces be limited relative to the capacity of the structure. Resolving energy losses in a system during a nonlinear excursion is not a simple task. However, applying a rationale of how much force the engineering community believes is practical may not be as difficult. Various values of capping forces were explored, but implementing this strategy on a variety of structures to better understand the consequences of the capping forces would aid in this future conversation. Further, other relationships besides the linear viscous capped nonlinear relationship proposed should be investigated to determine the effect of varied initial and secondary stiffness on response.

It is clear that capping the damping forces in the system is a practical and implementable design strategy. This is a critical piece missing from the further reliance of nonlinear analysis results in building

structures. Developing similar implementable strategies in other lateral load resisting systems (moment frames, concrete walls, etc.) is the next step in creating a more robust damping strategy for performance based analysis.

2.7 References

ASCE 7, "Minimum Design Loads for Buildings and Other Structures" Reston: *American Society of Civil Engineers*, 2010

Charney, F. A., "Unintended Consequences of Modeling Damping in Structures" *Journal of Structural Engineering*, 581-592, 2008

Crisfield, M. A., "Non-linear Finite Element Analysis of Solids and Structures - Volume 1&2" West Sussex*: John Wiley & Sons Ltd*, 2003

Hall, J., "Seismic Response of Steel Frame Buildings to Near-Source Ground Motions" Pasadena: *Earthquake Engineering Research Laboratory*, 1997

Hall, J. F., "Problems encountered from the use (or misuse) of Rayleigh damping" *Earthquake Engineering and Structural Dynamics, 35*(5), 525-545, 2006

Hamburger, R., Krawinkler, H., Malley, J., & Adan, S., Seismic Design of Steel Special Moment Frame Systems. Gaiitherburg: *National Institute of Standards and Technology*, 2009

Hardyneic, A., An Investigation into the effects of damping and nonlinear geometry models in earthquake engineering analysis. *Earthquake Engineering and Structural Dynamics, 44*(15), 2695-2715, 2015

Jehel, P., Leger, P., & Ibrahimbegovic, A., Initial versus tangent stiffness-based Rayleigh damping in inelastic time history seismic analyses. *Earthquake Engineering and Structural Dynamics*, 467-484, 2014

Michel Bruneau, C.-M. U., "Ductile Design of Steel Structures" New York: *McGraw-Hill,* 1998

Powell, G. H., "Perform 3D User Guide" Berkeley, *Computers and Stuctures Inc.*, 2011

Roeder, C. W., "Seismic Behavior of Concetrically Braced Frame" (Vol. 115). *Journal of Structural Engineering*, 1989

Chapter 3

EFFECT OF SLIDING MASS ON THE RESPONSE OF FRAME STRUCTURES

3.0 Introduction

Nonstructural components and their effects on structural response have been addressed and reviewed by multiple researchers (eg. Lee, 2007; Hutchinson, 2014). These studies often examine the effects of coupling components (such as full height partitions) or the response of nonstructural components themselves (such as medical equipment and its viability after shaking). A secondary concern is components themselves sliding in the event of ground shaking (Chaudhuri, 2004; Konstantinidis, 2014). These types of studies concern themselves with the integrity of the components that are shifting (server racks, medical imaging equipment, etc.); however, little has been done to understand the potential effects this sliding behavior has on response of a structure as a whole.

Sliding nonstructural components have been observed in building type structures in many earthquake events via CCTV footage, personal video cameras, testimonials of earthquake victims, and validated in test centers (ex. Earthquake Test Lab, 2015). A myriad of potential sliding components such as wheeled desks and chairs, as well as items on shelves and desks, are some examples of potential live loads in the system that tend to overcome a minimum force of restraint (static friction maximum) and then proceed to shift decoupled from the structure's lateral response (or slide) for moments in time. More modern industrial facilities (such as data centers and power plants) are turning to more advanced solutions to minimize risk associated with the seismic hazard and relative damage of equipment (Malushte, 2005). These solutions often involve forms of in-situ isolation of mission critical elements of the facility (servers, reactors, etc.), as opposed to base isolation of an entire structure.

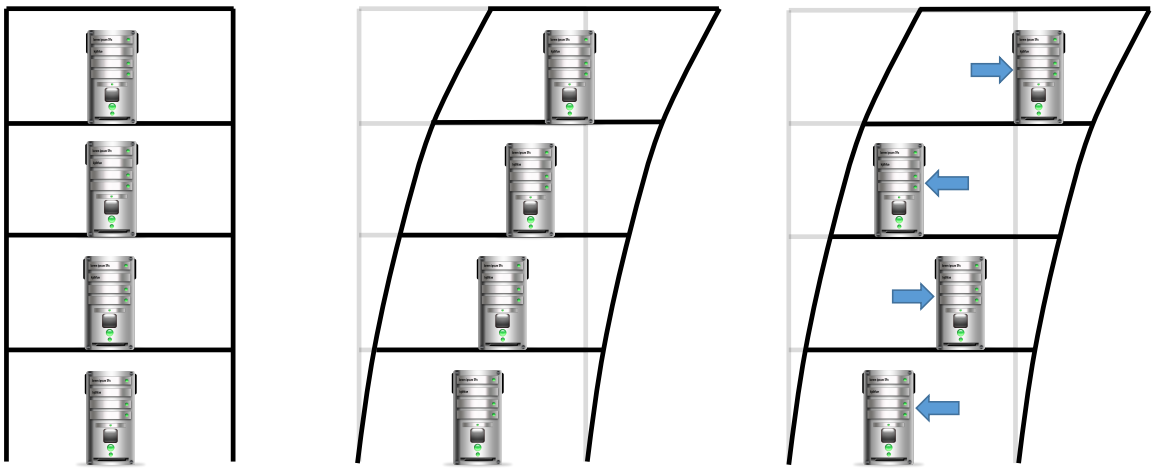

Figure 3.1 Schematic multistory datacenter in the (a) undeformed configuration. When mass is affixed to the floor, the contents of the building will move compatibly with the structure (b). However, if the contents are allowed to slide, the components will be uncoupled (c) and have unique degrees of freedom and configurations when compared to the structure. (*Server clipart courtesy of www.iconbug.com*)

This study seeks to quantify the effects associated with sliding masses and how variability in when and how much mass moves in a system can change the anticipated linear response of the structure (See Figure 3.1). The complications of adding in nonlinear effects of structural components are intentionally not presented here in order to decouple the issues and examine sliding mass explicitly. While many complicated physical models exist for evaluating this type of sliding behavior, we use Coulomb damping to simulate sliding in this study.

3.1 Quantifying potential sliding mass

Depending on the occupancy type of a building, the percentage of mass available for potential sliding is varied. For instance, in the case of a library and/or storage facility, there is a great deal of mass with the potential to slide and shift during an event. In contrast, a modern electronic office may have much less matter susceptible to shifting, but still has basic components (such as chairs, books, and other desk items) that could slide during a ground motion.

Quantifying this sliding mass ratio relative to the building mass is not a trivial task, nor is it expected to be particularly accurate. A brief summary of potential usages and building types is put forward to approximate the magnitude of available sliding mass in a particular occupancy. Here, two

usages are explored: traditional office space and data centers/storage facilities. While one could imagine a myriad of other potential situations, these two represent practical extremes of potential usages where sliding mass could have an impact on response.

ASCE 7 Minimum Design Loads for Buildings and other Structures prescribes a design load of 2.4 kN/m^2 for typical office space. More realistically, on a floor-by-floor basis, approximately 40% of the design live load is considered to be likely present in an average sense (considering ASCE 7 recommended live load reduction). This creates a logical upper bound on the potential mass available for sliding in an office environment, given that some mass would not be able to slide (such as desks/counters affixed to the structure).

An example of a more heavily loaded occupancy is storage facilities, which have unreducible loads in light storage conditions of 6 kN/m^2 (heavy storage is 11.97 kN/m^2) prescribed in ASCE 7. While this may sound extreme, consider data center facilities with typical cabinet weight limits and layouts described in Table 1.1. Weights of server racks and subsequent layout leave little room to debate over potential live load reduction, as server and/or battery rooms are densely populated with limited variation in the typical floor plan.

	Cabinet size:	600mm by 900mm"	600mm by 1050mm"	750mm by 1050"
	Aisle width:	900 mm	1200 mm	1200 mm
Cabinet Weight	500 kg	4.5	3.6	2.9
	750 kg	6.8	5.5	4.4
	1000 kg	9.1	7.3	5.8
	1250 kg	11.4	9.1	7.3
	1500 kg	13.6	10.9	8.7

Table 3.1 Average floor loading (kN/m^2) of typical server racks

For transparency, server farms are often built at grade level to avoid carrying and distributing these large loads; however, a transition to multi-story data centers in urban environments is becoming more common (Atlanta Business Chronicle, 2015). Additionally, commonplace in high seismic regions, these server racks are intentionally decoupled from floors to allow for sliding and/or rolling during an event to avoid damaging equipment. Simple products involving castor wheels, to more advanced products using isolation bearings (ex. IsoBase), create an intentionally low friction surface to minimize the transfer of forces between the server rack mass and the building structure.

With this in mind, we examine a few typical office and light storage scenarios with varied height to determine the relative effects of these potential sliding masses to total mass of the structure. In the case of typical storage (which is a proxy for data centers) the maximum potential sliding mass available, assuming all live load mass can slide, is greater than 50% of the total mass of the structure (see Table 3.2). Similarly, in the case of office space, this number can be near 20% of the total mass of the structure. This is meant to showcase the potential scale of decoupled mass available in typical structures; however, we explore relative sliding mass potential values between 5% and 25% as this range is considered more practical and will not exacerbate the potential effects. This spans a great deal of the space occupied in the lower portion of Table 3.3. We will show how this quantity of sliding mass can lead to change in linear structural response.

	Typical Storage Loading (kN/m2)					Typical Office Loading (kN/m2)				
Total Stories	3	5	10	15	20	3	5	10	15	20
Dead Load										
Steel										
Floor	0.48	0.48	0.48	0.48	0.48	0.29	0.29	0.29	0.29	0.29
Column/Bracing	0.30	0.32	0.40	0.53	0.71	0.25	0.27	0.34	0.44	0.59
Slab	2.80	2.80	2.80	2.80	2.80	2.39	2.39	2.39	2.39	2.39
Curtain Wall	0.25	0.25	0.25	0.25	0.25	0.24	0.24	0.24	0.24	0.24
SDL										
Carpet/finish	0.10	0.10	0.10	0.10	0.10	0.10	0.10	0.10	0.10	0.10
Mechanical/Susp, Ceiling	0.70	0.70	0.70	0.70	0.70	0.38	0.38	0.38	0.38	0.38
Partitions	0.50	0.50	0.50	0.50	0.50	0.48	0.48	0.48	0.48	0.48
Live	6.00	6.00	6.00	6.00	6.00	2.40	2.40	2.40	2.40	2.40
Reduced LL		100% Live Load Participation					40% Live Load Participation			
	6.00	6.00	6.00	6.00	6.00	0.96	0.96	0.96	0.96	0.96
Total Load	11.13	11.15	11.23	11.36	11.53	5.09	5.10	5.17	5.28	5.43

Table 3.2 Typical loading in storage and office facilities

	Typical Storage Loading (kN/m2)					Typical Office Loading (kN/m2)				
Total Stories	3	5	10	15	20	3	5	10	15	20
Slidable LL Percentage										
100%	53.9%	53.8%	53.4%	52.8%	52.0%	18.8%	18.8%	18.5%	18.1%	17.6%
75%	40.4%	40.4%	40.1%	39.6%	39.0%	14.1%	14.1%	13.9%	13.6%	13.2%
50%	27.0%	26.9%	26.7%	26.4%	26.0%	9.4%	9.4%	9.3%	9.1%	8.8%
25%	13.5%	13.5%	13.4%	13.2%	13.0%	4.7%	4.7%	4.6%	4.5%	4.4%
20%	10.8%	10.8%	10.7%	10.6%	10.4%	3.8%	3.8%	3.7%	3.6%	3.5%
15%	8.1%	8.1%	8.0%	7.9%	7.8%	2.8%	2.8%	2.8%	2.7%	2.6%
10%	5.4%	5.4%	5.3%	5.3%	5.2%	1.9%	1.9%	1.9%	1.8%	1.8%
5%	2.7%	2.7%	2.7%	2.6%	2.6%	0.9%	0.9%	0.9%	0.9%	0.9%

Table 3.2 Maximum potential sliding mass relative to total building mass

3.2 Computational Model:

To evaluate the impact of sliding masses on a building's response, a simplistic model separating affixed and sliding mass is developed. The basis of the results presented here come from a linear shear building model coupled at every floor with a nonlinear spring element that is attached to a portion of the

total floor mass (Figure 3.2). A floor's total mass (M_T^n) is defined as the sum of the permanently affixed (M_a^n) and the sliding mass (M_s^n) on floor *n*. The sliding mass ratio (SMR) is defined as the ratio of M_s^n to M_T^n. Note, all floors in the study have the same SMR for any particular analysis (mass is evenly distributed to every floor from both the rigid and sliding perspective).

The nonlinear axial spring is elastic - perfectly plastic with an initial stiffness of 100x the floor's shear stiffness. The stiffness of the nonlinear spring is high to represent a rigid diaphragm constraint for all potential sliding mass. The plastic capping force is then varied based as a percentage of the "slidable" masses' self weight to simulate overcoming varied levels of friction forces. This restraining force is then held constant until the inertial force on any sliding mass is below the plastic capacity (Columb damping).

If static and kinetic friction values are known throughout a system, then a more suitable model would be an elastic, reduced plastic element. We do not claim to know the relationship of all these materials with enough rigor to attempt to quantify this parameter precisely, and merely use the simplification of Coulomb damping to represent the physics of the problem more generally.

The nonlinear spring element on every floor serves two purposes. During low levels of excitation, mass is not expected to overcome the static friction forces associated with a ground motion. This implies that the mass moves with the floor, and no sliding is occurring. Alternatively, if the excitation is violent enough, it is expected that masses will begin to slide across surfaces, and thus decouple from the floors motion (the floor will slide beneath the mass).

Energy dissipation in the model comes from sliding mass and a modal damping damping strategy of the first primary lateral modes (See Figure 3.3). For this study, a constant damping of 2% is used for all translational modes in the system. Using this basic model, we study a suite of different building heights/stories (N) and proportions of sliding mass.

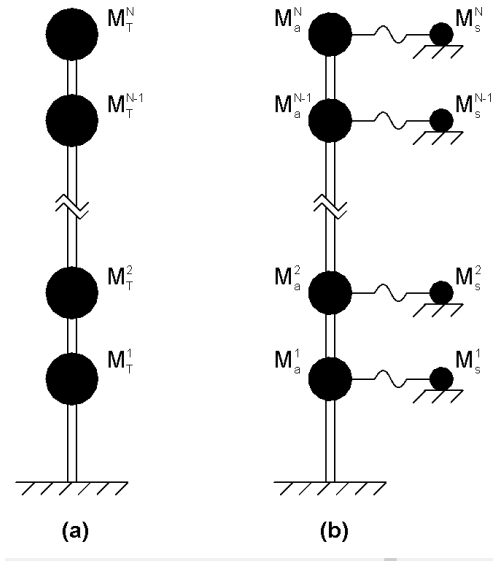

Figure 3.2 Computational model for (a) no sliding mass and (b) sliding mass model where $M_T^n = M_a^n + M_s^n$ with nonlinear fuse element.

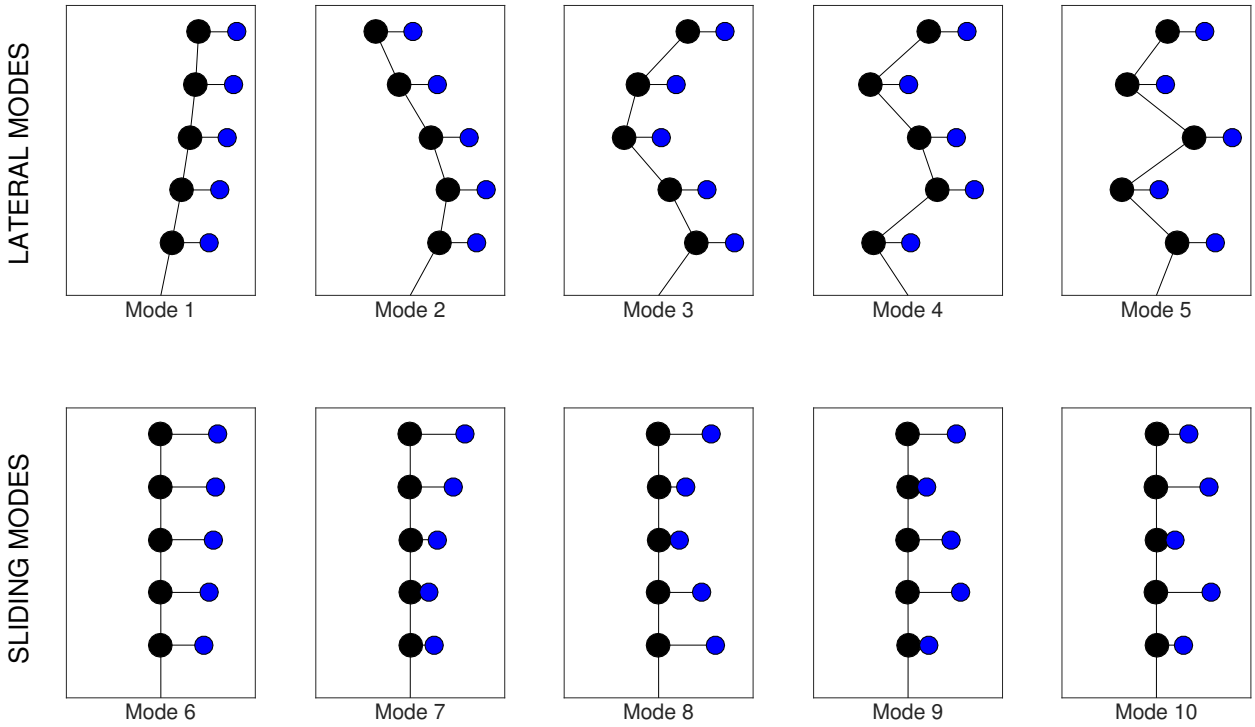

Figure 3.3 Lateral and sliding modes of the system. Lateral modes are used exclusively in constructing the modal damping matrix.

The modal damping strategy is well established (Powell, 2011) and is presemted here for completeness as well as clarification of the separation of modal energy and sliding energy. There are two types of modes in the system: first, low frequency modes where the floors masses all move together, and

second, very high frequency modes which excites the sliding mass nearly independently. The damping matrix for the system is created from the primary lateral modes of the system when sliding is not occurring (See Figure 3.3). The modal damping matrix is defined as

$$\bar{C} = \sum_{i=1}^{L} \frac{4\pi}{T_i} \xi_i \frac{(\bar{M}\phi_i)(\bar{M}\phi_i)^T}{\phi_i{}^T \bar{M} \phi_i} \tag{3.1}$$

where $\bar{C}$ is the damping matrix, $\bar{M}$ is the mass matrix, i is the ith mode of the system, L is the total number of lateral modes, T_i is the modal period, ξ_i is the ith mode's damping ratio, and ϕ_i is the ith mode shapes. Viscous energy (E_v) is calculated as

$$E_v = \int_0^x F\, dx = \int_0^x \bar{C}\dot{u}\, dx = \int_0^t \bar{C}\dot{u} \cdot \dot{u}\, dt \tag{3.2}$$

where u is the vector of displacements and the over-dot represents the time derivative. Similarly, the sliding energy (E_s) is determined as the energy lost in the plastic sliding of the damper summed continuously as

$$E_{s_{(i)}} = E_{s_{(i-1)}} + \sum_{e=1}^{z} \begin{cases} if\ f_e > f_y & \left| f_y * \left|(\Delta u_{i\_e} - \Delta u_{(i-1)\_e}\right| \right. \\ else & 0 \end{cases} \tag{3.3}$$

where e is the element number, z is the total number of nonlinear elements, and Δu_{i_e} is the differential displacement between the sliding mass and the core structure at time i.

3.3 Analysis results

The computational study was conducted on a series of shear building structures whose primary lateral systems are assumed to remain linear. The initial structural periods of the structures are summarized in Table 3.4.

	Stories				
Mode	3	5	10	15	20
1	0.404s	0.632s	1.204s	1.777s	2.349s
2	0.144s	0.217s	0.404s	0.594s	0.785s
3	0.100s	0.137s	0.246s	0.359s	0.473s
4		0.107s	0.180s	0.259s	0.340s
5		0.094s	0.144s	0.204s	0.266s

Table 3.3 Building periods for computational study

Each structure has a varying percentage of its floor level mass allowed to potentially slide (5%-25%) with varying levels of capping friction force (5% - 100%) in each analysis. The study was conducted using the El Centro – Terminal Station earthquake ground motions (Figure 3.4), as well as the Northridge - Rinaldi Station (Figure 3.5). These results consist of 1,000 total analyses (100 for each building for two separate ground motions) to show the gradation of effect for both stiff and flexible structures with varied amounts of sliding mass and static friction force limits. All viscous damping is done using modal damping set to a constant 2% for all modes.

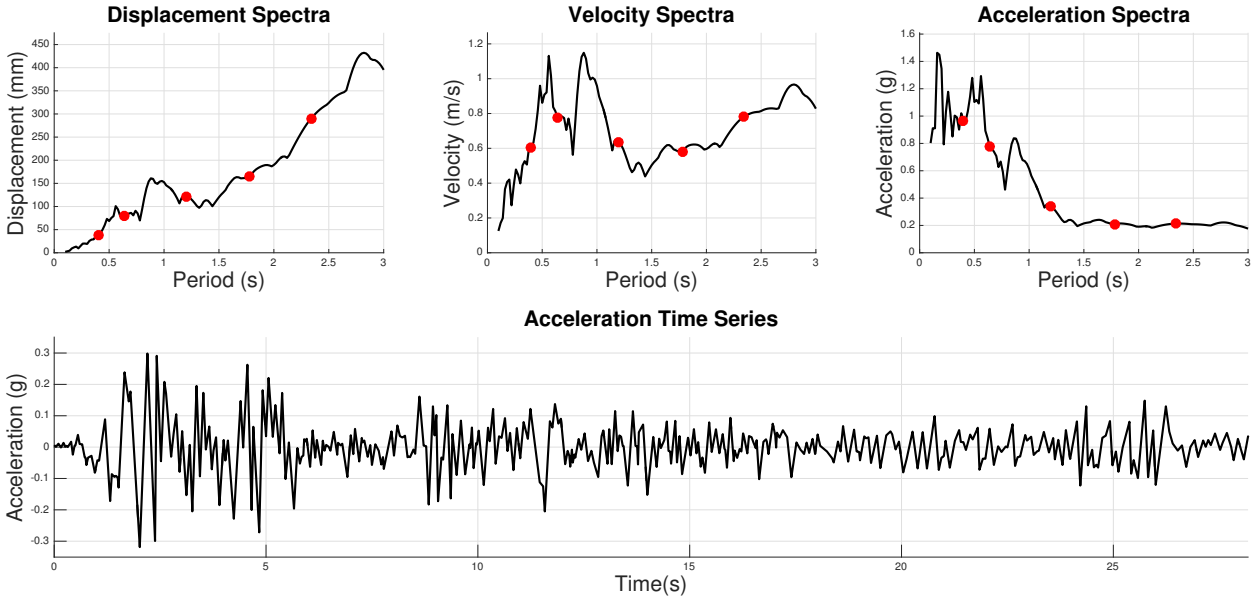

Figure 3.4 1940 El Centro earthquake and associated displacement, velocity, and acceleration spectra based on 2% damping. Red markers on spectra indicate first mode of archetype buildings.

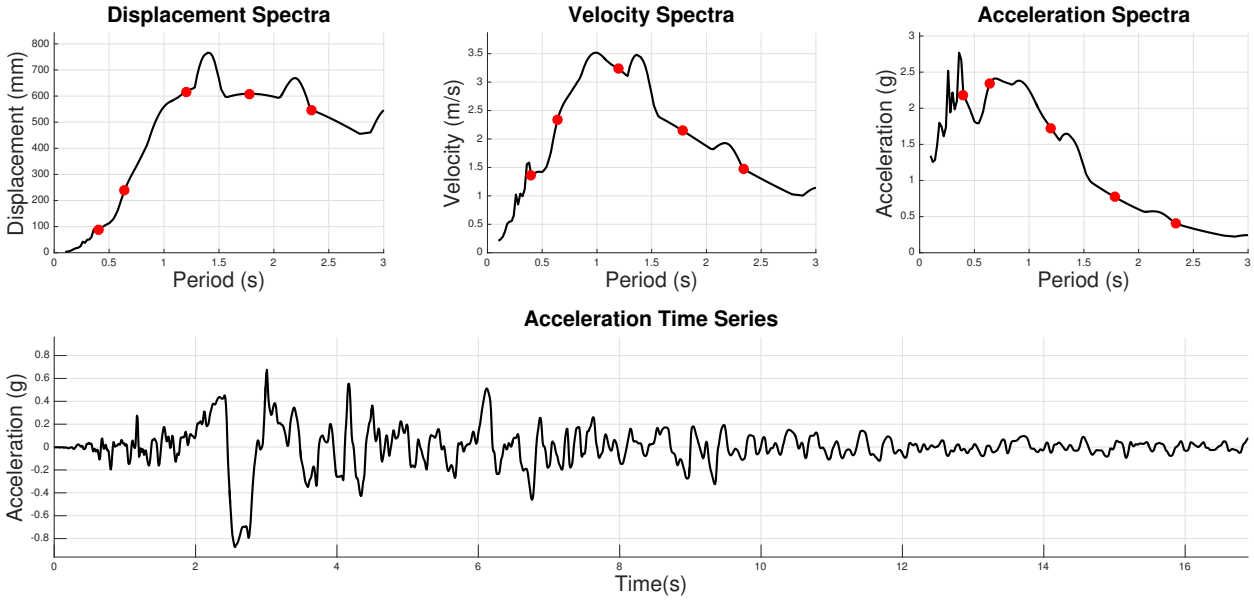

Figure 3.5 1994 Northridge earthquake measured at Rinaldi Station and associated displacement, velocity, and acceleration spectra based on 2% damping. Red markers on spectra indicate first mode of archetype buildings.

For every run of the analysis, deformation and energy peak responses are stored. This allows for the comparison of peak roof displacement over the analyses, as well as comparisons of energy dissipation mechanisms (traditional viscous energy compared to energy removed through sliding mass). This energy comparison allows the study of relative amount of energy contributions from either component of the system.

As an example of the effect of sliding mass on linear structural response, when a three (3) story building has no sliding mass (SMR=0) as opposed to an SMR of 0.25 with a sliding force ratio of .25g, the El Centro ground motion affects the roof displacement response history (Figure 3.6). The peak roof displacement reduces by more than 17%, but also, the time of occurrence for the peak has changed significantly, happening two cycles earlier. At the original peaks time of occurrence, the difference is even more pronounced (greater than 30%). Similarly, for the same scenario, Figure 3.7 shows how energy is dissipated in the system. Note an overall diminishing of the total energy dissipated when sliding mass is included (91.2% of the energy compared to SMR=0).

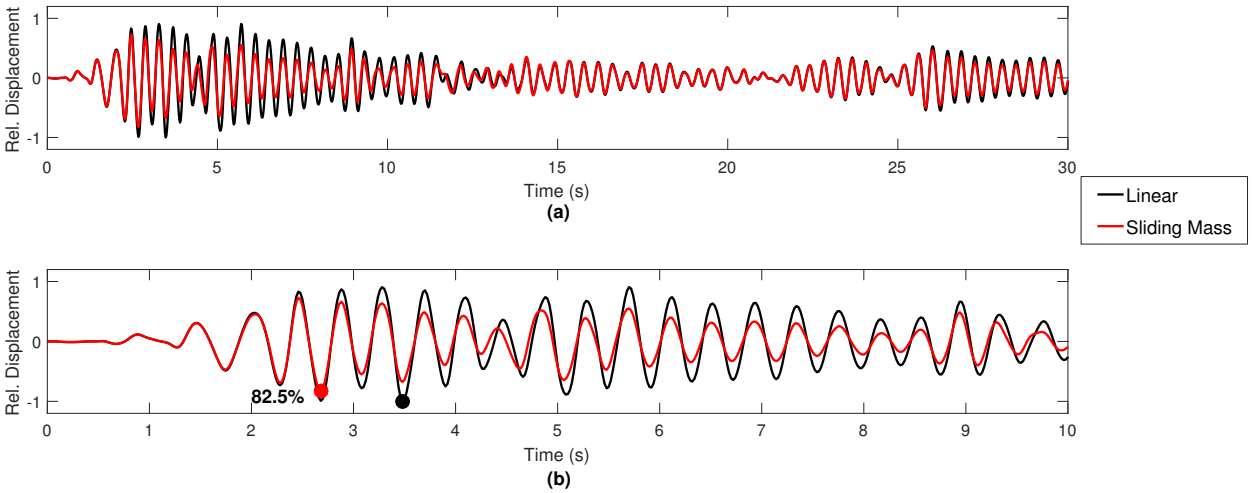

Figure 3.6 (a) Roof displacement response for a three (3) story building with no sliding mass compared to one with an SMR of .25 and a yield force of .25g associated with the mass subject to the El Centro Earthquake of 1940. (b) Enhanced view of same information highlighting maximum values and differences in response.

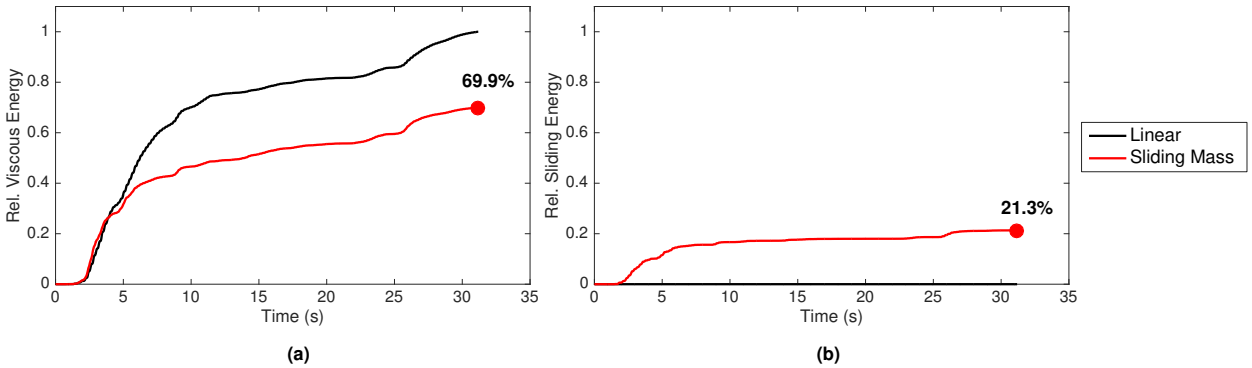

Figure 3.7 - Comparison of (a) viscous vs. (b) sliding energy for a three (3) story building with no sliding mass compared to one with an SMR of .25 and a yield force of .25g associated with the mass both subjected to the El Centro Earthquake of 1940.

Taking these peak parameters from each individual study, the results are compiled into the following figures (Figure 3.8 to 3.11) to make more general statements about the effects of sliding masses on response. The peak contributions are compared to the linear system to give scale to the sliding effect being studied relative to no contribution from sliding mass.

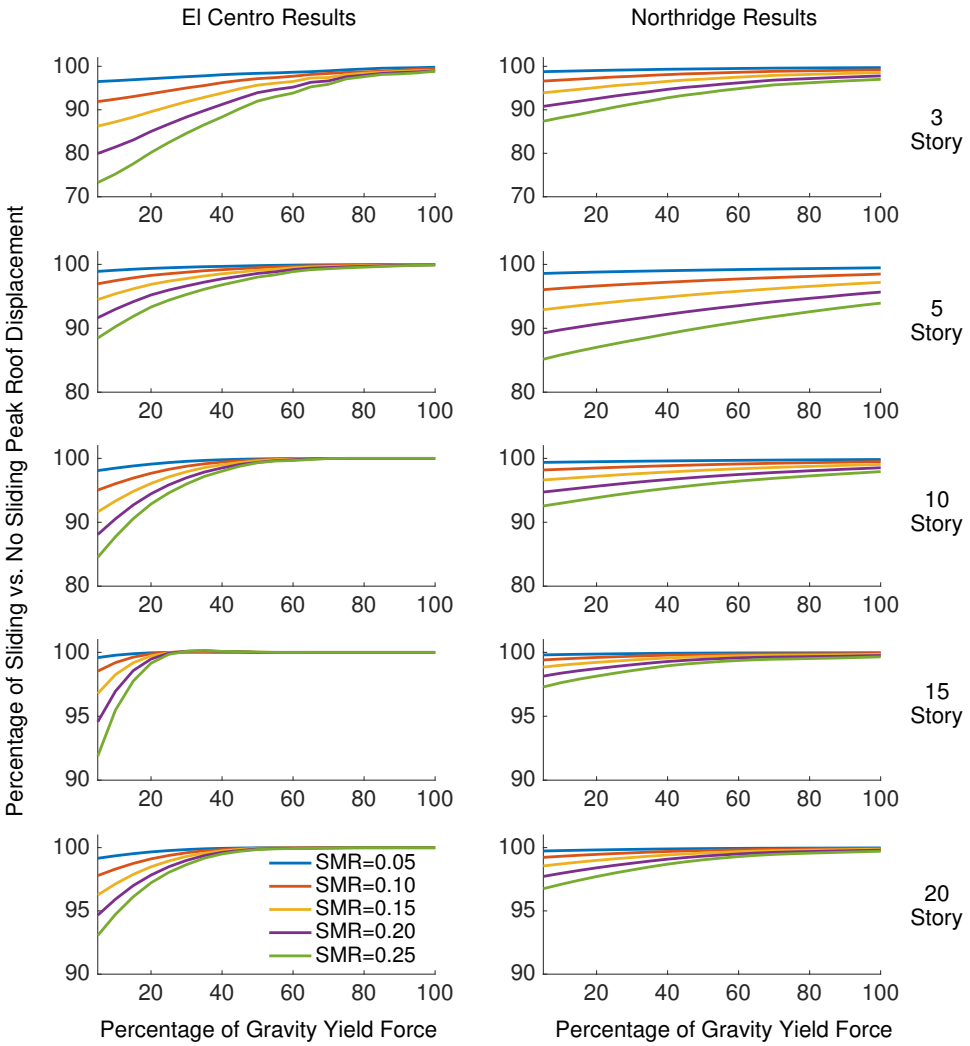

Figure 3.8 Summary of percentage of peak roof displacement when normalized to linear analysis without sliding. El Centro (left) and Northridge (right) ground motions with varying levels of SMR and the percentage of gravity weight yield force.

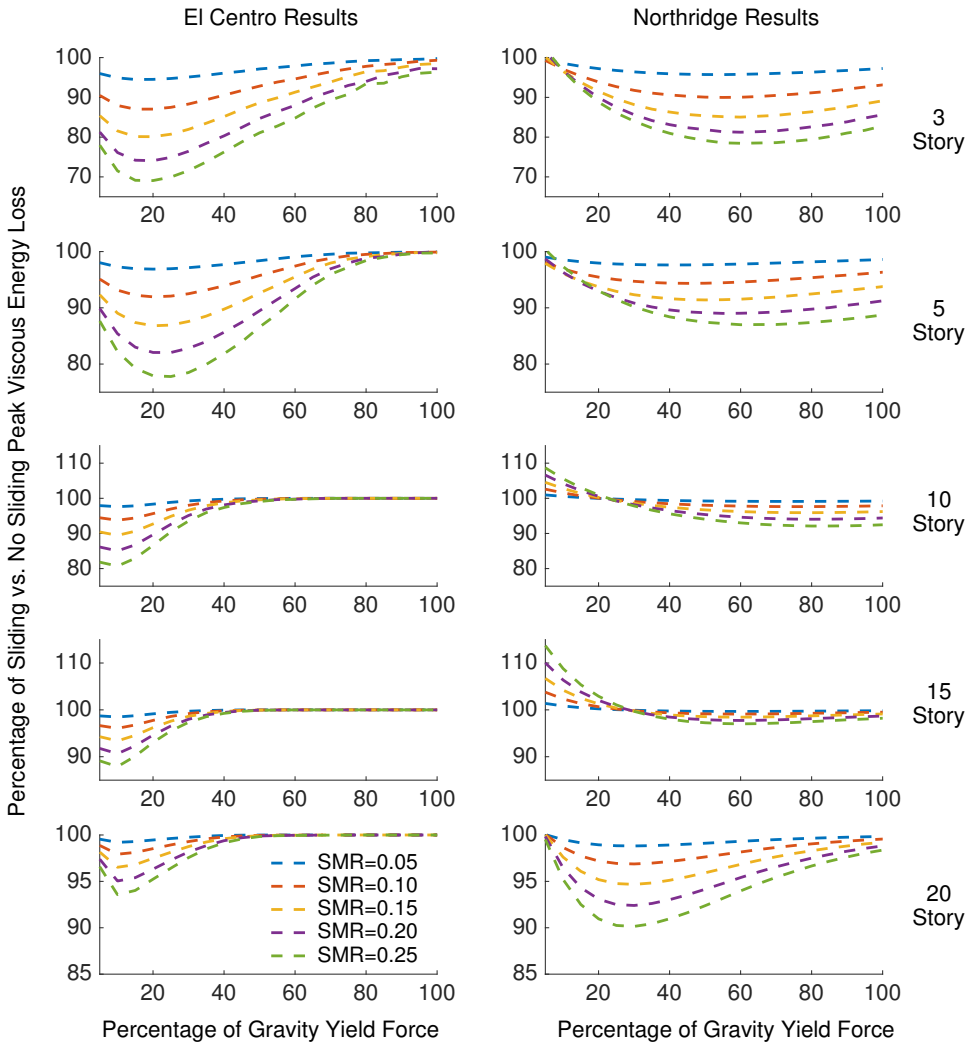

Figure 3.9 Summary of percentage of viscous damping energy when normalized to linear analysis without sliding. El Centro (left) and Northridge (right) ground motions with varying levels of SMR and the percentage of gravity weight yield force.

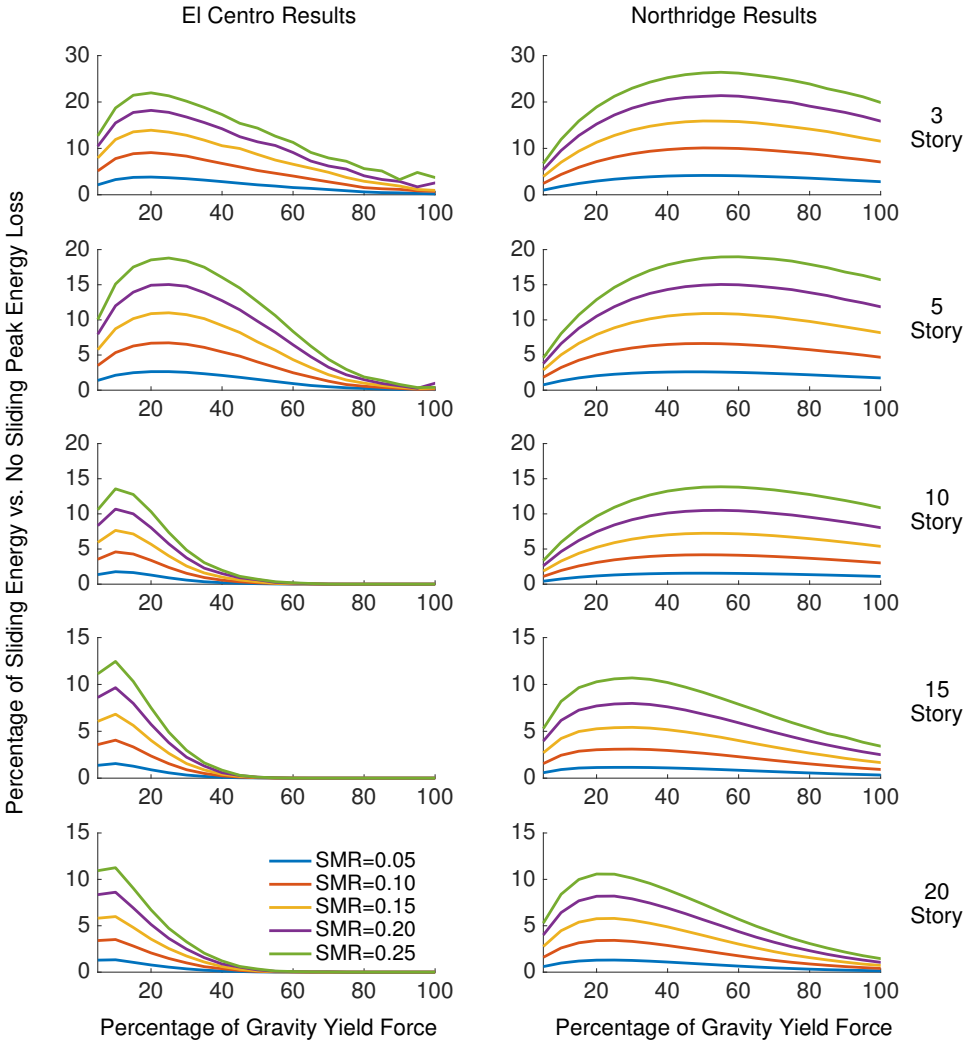

Figure 3.10 Summary of percentage of sliding energy when normalized to linear analysis without sliding. El Centro (left) and Northridge (right) ground motions with varying levels of SMR and the percentage of gravity weight yield force.

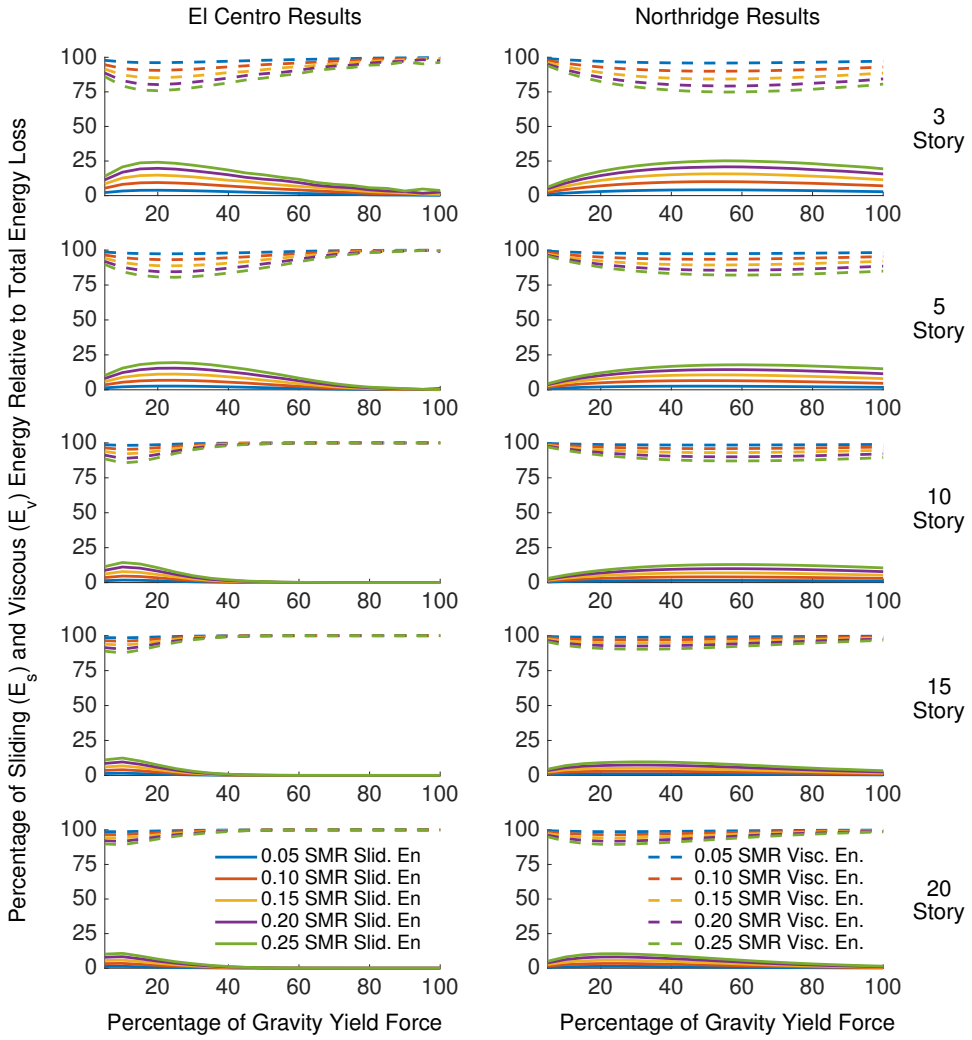

Figure 3.11 Summary of viscous damping and sliding energy compared to one another on a particular run. El Centro (left) and Northridge (right) ground motions with varying levels of SMR and the percentage of gravity yield force.

3.4 Discussion

By evaluating the results shown in the previous section, a series of observations can be made. As the quantity of mass available to slide increases, the variation of the peak roof displacement response of the structure becomes more pronounced (Figure 3.8). Further, as the friction force overcome to engage sliding is increased, we approach a condition where little to no effect in peak roof displacement is observed, as the mass tends to remain coupled with the main structural system (as is expected).

More interesting is the ground motion specific characteristics identified. For instance, one would expect the overall contribution to energy dissipation from modal damping would be maximum when all the mass in the system was unable to slide; however, in cases such as the ten (10) story structure

subjected to the Northridge ground motion, it is observed that the viscous energy could potentially increase with sliding mass (Figure 3.9). This is associated with a shift in the natural period of the structure when mass slides, which potentially create scenarios where a structure might have a more pronounced response (with respect to viscous energy). This can be observed in the velocity spectra of the ground motion (Figure 3.5) where a decrease in period of the ten (10) story structure increases the amplitude of the spectral velocity. In cases where masses can easily slide (intentional decoupling), this effect may be significant.

Also of interest is the transition in behavior of the amount of energy removed by sliding mass. When the mass is allowed to freely move (minimal yield forces) the amount of energy potentially available for sliding in a ground motion is not at its pinnacle. Having some level of coupling allows the mass to develop momentum in a direction, leading to higher initial velocity as opposed to the ground just shifting beneath it. Further, the larger the friction force, the more energy that can come out of the system over the same velocity based excursion.

The overall effects are more pronounced on shorter period structures as opposed to more flexible systems (seen in Figure 3.8 through Figure 3.11). This indicates the high frequency nature of this phenomena overall, as we assume the stiffness of the elastic perfectly plastic structure is quite high (minimal motion until slip). However, there are instances where a longer period system would make sense, for instance, masses that would tend to rock instead of slide would typically be longer period structures and would have potentially more pronounced effects in taller buildings. Rocking; however, is a very different phenomenon, and not within the scope of this study, and mentioned only for consideration of future work in secondary component effects to overall structural response.

For shorter structures, the peak differential in elastic response was greater than 10% for the largest amount of sliding mass studied. Note again that multi-story data centers, which could have potentially even more sliding mass, are becoming common in locations where land values are high. Variations this large in analysis results of high performance structures can have significant design impacts that should be realized by the engineer, if not quantified.

3.5 Conclusion

There are many secondary effects associated with nonstructural components in building systems. Studies often address the stiffness and energy dissipation available in the element/components that are

restrained and coupled with other structural components (such as partitions and piping). Alternatively, smaller and/or free components with the potential to slide/lose coupling or rock are often studied to determine component damage or fragility directly.

Here we focused specifically on nonstructural components which are not restrained to structures and the potential effect on the response of a building as a whole. Based on the results of the computational study performed, a series of observations can be made:

1) Shorter/stiffer structures tend to see a larger variation in response due to the high frequency nature of the phenomena of overcoming the maximum static force before sliding.
2) More mass available to slide tends to lead to smaller displacements in the ground motions used in this study. From the perspective of the displacement spectra and conceiving of the sliding mass as a reduction in the structural mass, a shift to a lower period structure and experiencing a lower peak displacement in an elastic system is as one would expect.
3) There is a strong dependence on ground motion characteristics and magnitude of sliding effect on response as well as when certain energy contributions are maximum. This should be evaluated for a more robust set of ground motions to determine dependencies.
4) Energy dissipation, and therefore measured damping, can have a significant portion of the energy loss associated with components sliding in a structure, and not necessarily associated with structural damage. This type of energetic loss is not typically modeled; however, it can prove to be significant in certain architectural usages where large amounts of mass are decoupled from the structural system (ex. data centers).

3.6 Future work

This study focused on determining if there was potential for sliding mass to contribute in a significant manner to the response of structures. This was accomplished by using a rudimentary Coulomb damping model. More complex models exist which may prove to be more realistic in a particular application. Specific studies into varied friction models, and other secondary component behaviors and their effects on the global performance of a structure are of interest. Similarly, ground motion dependence on the response shows a need for a more robust study with additional ground motions to understand the effect statistically. Additionally, introducing structural nonlinearity into the problem to understand the total effect on a yielding structure would prove advantageous.

3.7 References

Eduardo Miranda, Gilberto Mosqueda, Rodrigo Retamales, and Gokhan Pekcan, "Performance of Nonstructural Components during the 27 February 2010 Chile Earthquake" *Earthquake Spectra*, Volume 28, No. S1, pages S453–S471, June 2012

Samit Ray Chaudhuri and Roberto Villaverde, "Effect of Building Nonlinearity on Seismic Response of Nonstructural Components: A Parametric Study" *J. Struct. Eng.*, 2008, 134(4): 661-670

D Konstantinidis, F Nikfar, "Seismic performance of sliding contents in base-isolated buildings" *Proceedings of the 10th National Conference in Earthquake Engineering, Earthquake Engineering Research Institute*, Anchorage, AK, 2014.

Powell, G. H. (2011) "Perform 3D User Guide", *Berkeley: Computers and Structures Inc.*

Ray Chaudhuri, S. and Hutchinson, T. C., "Characterizing frictional behavior for use in predicting the seismic response of unattached equipment" *In Proceedings of the 11th International Conference on Soil Dynamics & Earthquake Engineering (SDEE)*, pages 368–375, 2005

Atlanta Business Chronicle, "Google plans more than 800,000-square-foot data center in metro Atlanta" <http://www.bizjournals.com/atlanta/blog/atlantech/2015/07/google-plans-more-than-800-000square-foot-data.html> , 2015

Earthquake Test Lab – Japan <https://www.youtube.com/watch?v=vDsmBDk9v0M>, Apr 6, 2015

Malushte, S., Whittaker, A. – "Survey of past isolation applications in nuclear power plants and challenges to industry/regulatory acceptance" 18th *International Conference on Structural Mechanics in Reactor Technology (SMiRT 18)* Beijing, China, August 7-12, 2005

Hutchinson, T.C., Restrepo, J.R., Conte, J.P., Pantoli, E., Chen, M., Wang, X., Astroza, R., and Ebrahimian, H.. "Shake table testing of a five story building outfitted with NCSs (BNCS project)". *Network for Earthquake Engineering Simulation (NEES)*(distributor). Dataset. DOI: 10.4231/D38W38349, 2014

Lee,T.H., Kato, M., Matsumiya, T. Suita, K., Nakashima, M, "Seismic Performance Evaluation of Non-structural Components: Drywall Partitions" *Earthquake Engineering and Structural Dynamics* 2007l 36:367-382 DOI:10.1002/eqe, 2007

W.H. Chong and T.T. Soong, "Sliding Fragility of Unrestrained Equipment in Critical Facilities" *Technical Report MCEER* 00-0005, ISSN 1520-295X, 2000

Lopez Garcia, D. and Soong, T. T., Sliding fragility of block-type non-structural components. Part 1: Unrestrained components. *Earthquake Engng. Struct. Dyn.*, 32: 111–129. doi:10.1002/eqe.217, 2003

Lopez Garcia, D. and Soong, T. T., Sliding fragility of block-type non-structural components. Part 2:

Restrained components. *Earthquake Engng. Struct. Dyn.*, 32: 131–149., 2003

C h a p t e r 4

MODIFIED PROCEDURE FOR THE DESIGN OF SECONDARY INTERMEDIATE MOMENT FRAMES FOR BUILDING STRUCTURES

4.0 Introduction

Current code provisions in the United States (IBC, 2012) require that special concentrically braced frame (SCBF) structures over a certain height in high risk seismic conditions (such as those in the western United States) be limited in height unless constructed with a secondary intermediate moment frame. The key metric for determining SCBF building height limitation applicability is the Seismic Design Category (SDC). The SDC is based on site location earthquake hazard levels (S_s and S_1 values), site specific soil properties (F_a and F_v) and Occupancy Category (I, II, III, IV). The goal of the SDC is to classify a structure based on its risk category and the severity of the design earthquake ground motion (ASCE 7, 2010) which is independent of the structural system chosen. The SDC is then used to filter structural systems and determine if they are limited in height, not permitted (NP), or unrestricted in height (NL). For example, less ductile systems, such as unreinforced masonry structures, have severe height limits or may not be permitted (NP) to be constructed at all. Alternatively, other highly ductile systems (ex. special moment frames) have no height limitations (NL). In theory, the idea of minimized risk is achieved by penalizing more susceptible brittle structures with respect to the earthquake hazard and rewarding more ductile systems.

While the intent is sound, a very restrictive portion of the building code is that no steel braced frame system is permitted to be constructed without height restriction in SDC-D or worse. For structures falling into these categories, a lateral design scheme incorporating a secondary intermediate moment frame is required. Further, this moment frame is required to have a certain level of robustness, mandated to carry 25% of the total prescribed seismic forces in the supplemental system regardless of the interplay in stiffness between the two systems. This “25 percent frame” is meant as a secondary lateral system with higher degrees of redundancy and ductility in order to improve the ability of the building to support the service loads after strong earthquake shaking (NEHRP Commentary C12.2.5.1). Figure 4.1 shows the undeformed versus deformed condition of a braced frame emphasizing common types of nonlinear mechanisms that can develop after strong shaking such as brace buckling and tension rupture. These types of local failure mechanisms can cause a significant reduction in the building’s overall ability to remain stable.

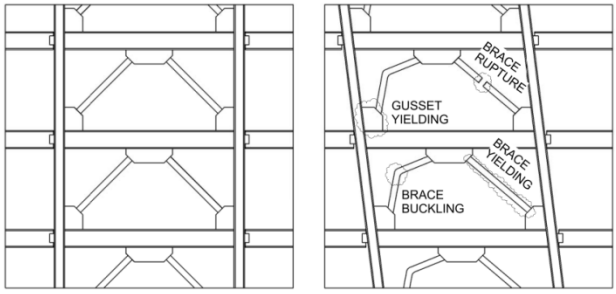

Figure 4.1 Predominant Braced Frame Nonlinear Mechanisms

NEHRP (BSSC, 2009) clearly states in the commentary that the height limit is based primarily on "subjective judgment." There is also little commentary provided as to support the notion that using 25% of the effective base shear for the design of the intermediate moment frame will ensure structural stability under service gravity loads. Further, there are qualitative arguments that taller structures should be more robust as there is a larger risk to property and human life; however, this is meant to be an issue of occupancy and importance as the code is written.

The behavior of braced frame and moment frame structures is well studied (Hall, 1997; Sabelli et. al., 2013; Hamburger, 2009); however, dual systems have more complex behavior and are less often studied. To independently examine the mechanical differences between braced frame, moment frame, and dual systems, we designed a 20 story office building using modern day building code requirements (IBC 2012) in Los Angeles (Figure 4.2 and Appendix C). Quasi-static pushover analysis was performed that included P-delta stiffness reduction as well as large displacement nodal updating techniques. All component level nonlinear effects were represented computationally using FEMA 441 hinge criteria for beams, columns and braces. The analysis does not take advantage of secondary framing elements (gravity framing) for stiffness and merely relies on the prescribed lateral system for resistance to eliminate confusion and complexity. For simplicity, a 2D model with an equivalent P-Delta column is used for lost frame weight.

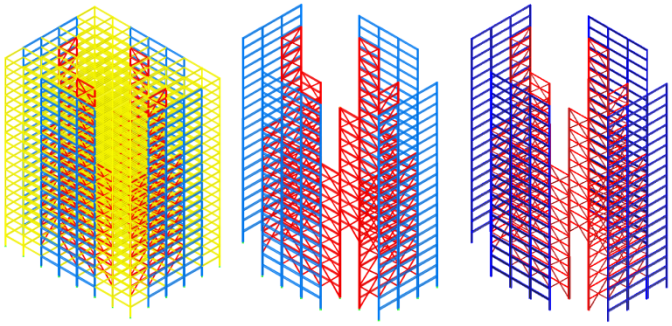

Figure 4.2 Complete 3D ETABS Model, Isolated ETABS Model, and BIM Model of 20 Story Dual System

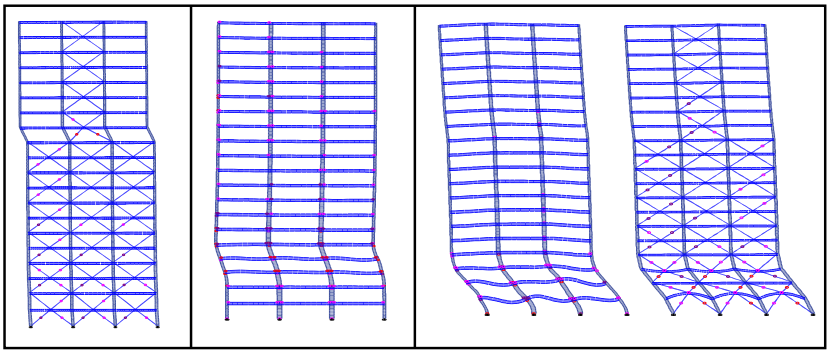

Figure 4.3 Deformed Configuration of Braced Frame, Moment Frame, and Dual Frame from Quasi-Static Pushover

Figure 4.3 shows that the dual system, at large displacements, has nonlinear response in both the moment and braced frame components of the structure. When braced and moment frame systems are separated, the braced frame structure has a tendency to develop a weak upper story leading to collapse. This mechanism is reinforced by the moment frame (which has significantly more ductile capacity) in the dual system and allows the structure to achieve larger total drift before reaching a localized P-Delta instability, adding to the overall ductility of the structure. This "reinforcing" of mechanisms is one of the benefits of dual systems overall; however, the intended post-event stability of the system is yet to be established.

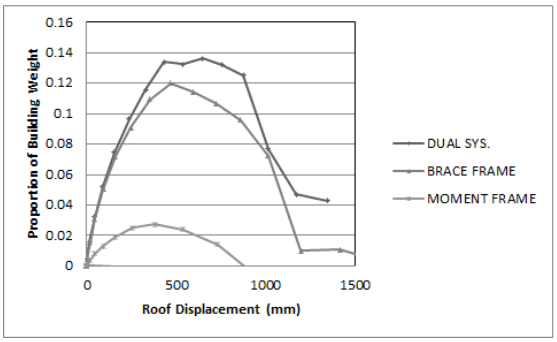

Figure 4.4 Pushover Curve Comparing Effects of Dual System Components

This chapter focuses on developing a more prescriptive method of determining design forces for structures in their post-event plastically deformed state (See Figure 4.5) and maintaining stability. The concept of gravity based, so called "P-Delta" moments, is used to develop a prescriptive method for developing design forces that are consistent with the building code's intent.

The scale to which P-Delta moments exist in a system was examined by prescribing code based deformation limits and observing the induced demand. Working with these responses, a procedure for developing a stabilizing strength/stiffness for that system is presented.

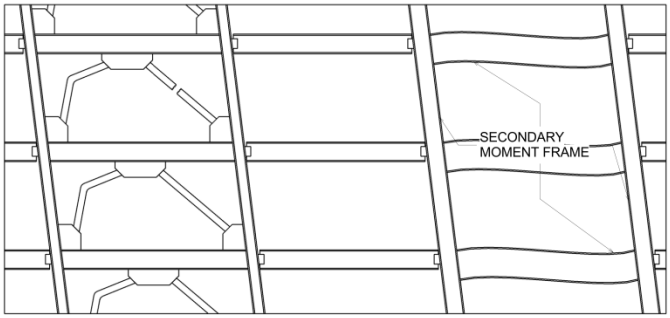

Figure 4.5 Dual System with Braced Frame in Damaged State and Secondary Moment Frame

4.1 Code Based Deformation Demands and Limits

ASCE 7-10 is prescriptive in the determination of peak displacement demands on a system, as well as to what the limits are for this demand. Given a location, building type, and usage, the code determines an inelastic spectrum for design. The design spectrum takes into account the perceived ductility of the system by taking the appropriate local elastic spectra and dividing by a system based "R-factor" to represent the structure's reduced forces in the nonlinear regime (See Figure 4.6). The reduced scale response spectra are then used for design of the lateral system by either response spectrum analysis, equivalent lateral forces, or in some circumstances time-history analysis.

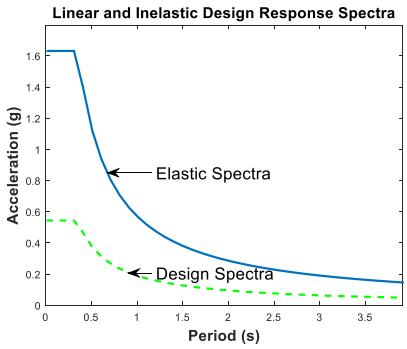

Figure 4.6 Code Based Response Spectra Implemented in Design of Building Structures

Performing a linear elastic analysis, the design spectra (Figure 4.6) uses the elastic period of the structure to determine the applicable earthquake forces. The design spectrum assumes that there will be some inherent non-linearity in the system that will "soften" the structure and allow for a reduced set of forces as opposed to the elastic spectra. As such, elastic displacements due to these reduced forces are artificially increased by a ductility factor "C_d" which is meant to account for this structural softening leading to higher inelastic displacements (note, importance factor, I_e is removed when determining inelastic demands from elastic displacement amplification). This inelastic displacement is what is limited by the code to prescriptive values, which are based on risk category (usage) and structural type. Excluding masonry structures and buildings less than 4 stories from this study, we examine the 4 risk categories and the limits on inelastic drift prescribed in ASCE 7-10 Table 12.12-1 (See Table 4.1). Here h_{sx} represents the story height below level "x" and Δ_{max} represents the maximum inelastic story drift allowed by the seismic provisions.

	Risk Category		
	I or II	III	IV
Δ_{max}	$0.020h_{sx}$	$0.015h_{sx}$	$0.010h_{sx}$

Table 4.1 Summary of ASCE 7-10 Table 12.12-1 Drift Limits

The prescribed limits were used to investigate various scenarios for typical building structures that have been taken to their maximum inelastic displacement demands over their height to establish a design approach for structural stability.

4.2 Simplistic Evaluation Using Code Maximum Inelastic Deformed Shape and Subsequent P-Delta Demand

Given the drift limits in Table 4.1, P-Delta stability is explored by making basic observations of what these requirements imply. As the code's intent is to have a structure that is stable after an

earthquake which has pushed the structure into the inelastic deformed shape, elastic recovery is assumed minimal, and a deformed configuration maximum is assumed in the following sets of data (See Figure 4.7a). Additional analysis representative of flexural and shear elastically deformed shapes are also performed, assuming uniform floor weight and the appropriate curvature, to determine the effects of varied drift over the height (See Figure 4.7b).

In terms of P-Delta moments, it is clear that the intent of more stringent building drift criteria, with respect to its Risk Category, should have smaller permanent inelastic deformation than lower risk structures. These lower magnitudes of P-Delta moment suggest a potential for economy in secondary systems of such structures.

To evaluate the P-Delta moments for typical structures adhering to the code provisions to the most extreme extents possible, a linear maximum story drift over all floors equal to the maximum allowed by ASCE 7-10 is studied (See Figure 4.7a).

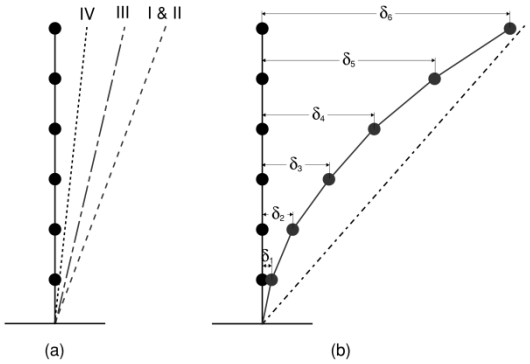

Figure 4.7 Deformed Shape Limits & Typical Deformed Shape

As the secondary moment frame does not come into play until a structure is over a height of 73.2m (240ft) (assuming typical vertical regularity) focus is made on a typical story height of 3.96m (13ft) and 20 stories tall thereby consisting of a 79.25m (260ft) tall building structure. All floors are assumed to have a similar weight (denoted P).

Every floor will have its own displacement δ_j that will be a function of the story height multiplied by the code mandated maximum drift level (Δ_{max}). Given this, every floor's contribution to the base overturning moment is simply:

$$M_{base_j} = P \times \Delta_{max} \times Elev_j \tag{4.1}$$

where:

$Elev_j$ is the floor elevation of the "jth" floor (See Figure 4.8)

However, what is more pertinent is what the contribution of the summation of the entire load above the building is to the overturning moment along the length (assuming typical floor height "h" and "N" being the total number of floors).

$$M_j = P \times h \times \Delta_{max} \times \sum_{i=j+1}^{N} (N - i) \tag{4.2}$$

This approach results in a moment diagram whose growth increases linearly between each story but more rapidly as additional stories are continuously added to the structure. This is demonstrated in Figure 4.9 where a pre-deformed structure conforming to the maximum drifts stipulated by ASCE 7-10 for the various risk categories is loaded vertically with unit point loads. Figure 4.9 shows the growth in the moment diagram with respect to the uniform slope of the structure taking a non-linear increase over the height. Given this nonlinear growth, there is an implied variation in the shear over the height of the structure towards the base.

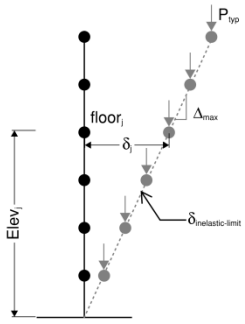

Figure 4.8 Model Configuration for Floor Variables

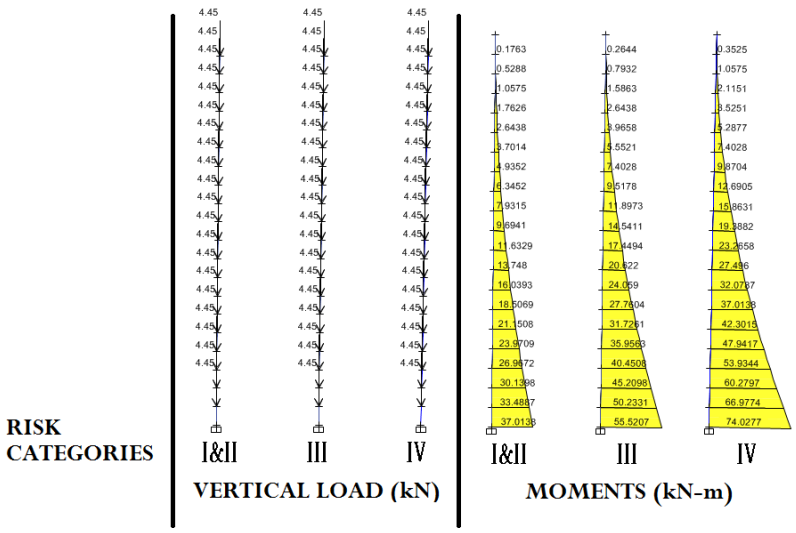

Figure 4.9 Gravity Induced P-Delta Moments under Uniform Vertical Load for Varied Risk Categories (kN-m)

To develop the equivalent horizontal forces which mimic this moment diagram (Figure 4.9), and overall demand on the system, the analysis must resolve the static equilibrium of a sloped column element. Sloped columns induce shears on a floor-by-floor bases which are not fully resolved by the floor below due to the increased weight of the newest level (See Figure 4.10).

The applied forces resolve at the floor level to give the difference in displacement of the floor above by the floor below divide by the height, times the weight of the floor, but this can be simplified to the drift times the floor weight for this displacement model:

$$H_j = P \times \frac{\delta_j - \delta_{j-1}}{h_j} = P \times \Delta_{max} \tag{4.3}$$

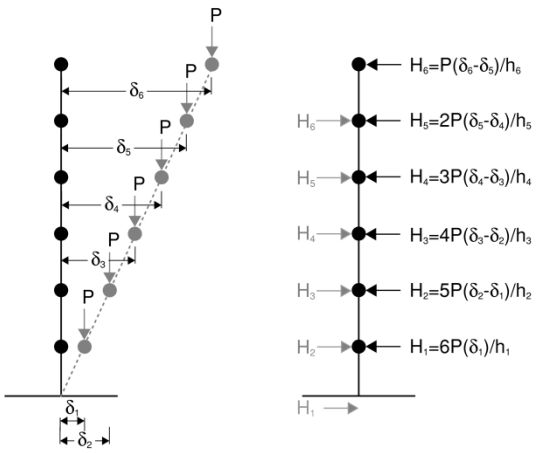

Figure 4.10 Drift Based P-Delta Equivalent Lateral Forces

Applying this set of forces to the typical structure (See Figure 4.11) an equivalent moment diagram to the induced gravity P-Delta moments (See Figure 4.9) is observed. The force applied in this extreme case of full inelastic displacement over the entire height of the structure (assuming uniform floor weight) leads to a uniform horizontal applied force of the floor weight times the drift. This would suggest that the base shear for each of the 4 occupancy categories is simply the weight of the building times the maximum drift. Note this distribution is nothing like the seismic load distribution assumed in ASCE 7-10, which is weighted more heavily at the top of a structure.

$$Base\ Shear = Weight \times \Delta_{max} \tag{4.4}$$

Table 4.2 summarizes the equivalent base shear in the building distributed uniformly over the height of the structure.

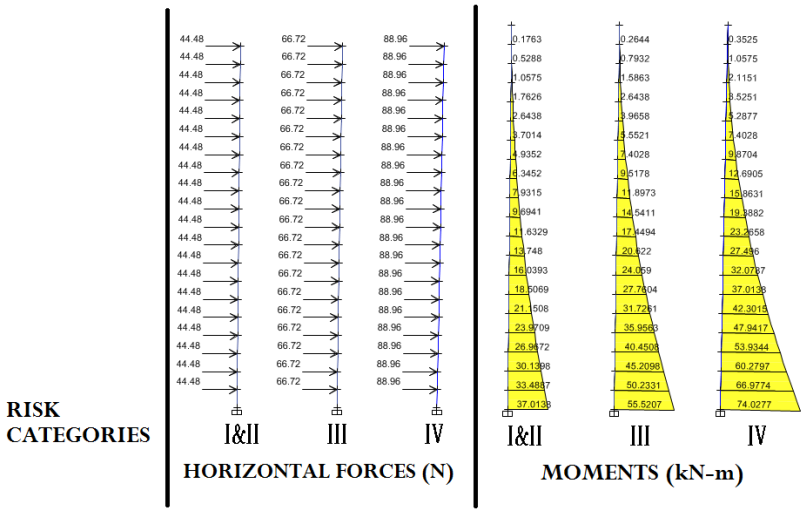

Figure 4.11 Equivalent Horizontal Forces and Moment Diagram Consistent with Figure 4.9

	Risk Category		
	I or II	III	IV
V_b	2% W	1.5% W	1% W

Table 4.2 Full Building at Maximum Inelastic Displacement Proposed Total Base Shear

4.3 Evaluation Using Code Maximum Inelastic Deformed Shape and Subsequent P-Delta Demand on the System Incorporating Varied Floor Weight and Story Height

The distribution above has a series of assumptions but represents the most basic approach to what the maximum base shear would be for a uniformly weighted structure. Abandoning these assumptions but applying the same displacement field, the j[th] floor moment equation becomes more complicated and requires constructing a vector of elevations be formulated into

$$M_j = \sum_{i=j+1}^{N} P_i \times (elev_i - elev_j) \times \Delta_{max} \tag{4.5}$$

The floor-by-floor force also needs to be updated, but due to cancelation of components from floors above and similar slopes, the result simplifies to Eq. 4.6 with special conditions for the roof ($\delta_{N+1} - \delta_N = 0$).

$$H_j = \left(-\frac{\delta_{j+1}-\delta_j}{h_{j+1}} \sum_{i=j+1}^{N} P_i\right) + \frac{\delta_j - \delta_{j-1}}{h_j} \sum_{i=j}^{N} P_i = P_j \times \Delta_{max} \tag{4.6}$$

Due to the force varying over the height (as the floor weights vary), the force distribution is slightly more complicated, though determining the weight of the floor is a trivial exercise. The main realization; however, is the total base shear would still be equivalent to those presented in Table 4.2.

4.4 Evaluation Using Varied Deformed Configuration

The previous studies focused on using the maximum drift over the full height of the building; however, this displaced shape consistently over the full height of a tower is a conservative assumption (as damage tends to localize in taller braced frame structures). As an alternative, we use two variations on the deformed configuration. The structural deformation is broken into two categories representative of a shear mode and a flexural mode (See Figure 4.12).

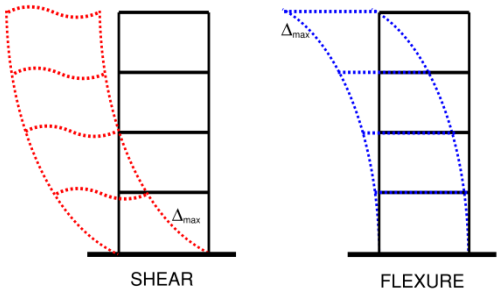

Figure 4.12 Flexural vs Shear Deformation

In either of these deformed shapes, the cancelation of forces is more complex since the floor below has a different slope than the floor above. This change in slope does not allow for the clean cancelation of the horizontal floor shears as was observed earlier. This makes the floor force equal to

$$H_j = \left(-\frac{\delta_{j+1}-\delta_j}{h_{j+1}}\sum_{i=j+1}^{N} P_i\right) + \frac{\delta_j-\delta_{j-1}}{h_j}\sum_{i=j}^{N} P_i \tag{4.7}$$

Next, this equation is summed over the height to determine floor shears for any deformed shape, and then specialized to the two shapes suggested in Figure 4.12. To determine the base shear specifically, Equation 4.7 is summed over the entire height of the structure.

$$V_b = \sum_{j=1}^{N}\left(-\frac{\delta_{j+1}-\delta_j}{h_{j+1}}\sum_{i=j+1}^{N} P_i + \frac{\delta_j-\delta_{j-1}}{h_j}\sum_{i=j}^{N} P_i\right) \tag{4.8}$$

For the shear beam deformed shape, we implement the 3 various maximum drifts and create the displacement field described by Eq. 4.9 (quarter sine wave displacement field).

$$u_{shear} = \Delta_{max}\frac{2elev_N}{\pi}\times\sin\left(\frac{elev_j}{elev_N}\frac{\pi}{2}\right) \tag{4.9}$$

Similarly, for the flexural displacement, an assumed deformed shape of a beam with uniform stiffness and peak drift at the roof under triangular loading gives the deflection profile shown in Eq 4.10. Note, the inelastic displacement field represented for flexure may not be very realistic for a nonlinear structure, but is used as a computational demonstration of the effects of deformation on response.

$$u_{flex} = \frac{24\Delta_{max}}{15{elev_N}^3} \times \left(\frac{{elev_j}^5}{120 elev_N} + \frac{elev_N \times {elev_j}^3}{12} + \frac{{elev_N}^2 \times {elev_j}^2}{6} \right) \tag{4.10}$$

Given these displacements, and taking derivatives of Eq. 4.9 and Eq. 4.10, the slope/drift in the columns is determined. This is substituted into Eq. 4.7 to determine the variation in horizontal forces. The shear deformed shape drifts and horizontal forces described by Eq. 4.11 and Eq. 4.12.

$$\theta_{shear\ j} = \Delta_{max} \cos\left(\frac{elev_j}{elev_N} \frac{\pi}{2} \right) \tag{4.11}$$

$$H_j = \left(-\theta_{shear\ j+1} \sum_{i=j+1}^{N} P_i \right) + \theta_{shear\ j} \sum_{i=j}^{N} P_i \tag{4.12}$$

Similarly, for the flexural case, Eq. 4.13 and Eq. 4.14 respectively show the drift and horizontal forces associated with the prescribed deformed shape.

$$\theta_{flex\ j} = \frac{24\Delta_{max}}{15{elev_N}^3} \times \left(\frac{{elev_j}^4}{24 elev_N} + \frac{elev_N \times {elev_j}^2}{4} + \frac{{elev_N}^2 \times elev_j}{3} \right) \tag{4.13}$$

$$H_j = \left(-\theta_{flex\ j+1} \sum_{i=j+1}^{N} P_i \right) + \theta_{flex\ j} \sum_{i=j}^{N} P_i \tag{4.14}$$

The previous described equations can be used to determine the moments and shears in any system directly using basic statics.

4.5 Computational Evaluation

The particular building described in Table 4.3 is now examined under the series of displacement fields suggested earlier at the code limits of drift for various occupancy categories. The structure is simplified such that the floors are of equivalent height and weight.

Figure 4.13 shows the suite of displacements prescribed earlier and the field of potential inelastic deformations examined from here forward. It is clear that the constant inelastic drift ratio data set produces the largest displacement at every individual story. Of particular interest is that the displacement of the shear deformation is consistently larger than that of the flexural assumption used. This implies consistently larger P-Delta moments in the shear assumption when compared to the flexural.

Building Information			
Story	Floor Height	Elev	Floor Weight
	m	m	kN
20	3.96	79.2	4.4482
19	3.96	75.3	4.4482
18	3.96	71.3	4.4482
17	3.96	67.4	4.4482
16	3.96	63.4	4.4482
15	3.96	59.4	4.4482
14	3.96	55.5	4.4482
13	3.96	51.5	4.4482
12	3.96	47.5	4.4482
11	3.96	43.6	4.4482
10	3.96	39.6	4.4482
9	3.96	35.7	4.4482
8	3.96	31.7	4.4482
7	3.96	27.7	4.4482
6	3.96	23.8	4.4482
5	3.96	19.8	4.4482
4	3.96	15.8	4.4482
3	3.96	11.9	4.4482
2	3.96	7.9	4.4482
1	3.96	4.0	4.4482
0	0.00	0.0	4.4482

Table 4.3 Basic Building Information

While examining the displacement fields is of interest, it is actually the variations of drift and weight above particular floors in a building that create "kick forces" in a structure. Since these prescribed deformed shapes arise from the accumulation of drifts in the system, it is important to understand what the deformed shapes described in Figure 4.13 imply for drifts. Taking the difference of displacement between floors and dividing by the height of the structural floor gives the drift field shown in Figure 4.14 (Note, these computations do not use the continuous equation described earlier, and instead use the discrete drifts associated with the continuous displacement fields prescribed). Observe that the prescribed drift levels match the peak demands imposed by the code at the base for the assumed shear deformation and at the roof for the assumed flexural deformation. This is consistent with the developed algorithm's intent in both cases. As the displacement magnitudes are greatly different (variation in roof displacements of approximately 1.5x), there will be a differential in the magnitude of moments and shear associated with these inelastic configurations.

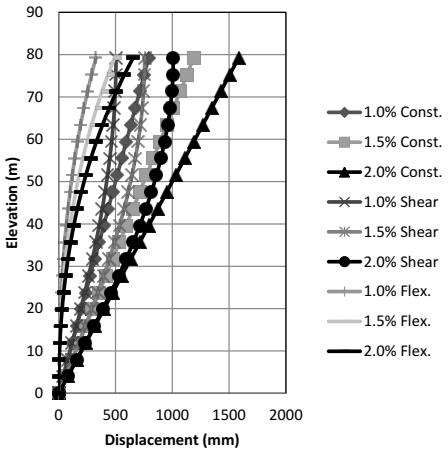

Figure 4.13 Displacement Fields of Code Based and Proposed Displacement Fields

We studied the applied horizontal forces on the system resulting from the kick forces associated with the sloped columns and vertical loads applied to the building. A summary of the horizontal loads imposed on the system, and the accumulation of shear over the height is seen in Figure 4.15 and Figure 4.16 respectively.

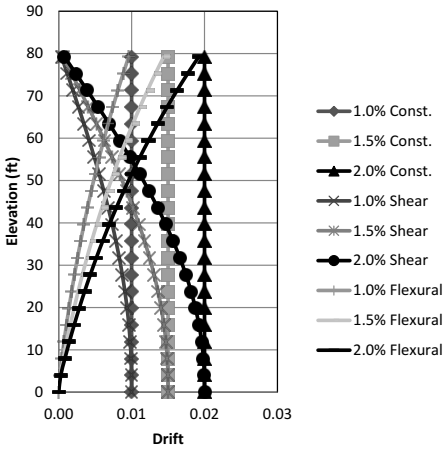

Figure 4.14 Drift Associated with each Displacement Field

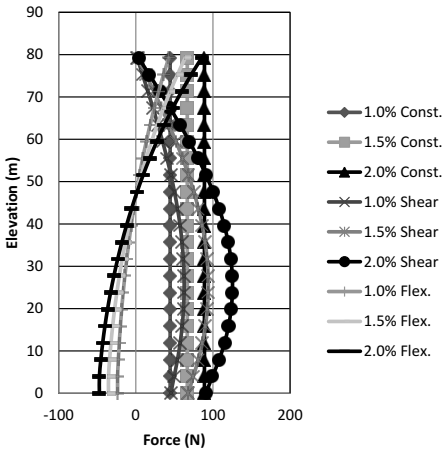

Figure 4.15 Applied Floor Loads for each Deformed Shape Prescribed

Several key observations were made from the data. Since the drift field for the shear deformed shape matches at the base condition for the constant inelastic drift, the base shears are consequently equal to one another (See Figure 4.16). The distribution of shear over the height; however, is always less for the shear assumption as opposed to the constant inelastic drift, even though the floor force may be larger on a floor-by-floor basis (See Figure 4.15). This will clearly lead to a lower moment magnitude over the height of the structure as opposed to the uniform load distribution of constant inelastic drift.

The flexural drift assumption creates a near zero base shear condition due to the verticality of the base column assumed in this displacement field. This result clarifies why there are forces oriented in two directions in the flexural displacement field shown in Figure 4.15 as these forces must cancel over the height of the structure since the vertical load cannot create any net shear. The need for omnidirectional horizontal forces over the height of the structure arises when a vertical condition is enforced at the base combined with the presence of any applied gravity load forces to the system. This may seem counterintuitive relative to the deformed shape given the continuous curvature without inflection.

Finally, the moment in the system due to the varied deformed configurations is observed (See Figure 4.17). Drastic variation in the moment diagram shape as well as the magnitude over the structure's height is evident from these results. This again shows the influence of what the assumed actual deformed configuration is and the demand on the system in its post event plastically deformed configuration.

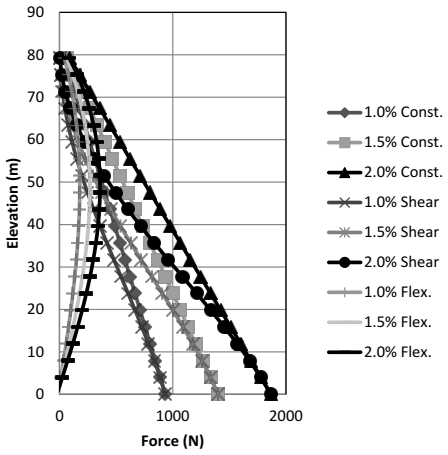

Figure 4.16 Accumulated Shear Force in Building over the Height

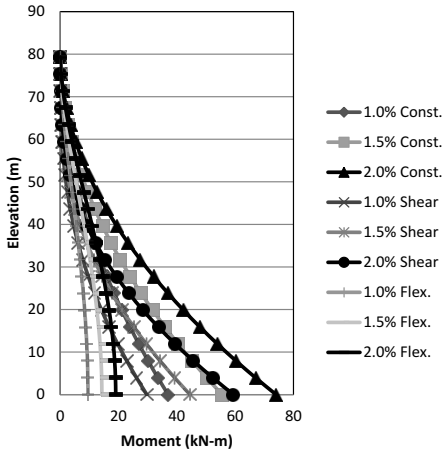

Figure 4.17 Accumulated Moment in Building over the Height

4.6 Potential Recommendations

To better capture the design intent of post event stability, the following method suggests an iterative process to establish an alternative set of design forces for a secondary moment frame:

When implementing a dual system with a secondary intermediate moment frame, use the appropriate design forces prescribed by the design provisions for the actual applied earthquake, which take into account the interplay of forces between the moment frame and braced frame systems. This typically results in a system where a majority of the building's base shear is resolved in the braced frame, and the moment frame may take on the order of 10% to 15% of the actual seismic demand.

From here, determine the elastic displacements in the system and amplify them by the appropriate ductility factor (C_d) to achieve the inelastic displacements of the proposed system. Determine the horizontal design forces due to the associated inelastic drifts and gravity loads on a floor-by-floor basis (Eq. 4.7). Apply these forces to the moment frame only and determine if the subsequent structure maintains stability in this configuration (can support the loads applied). If not, increase the strength of the moment frame and repeat.

Note that this analysis would also be linear, as the forces and assumed final configuration of the structure already take into account the P-Delta stability of the structure negating the need to perform another geometrically nonlinear analysis. It could be argued that the stiffness of the structure differs in the newly deformed shape; however, at the levels of maximum drift implemented in the seismic provisions today, the effect is minimal (Powell, 2010).

If 25% of total base shear forces is maintained as the minimum magnitude of force for design of secondary frames, some level of consideration in the way the forces are distributed consistent with the deformed shape is appropriate. This does have certain issues in determining magnitude as certain configurations could result in no base shear (See Figure 4.16). Perhaps the simplest approach is to use a uniform applied load based on the maximum inelastic drift on all levels. This is varied from the seismic forces distribution currently implemented over the height of the building that shifts these forces to be higher as the floors are further from the point of excitation/base.

4.7 Conclusions

The secondary moment frame provisions, with respect to seismic design category (SDC), aim to make braced frame structures more ductile while maintaining stability in a post event state. Through the examination of the prior results, significant differences in the demand on a building system based on the deformed configuration after an event has occurred with respect to maintaining verticality and sustaining stability were observed. Most importantly, this demand is completely based on the gravity induced forces and the inelastic deformed shape of the structure after an event. The use of 25% of the earthquake force as a design metric for a stabilizing frame under the assumption that the bracing components are no longer reliable does not appear to have a firm physical basis for enforcing this intent.

Another important element to address is the idea that, regardless of the deformed shape assumed, the demand on the frame was significantly less for occupancy categories where the more stringent drift criteria were applied. Clearly the P-Delta forces on the secondary moment frames in Occupancy Category IV are less in magnitude than in other occupancy categories, indicating an opportunity for either economy in these types of structures, or potentially a relative increase in the lower occupancy categories

depending on the frame of reference. From either perspective, the use of 25% of the base shear across the occupancy categories does not logically account for the variation in maximum drift designed for.

For results shown and discussed, see Appendix D.

4.8 Future Research

One element that was not investigated here, but is of great importance, is the state of stress in the system after the event has occurred. As the moment frame and braced frames will all work in tandem, any form of non-linearity in the system has the potential to develop permanent residual stresses. This could reduce the capacity of elements in the post event state. The intent of this paper is to bring to light the idea of using this basic deformation based design technique to enlighten design strategies for secondary moment frames. The aim is to encourage a more consistent method with respect to the code's intents for the frame as a whole.

The concept of the secondary frame being implemented at 240ft in SDC-D or worse is also somewhat vague, yet the design strategy presented is independent of this code requirement and could be extrapolated to multistory buildings of any height (shorter or taller). The idea that as a structure gets taller, there is more of a P-Delta effect on the system overall is sound. Perhaps a more refined approach assessing how much P-Delta moment is in the system in the final deformed configuration for any structure would be more suited for determining if secondary moment frames are indeed required. This would require that the residual capacity of the braced frame itself could sustain said loading and a better understanding of element stiffness after repeated hysteresis.

4.9 References

International Code Council, Inc. *International Building Code.* County Club Hills : IBC, 2012.

American Society of Civil Engineers. *ASCE 7 - Minimum Design Loads for Buildings and Other Structures.* Reston, Virginia : American Society of Civil Engineers, 2010.

BSSC. *NEHRP Recommended Seismic Provisions for New Buildings and Other Structures.* Washington DC : FEMA, 2009. P-750.

Hall, John. *Seismic Response of Steel Frame Buildings to Near-Source Ground Motions.* Pasadena : Earthquake Engineering Research Laboratory, 1997. EERL 97-05.

Sabelli, Rafael, Roeder, Charles W. and Hajjar, Jerome F. *Seismic Design of Steel Special Concetrically Braced Frame Systems.* Gaitherburg : National Institute of Standards and Technology, 2013. NIST GCR 13-917-24.

Hamburger, Ronald, et al., et al. *Seismic Design of Steel Special Moment Frame Systems.* Gaiitherburg : National Institute of Standards and Technology, 2009. NIST GCR 09-917-3.

Powell, Graham. *Modeling for Structural Analysis, Behavior and Basics.* Berkeley : Computers and Structures Inc., 2010.

Chopra, A. K. *Dynamics of Structures: Theory and Application to Earthquake Engineering.* Upper Saddle River, NJ : Prentice Hall, 2007.

Smith, Bryan and Coull, Alex. *Tall Building Structures, Analysis and Design.* Toronto : John Wiley & Sons, 1991.

Whittaker, Andrew S, Uang, Chia-Ming and Bertero, Vitelmo V. *An Experimental Study of the Behavior of Dual Steel Systems.* University of California at Berkeley : Earthquake Engineering Research Center, 1990.

Roeder, Charles W. *Seismic Behavior of Concetrically Braced Frame.* s.l. : Journal of Structural Engineering, 1989. Vol. 115.

Michel Bruneau, Chia-Ming Uang, Andrew Whittaker. *Ductile Design of Steel Structures.* New York : McGraw-Hill, 1998.

Appendix A

Static Condensation

Given a computational model with multiple degrees of freedom, it is numerically possible to reduce the set of equations to only the degrees of freedom where forces are to be applied to the system. In the case of earthquake analysis for building type structures, this is typically limited to the massed degrees of freedom at a floor level. In these conditions, the equations of motion can be reduced to only include these condensed degrees of freedom, and still maintain accuracy in the solution. This method is well described in Chopra's Earthquake Engineering text (REFERENCE CORRECTLY) and is put forth here for convenience.

An undamped dynamic system under forced vibration can be described by the simple equation:

$$\boldsymbol{M}\ddot{u} + \boldsymbol{K}u = p(t) \tag{A.1}$$

These equations can be organized and ordered such that there are degrees of freedom with mass or dynamic degrees of freedom (denoted "t") and massless degrees of freedom (denoted "0").

$$\begin{bmatrix} \boldsymbol{m_{tt}} & \boldsymbol{0} \\ \boldsymbol{0} & \boldsymbol{0} \end{bmatrix} \begin{Bmatrix} \ddot{u}_t \\ \ddot{u}_0 \end{Bmatrix} + \begin{bmatrix} \boldsymbol{k_{tt}} & \boldsymbol{k_{t0}} \\ \boldsymbol{k_{0t}} & \boldsymbol{k_{00}} \end{bmatrix} \begin{Bmatrix} u_t \\ u_0 \end{Bmatrix} = \begin{Bmatrix} p_t(t) \\ 0 \end{Bmatrix} \tag{A.2}$$

Multiplying out the above, we get two separate systems of equations, one with a forcing function and one without, but both sets of equations require solving for dynamic degrees of freedom and massless degrees of freedom.

$$\boldsymbol{m_{tt}}\ddot{u}_t + \boldsymbol{k_{tt}}u_t + \boldsymbol{k_{t0}}u_0 = p_t(t) \qquad\qquad \boldsymbol{k_{0t}}u_t + \boldsymbol{k_{00}}u_0 = 0 \tag{A.3}$$

Solving for the massless degrees of freedom from the second half of A.3, we get a computational relationship which allows for u_0, the massless degrees of freedom, to be replaced by a function of the dynamic degrees of freedom.

$$u_0 = -\boldsymbol{k_{00}}^{-1}\boldsymbol{k_{0t}}u_t \tag{A.4}$$

Substituting this back into the first half of A.3 gives

$$\boldsymbol{m_{tt}}\ddot{u}_t + \boldsymbol{k_{tt}}u_t + -\boldsymbol{k_{t0}}\boldsymbol{k_{00}}^{-1}\boldsymbol{k_{0t}}u_t = \boldsymbol{m_{tt}}\ddot{u}_t + [\boldsymbol{k_{tt}} - \boldsymbol{k_{t0}}\boldsymbol{k_{00}}^{-1}\boldsymbol{k_{0t}}]u_t = p_t(t) \tag{A.5}$$

The bracketed term in A.5 is the condensed stiffness matrix which allows for the problem to be solved entirely based on the displacements of the dynamic degrees of freedom. The solution to this displacement field can then be used to back out any condensed response by plugging back into A.4

A p p e n d i x B

Schematic drawings of 6 story building used in Chapter 2 study on the implementation of viscous capped damping in braced frame building structures.

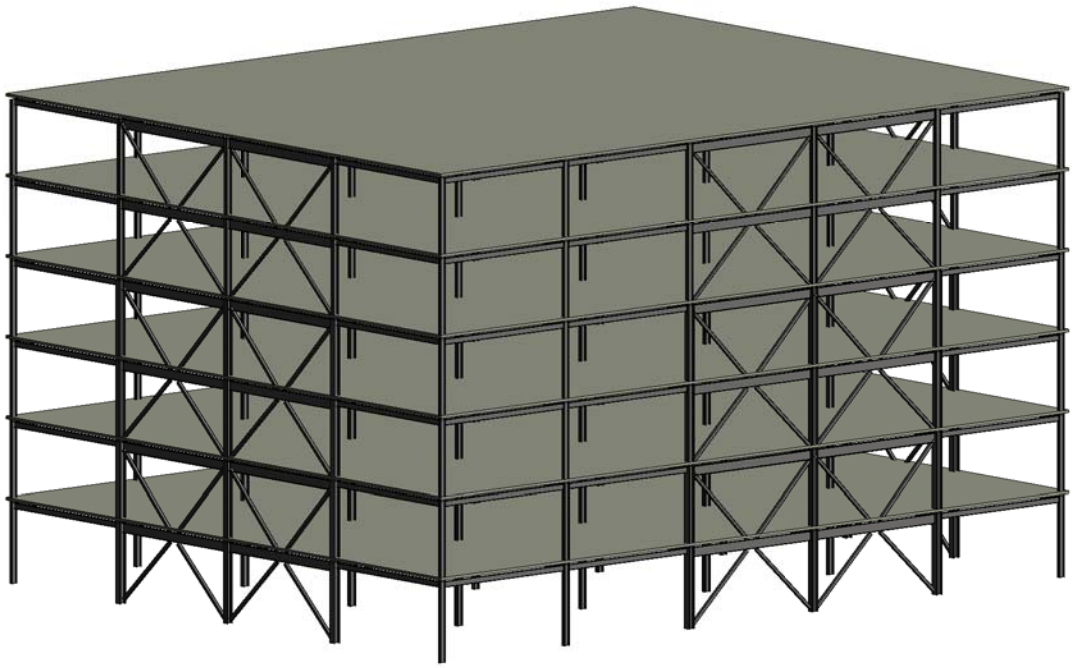

Caltech

http://www.mce.caltech.edu/

CALTECH

6 STORY

3D View

Project number	Project Number
Date	3/25/2014
Drawn by	Anthony Massari
Checked by	Anthony Massari

S.1.0

Scale

10/29/2015 6:44:22 PM

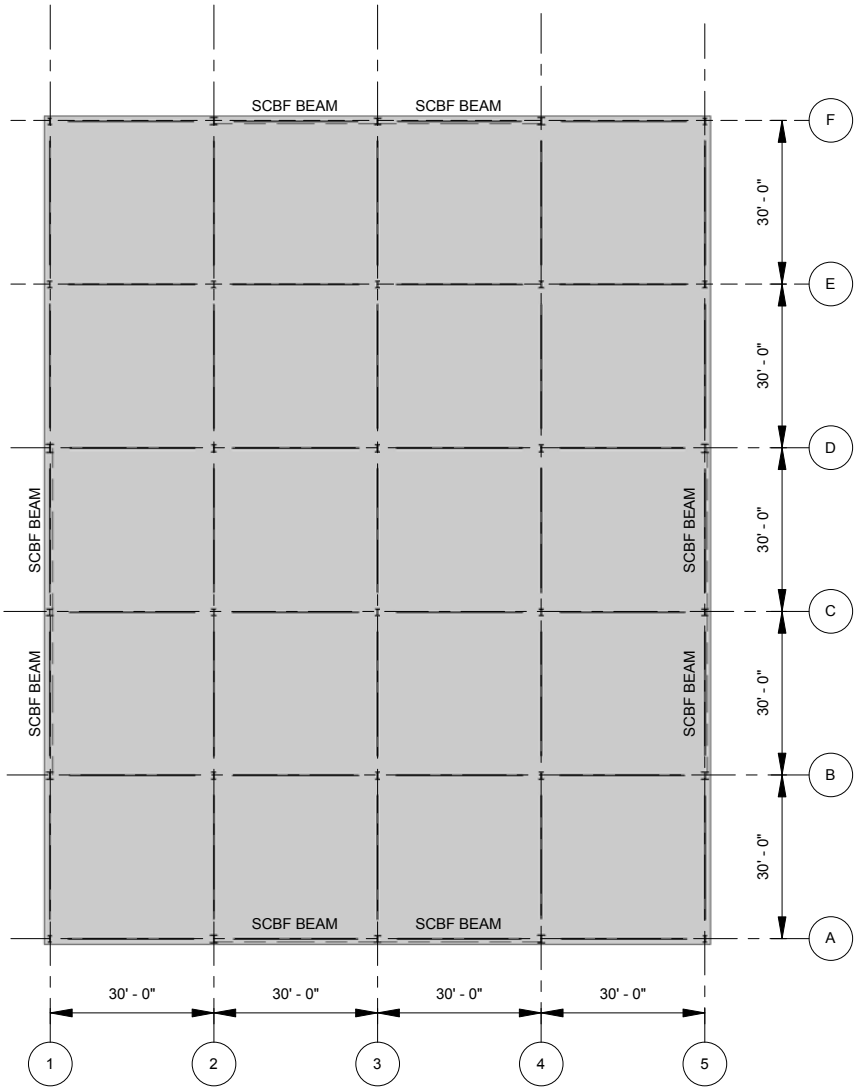

SCBF BEAM SCHEDULE	
ROOF	W21x55
LEVEL 6	W21x44
LEVEL 5	W21x68
LEVEL 4	W21x44
LEVEL 3	W21x83
LEVEL 2	W21x44

Caltech

http://www.mce.caltech.edu/

CALTECH

6 STORY

TYP. FLOOR PLAN

Project number	Project Number
Date	3/25/2014
Drawn by	Anthony Massari
Checked by	Anthony Massari

S.1.1

Scale As indicated

10/29/2015 6:44:23 PM

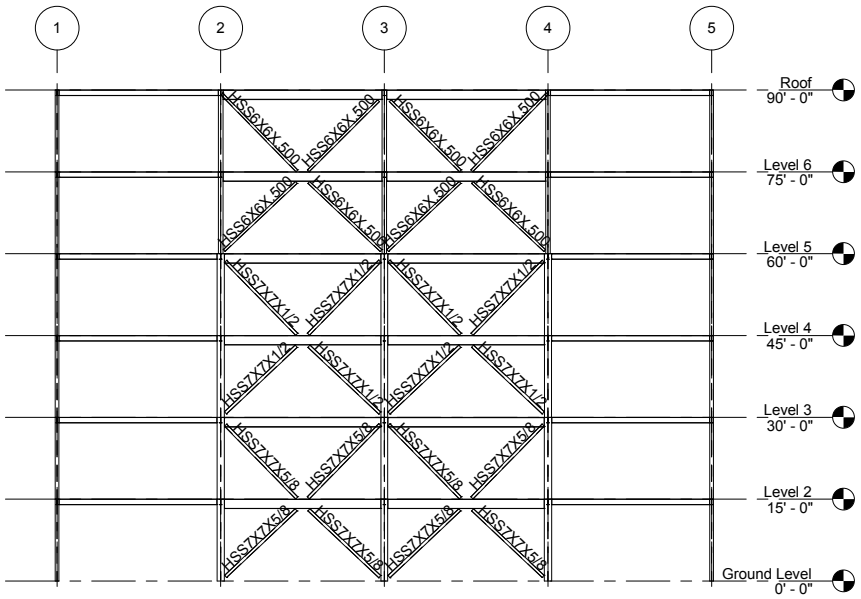

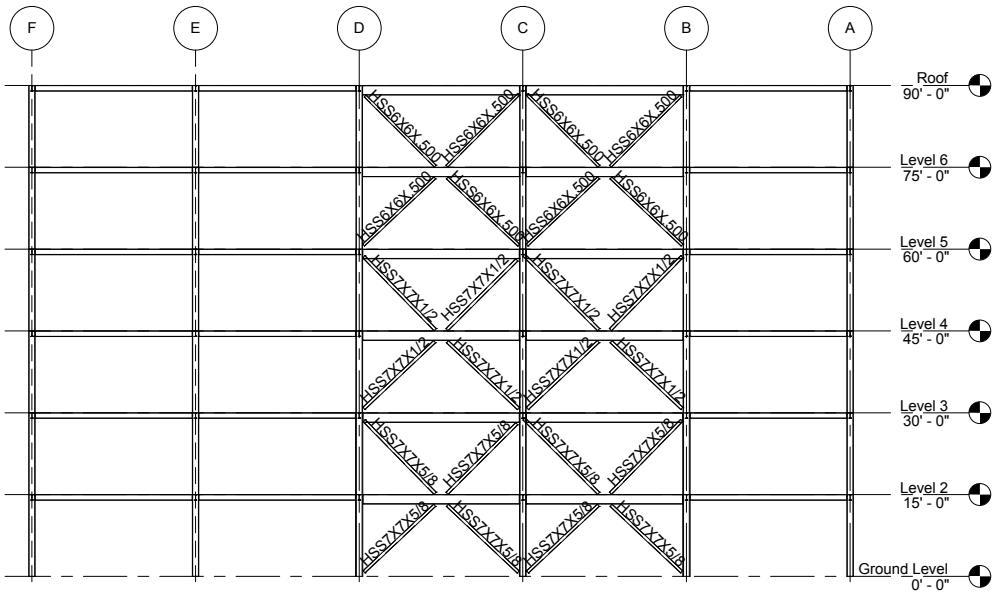

Caltech http://www.mce.caltech.edu/	CALTECH 6 STORY	TYP. BRACING ELEV.
	Project number: Project Number Date: 3/25/2014 Drawn by: Author Checked by: Checker	S.2.1 Scale: 1/32" = 1'-0"

10/29/2015 6:44:23 PM

Roof						Roof
90' - 0" Level 6	W14X48	W14X74	W14X68	W14X48	W14X48	90' - 0" Level 6
75' - 0" Level 5	W14X48	W14X74	W14X68	W14X48	W14X48	75' - 0" Level 5
60' - 0" Level 4	W14X48	W14X145	W14X132	W14X61	W14X48	60' - 0" Level 4
45' - 0" Level 3	W14X48	W14X145	W14X132	W14X61	W14X48	45' - 0" Level 3
30' - 0" Level 2	W14X48	W14X233	W14X132	W14X82	W14X61	30' - 0" Level 2
15' - 0" Ground Level	W14X48	W14X233	W14X132	W14X82	W14X61	15' - 0" Ground Level
0' - 0"						0' - 0"
Column Locations	A-1, A-5, F-1, F-5	A-2, A-4, B-1, B-5, D-1, D-5, F-2, F-4	A-3, C-1, C-5, F-3	B-2, B-3, B-4, C-2, C-3, C-4, D-2, D-3, D-4, E-2, E-3, E-4	E-1, E-5	

Caltech

http://www.mce.caltech.edu/

CALTECH

6 STORY

COLUMN SCHEDULE

Project number	Project Number
Date	3/25/2014
Drawn by	Author
Checked by	Checker

S.3.1

Scale 1/16" = 1'-0"

10/29/2015 6:44:24 PM

Appendix C

Schematic drawings of 20 story building used in Chapter 4 study on modified procedures for the design of secondary intermediate moment frames for building structures.

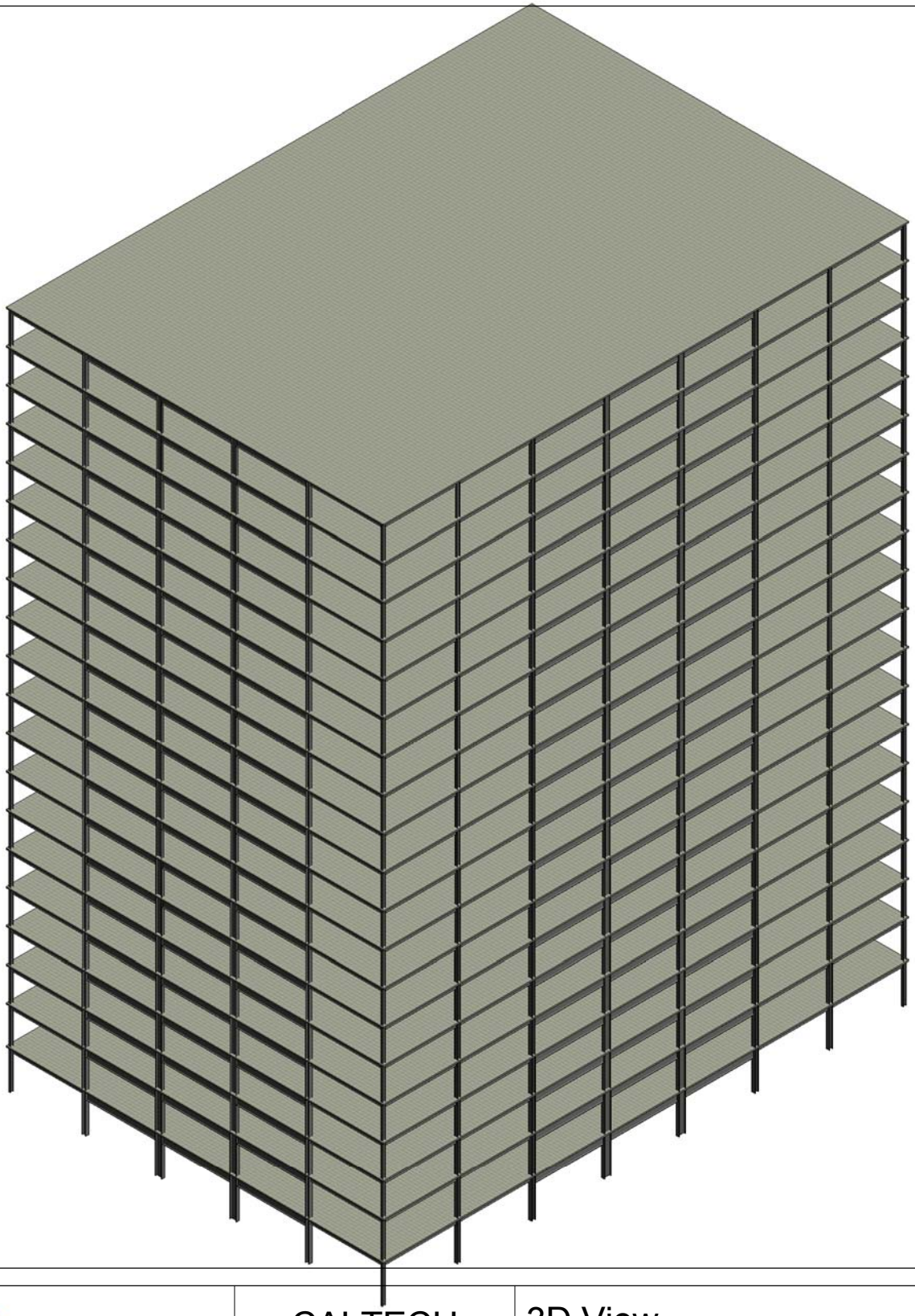

Caltech

http://www.mce.caltech.edu/

CALTECH

20 STORY

3D View

Project number	Project Number	S.1.0
Date	3/25/2014	
Drawn by	Anthony Massari	
Checked by	Anthony Massari	Scale

9/29/2015 9:54:05 AM

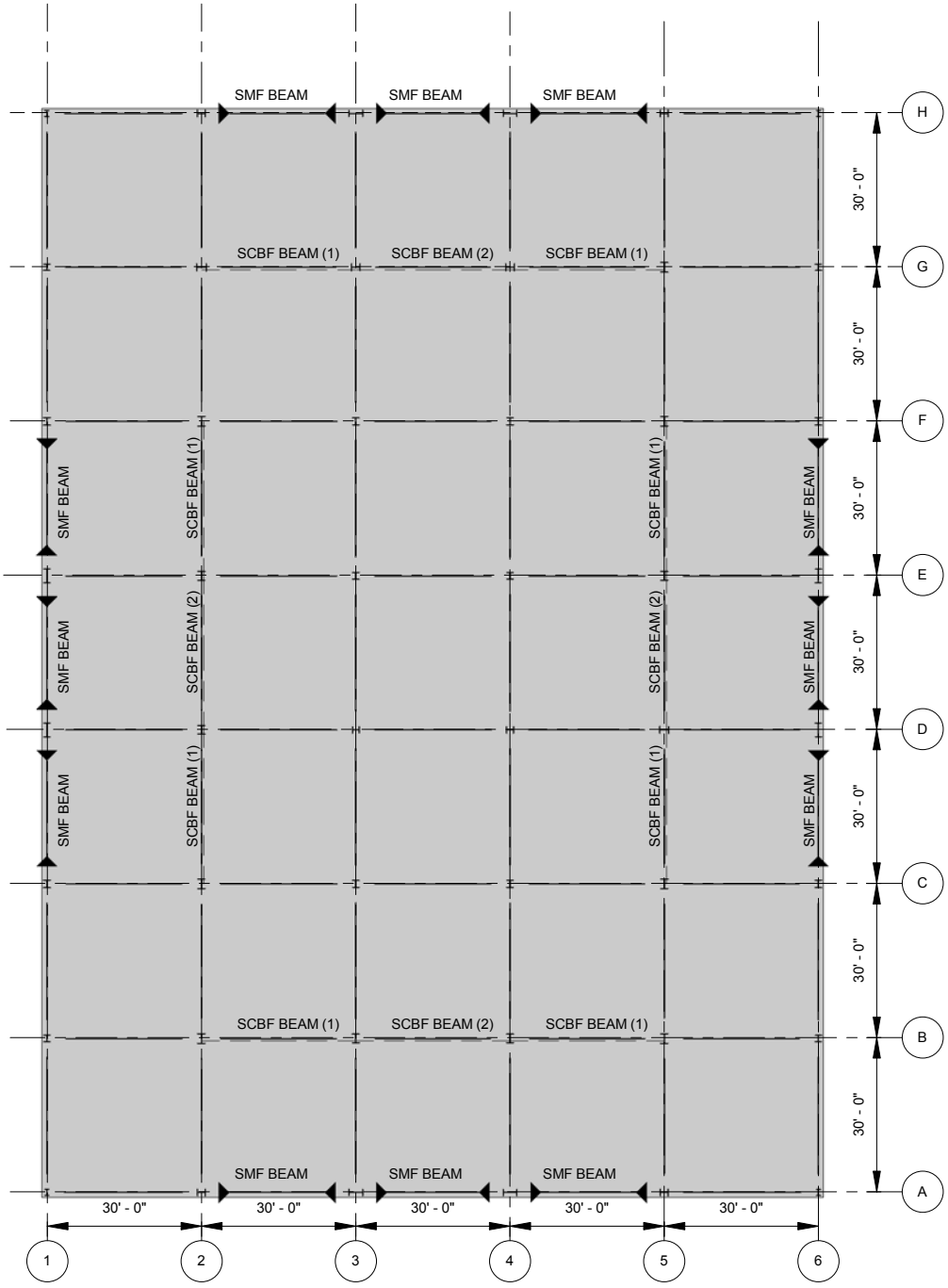

SCBF BEAM SCHEDULE		
	BEAM (1)	BEAM (2)
ROOF	-	W21x83
LEVEL 20	-	W21x44
LEVEL 19	-	W21x101
LEVEL 18	-	W21x44
LEVEL 17	-	W21x101
LEVEL 16	-	W21x44
LEVEL 15	-	W21x101
LEVEL 14	-	W21x44
LEVEL 13	W21x101	W21x101
LEVEL 12	W21x44	W21x44
LEVEL 11	W21x101	W21x101
LEVEL 10	W21x44	W21x44
LEVEL 9	W21x101	W21x101
LEVEL 8	W21x44	W21x44
LEVEL 7	W21x101	W21x101
LEVEL 6	W21x44	W21x44
LEVEL 5	W21x101	W21x101
LEVEL 4	W21x44	W21x44
LEVEL 3	W21x101	W21x101
LEVEL 2	W21x44	W21x44

SMF BEAM SCHEDULE	
	BEAM
ROOF	W24x76
LEVEL 20	W24x76
LEVEL 19	W24x76
LEVEL 18	W24x76
LEVEL 17	W24x84
LEVEL 16	W24x84
LEVEL 15	W24x84
LEVEL 14	W24x84
LEVEL 13	W27x94
LEVEL 12	W27x94
LEVEL 11	W27x94
LEVEL 10	W27x94
LEVEL 9	W27x94
LEVEL 8	W30x108
LEVEL 7	W30x108
LEVEL 6	W30x108
LEVEL 5	W30x108
LEVEL 4	W30x108
LEVEL 3	W30x132
LEVEL 2	W30x132

Caltech

http://www.mce.caltech.edu/

CALTECH

20 STORY

TYP. FLOOR PLAN

Project number	Project Number
Date	3/25/2014
Drawn by	Anthony Massari
Checked by	Anthony Massari

S.1.1

Scale As indicated

9/29/2015 9:54:05 AM

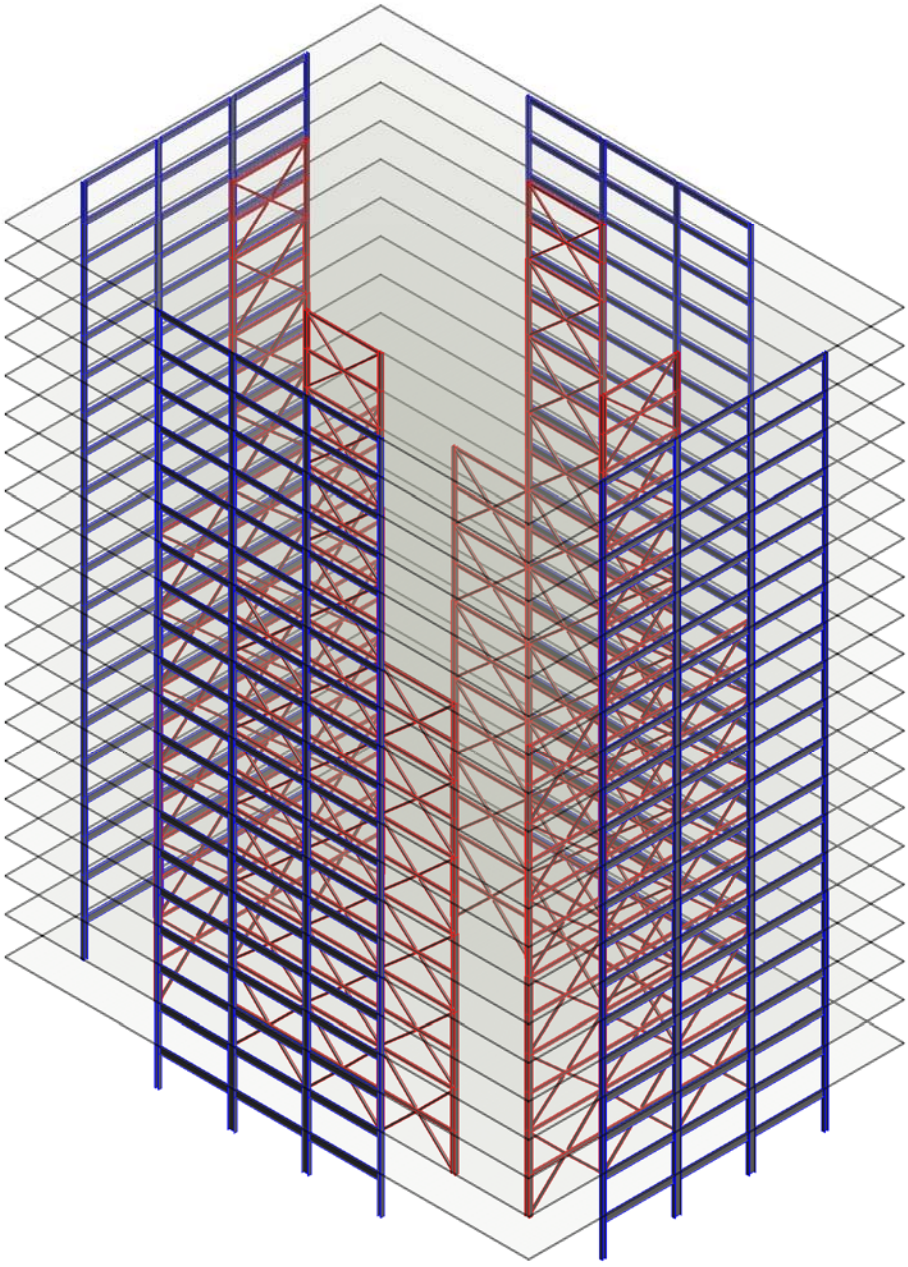

Caltech

http://www.mce.caltech.edu/

CALTECH

20 STORY

LATERAL SYSTEM 3D

Project number	Project Number
Date	3/25/2014
Drawn by	Author
Checked by	Checker

S.1.2

Scale

9/29/2015 9:54:07 AM

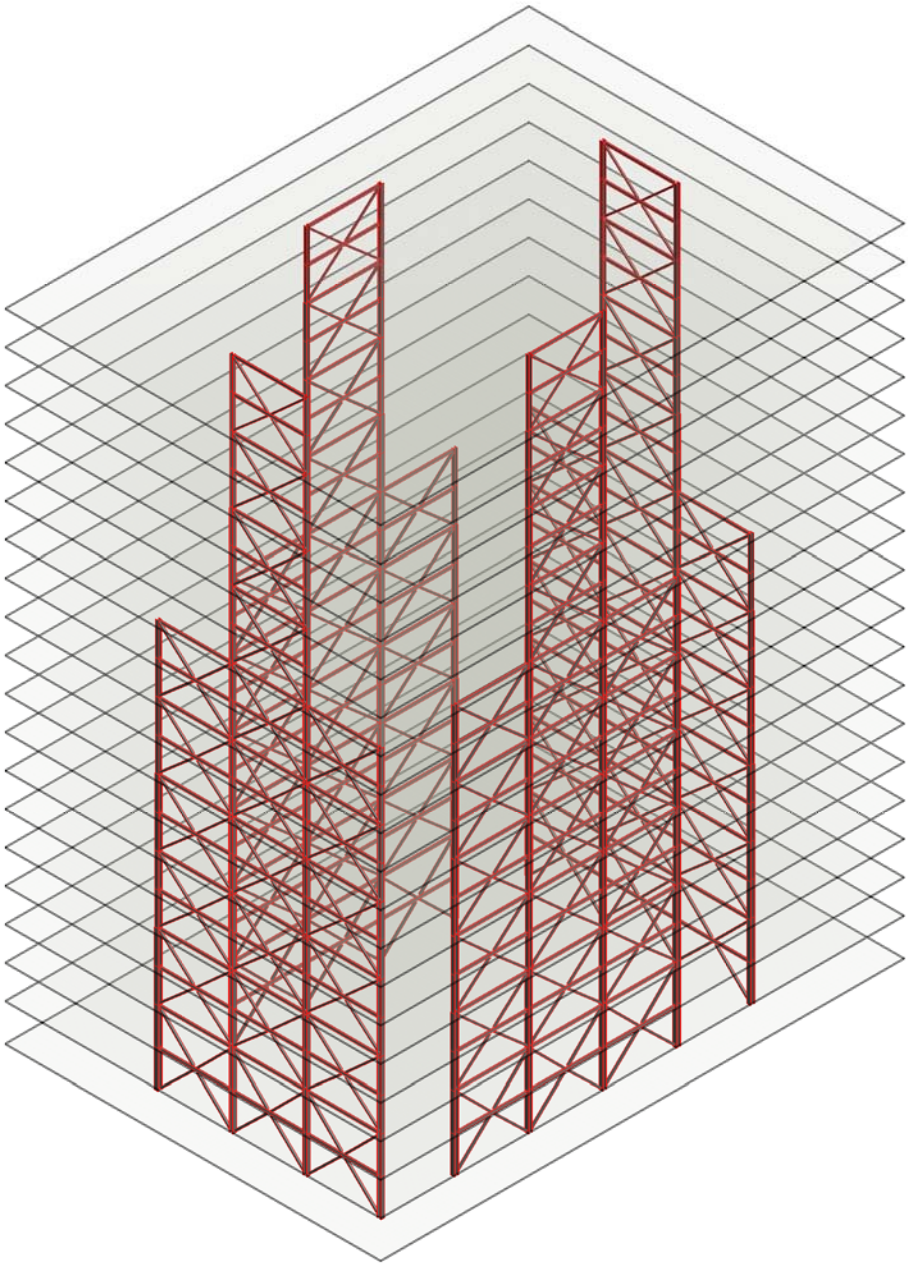

Caltech

http://www.mce.caltech.edu/

CALTECH

20 STORY

BRACED FRAME 3D

Project number	Project Number
Date	3/25/2014
Drawn by	Author
Checked by	Checker

S.2.1

Scale

9/29/2015 9:54:09 AM

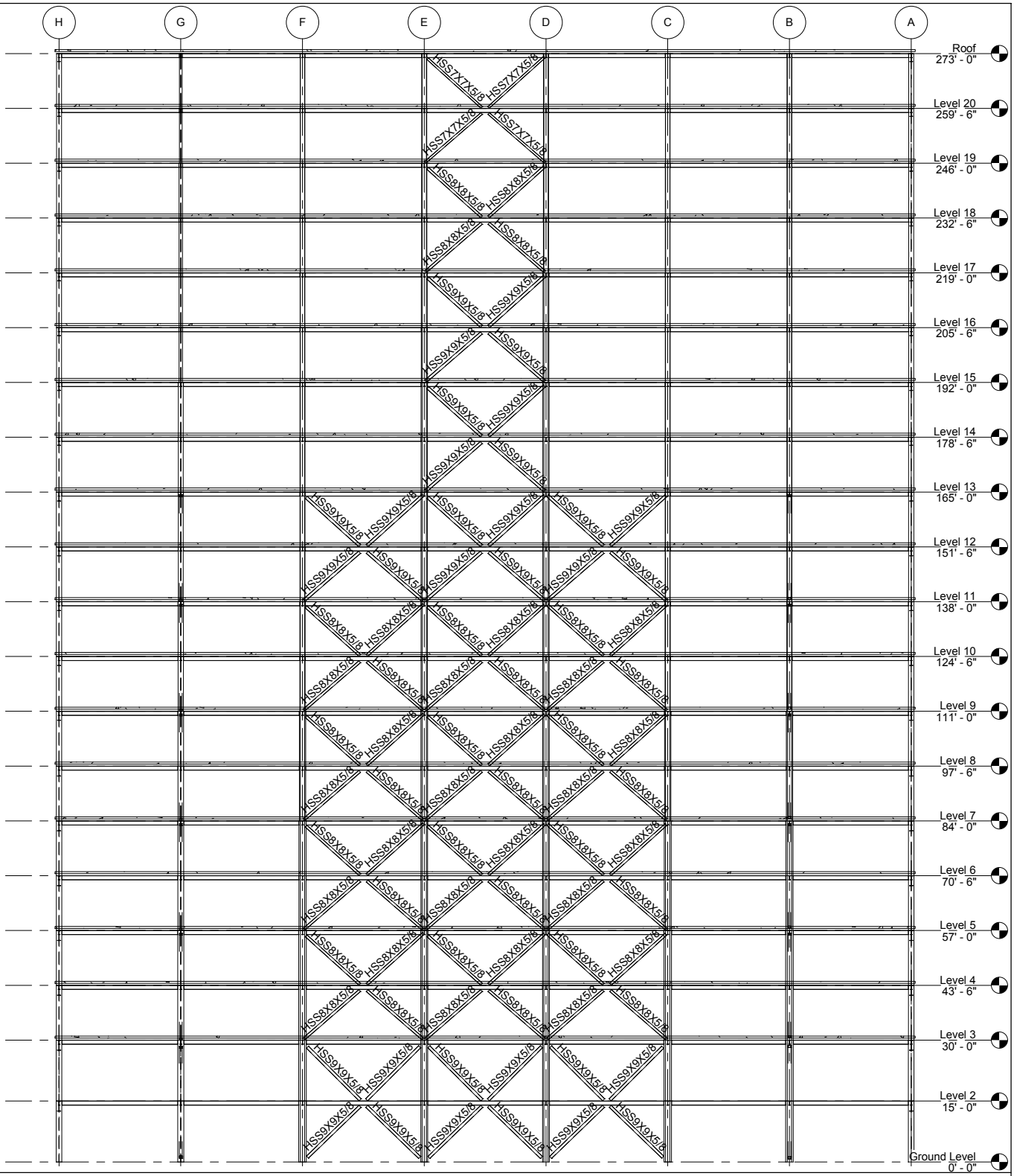

Caltech

http://www.mce.caltech.edu/

CALTECH

20 STORY

GRIDLINE 2 & 5 SBF

Project number	Project Number
Date	3/25/2014
Drawn by	Anthony Massari
Checked by	Anthony Massari

S.2.2

Scale 1/32" = 1'-0"

9/29/2015 9:54:11 AM

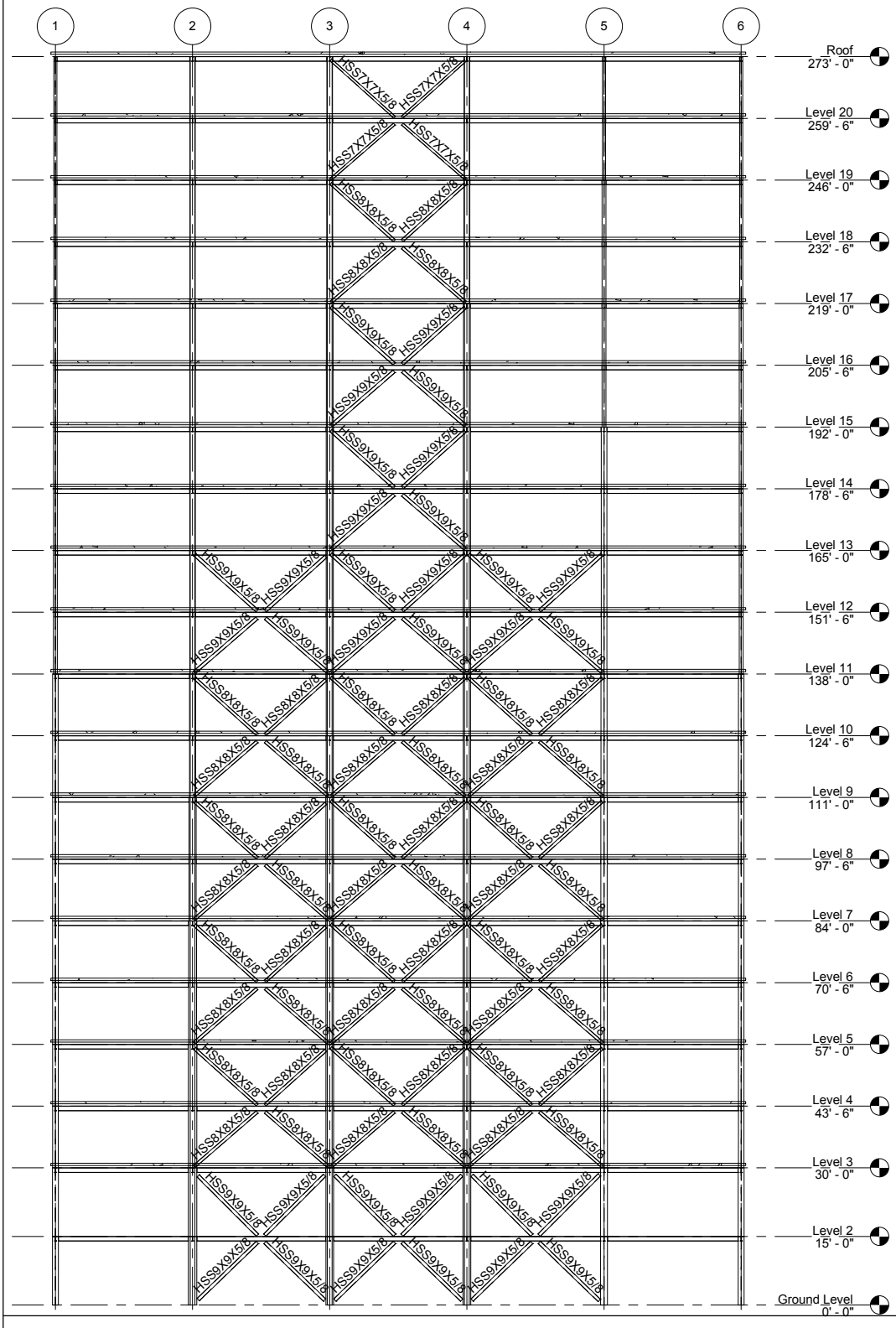

Caltech

http://www.mce.caltech.edu/

CALTECH

20 STORY

GRIDLINE B & G SBF

Project number	Project Number
Date	3/25/2014
Drawn by	Anthony Massari
Checked by	Anthony Massari

S.2.3

Scale 1/32" = 1'-0"

9/29/2015 9:54:13 AM

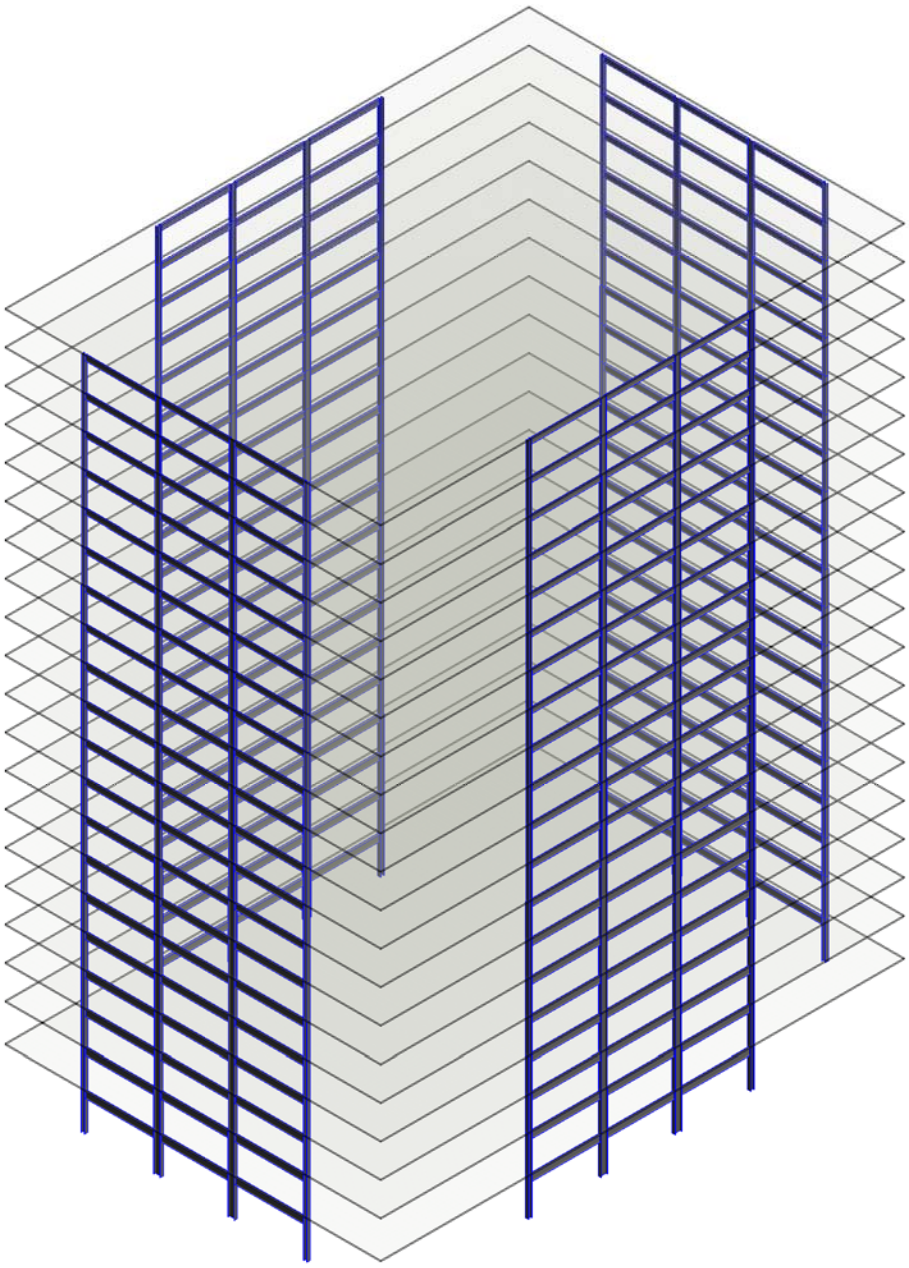

Caltech

http://www.mce.caltech.edu/

CALTECH

20 STORY

MOMENT FRAME 3D

Project number	Project Number
Date	3/25/2014
Drawn by	Author
Checked by	Checker

S.3.1

Scale

9/29/2015 9:54:15 AM

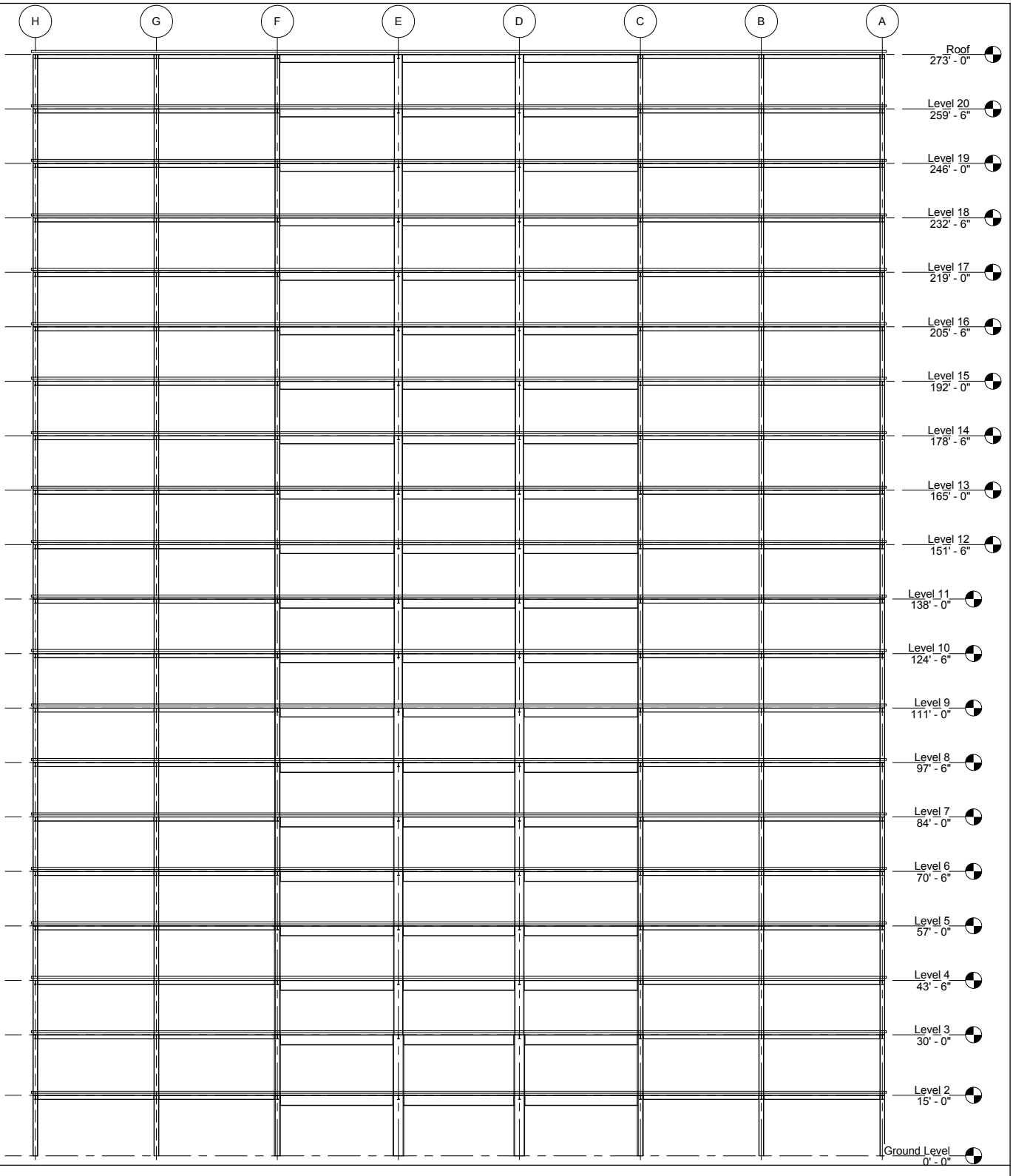

Caltech

http://www.mce.caltech.edu/

CALTECH

20 STORY

GRIDLINE 1 & 6 SMF

Project number	Project Number
Date	3/25/2014
Drawn by	Author
Checked by	Checker

S.3.2

Scale 1/32" = 1'-0"

9/29/2015 9:54:16 AM

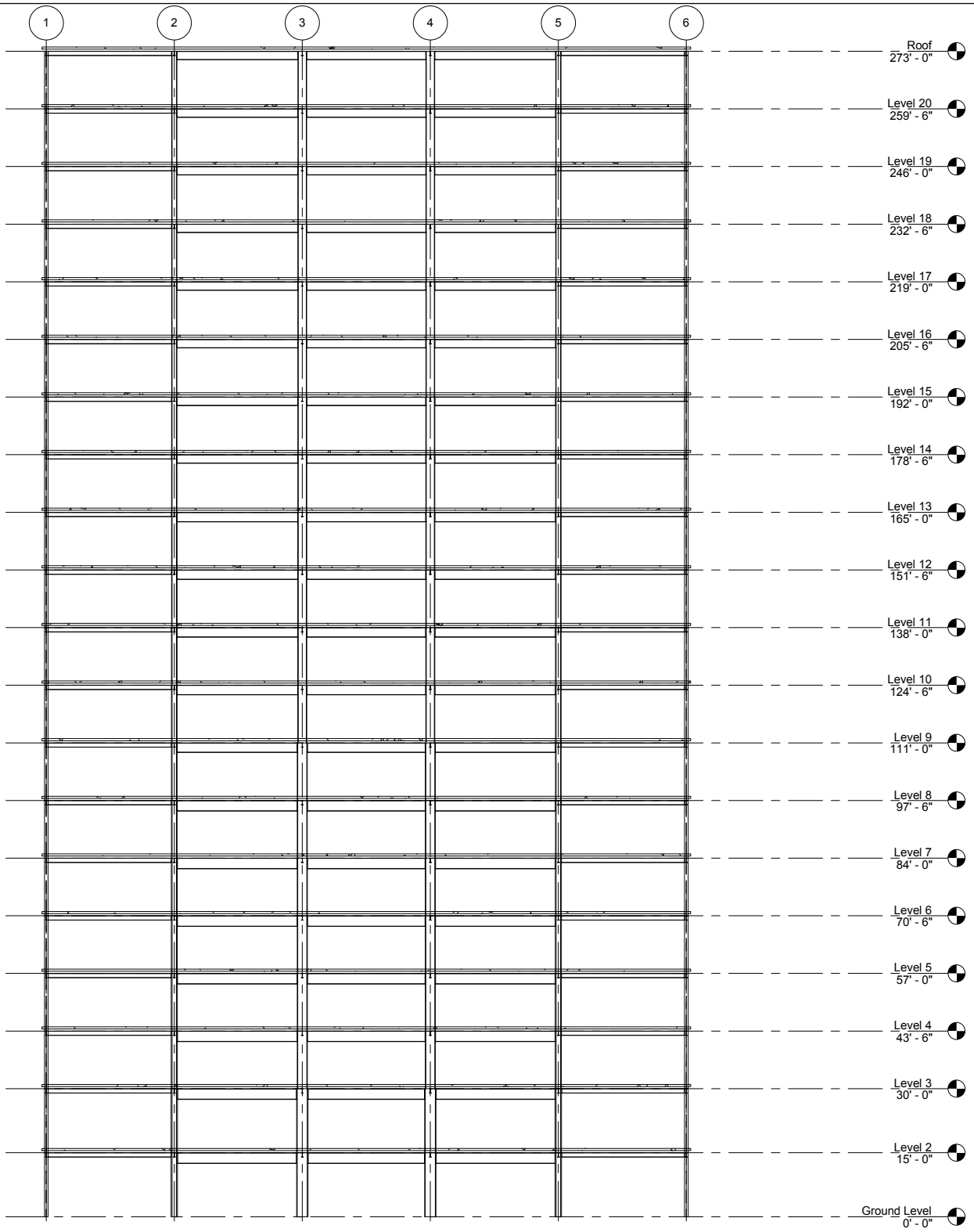

Caltech

http://www.mce.caltech.edu/

CALTECH

20 STORY

GRIDLINE A & H SMF

Project number	Project Number
Date	3/25/2014
Drawn by	Author
Checked by	Checker

S.3.3

Scale 1/32" = 1'-0"

9/29/2015 9:54:17 AM

Level 7								Level 7
84' - 0" Level 6	W14X61	W14X283	W27X217	W14X109	W14X605	W14X500	W14X193	84' - 0" Level 6
70' - 6" Level 5	W14X61	W14X283	W27X217	W14X109	W14X605	W14X500	W14X193	70' - 6" Level 5
57' - 0" Level 4	W14X61	W14X311	W27X217	W14X109	W14X730	W14X550	W14X211	57' - 0" Level 4
43' - 6" Level 3	W14X61	W14X311	W27X217	W14X109	W14X730	W14X550	W14X211	43' - 6" Level 3
30' - 0" Level 2	W14X68	W14X370	W30X292	W14X145	W14X730 w/ 1"PL	W14X550	W14X233	30' - 0" Level 2
15' - 0" Ground Level	W14X68	W14X370	W30X292	W14X145	W14X730 w/ 1"PL	W14X550	W14X233	15' - 0" Ground Level
0' - 0"								0' - 0"
Column Locations	A-1, A-6, H-1, H-6	A-2, A-5, C-1, C-6, F-1, F-6, H-2, H-5	A-3, A-4, D-1, D-6, E-1, E-6, H-3, H-4	B-1, B-6, G-1, G-6	B-2, B-5, C-2, C-5, F-2, F-5, G-2, G-5	B-3, B-4, D-2, D-5, E-2, E-5, G-3, G-4	C-3, C-4, D-3, D-4, E-3, E-4, F-3, F-4	

Caltech

http://www.mce.caltech.edu/

CALTECH

20 STORY

COLUMN SCHEDULE

Project number	Project Number
Date	3/25/2014
Drawn by	Anthony Massari
Checked by	Anthony Massari

S.4.1

Scale 1/16" = 1'-0"

9/29/2015 9:54:18 AM

Level 14								Level 14
178' - 6" Level 13	W14X61	W14X159	W24X162	W14X68	W14X132	W14X426	W14X90	178' - 6" Level 13
165' - 0" Level 12	W14X61	W14X193	W24X176	W14X82	W14X132	W14X426	W14X109	165' - 0" Level 12
151' - 6" Level 11	W14X61	W14X193	W24X176	W14X82	W14X132	W14X426	W14X109	151' - 6" Level 11
138' - 0" Level 10	W14X61	W14X211	W24X192	W14X90	W14X193	W14X426	W14X145	138' - 0" Level 10
124' - 6" Level 9	W14X61	W14X211	W24X192	W14X90	W14X193	W14X426	W14X145	124' - 6" Level 9
111' - 0" Level 8	W14X61	W14X233	W27X194	W14X99	W14X426	W14X500	W14X193	111' - 0" Level 8
97' - 6"								97' - 6"
Column Locations	A-1, A-6, H-1, H-6	A-2, A-5, C-1, C-6, F-1, F-6, H-2, H-5	A-3, A-4, D-1, D-6, E-1, E-6, H-3, H-4	B-1, B-6, G-1, G-6	B-2, B-5, C-2, C-5, F-2, F-5, G-2, G-5	B-3, B-4, D-2, D-5, E-2, E-5, G-3, G-4	C-3, C-4, D-3, D-4, E-3, E-4, F-3, F-4	

Caltech

http://www.mce.caltech.edu/

CALTECH

20 STORY

COLUMN SCHEDULE

Project number	Project Number
Date	3/25/2014
Drawn by	Anthony Massari
Checked by	Anthony Massari

S.4.2

Scale 1/16" = 1'-0"

9/29/2015 9:54:18 AM

Roof								Roof
273' - 0" Level 20	W14X61	W14X132	W24X94	W14X48	W14X48	W14X132	W14X48	273' - 0" Level 20
259' - 6" Level 19	W14X61	W14X132	W24X94	W14X48	W14X48	W14X132	W14X48	259' - 6" Level 19
246' - 0" Level 18	W14X61	W14X132	W24X131	W14X48	W14X68	W14X193	W14X61	246' - 0" Level 18
232' - 6" Level 17	W14X61	W14X132	W24X131	W14X48	W14X68	W14X193	W14X61	232' - 6" Level 17
219' - 0" Level 16	W14X61	W14X132	W24X146	W14X61	W14X82	W14X342	W14X82	219' - 0" Level 16
205' - 6" Level 15	W14X61	W14X132	W24X146	W14X61	W14X82	W14X342	W14X82	205' - 6" Level 15
192' - 0" Level 14	W14X61	W14X159	W24X162	W14X68	W14X132	W14X426	W14X90	192' - 0" Level 14
178' - 6"								178' - 6"
Column Locations	A-1, A-6, H-1, H-6	A-2, A-5, C-1, C-6, F-1, F-6, H-2, H-5	A-3, A-4, D-1, D-6, E-1, E-6, H-3, H-4	B-1, B-6, G-1, G-6	B-2, B-5, C-2, C-5, F-2, F-5, G-2, G-5	B-3, B-4, D-2, D-5, E-2, E-5, G-3, G-4	C-3, C-4, D-3, D-4, E-3, E-4, F-3, F-4	

Caltech

http://www.mce.caltech.edu/

CALTECH

20 STORY

COLUMN SCHEDULE

Project number	Project Number
Date	3/25/2014
Drawn by	Author
Checked by	Checker

S.4.3

Scale 1/16" = 1'-0"

9/29/2015 9:54:18 AM

Appendix D

Building Information				Displacement (mm)								
Story	Floor Height	Elev	Floor Weight	Max Inelastic Displacement			Shear Deflected Shape			Flexural Deflected Shape		
	m	m	kN	1.0%	1.5%	2.0%	1.0%	1.5%	2.0%	1.0%	1.5%	2.0%
20	3.96	79.2	4.4482	792	1189	1585	505	757	1009	328	491	655
19	3.96	75.3	4.4482	753	1129	1506	503	754	1006	289	434	579
18	3.96	71.3	4.4482	713	1070	1426	498	747	997	254	382	509
17	3.96	67.4	4.4482	674	1010	1347	491	736	981	222	333	445
16	3.96	63.4	4.4482	634	951	1268	480	720	960	193	289	386
15	3.96	59.4	4.4482	594	892	1189	466	699	932	166	249	332
14	3.96	55.5	4.4482	555	832	1109	450	674	899	142	212	283
13	3.96	51.5	4.4482	515	773	1030	430	645	860	120	179	239
12	3.96	47.5	4.4482	475	713	951	408	612	816	100	150	199
11	3.96	43.6	4.4482	436	654	872	384	575	767	82	123	164
10	3.96	39.6	4.4482	396	594	792	357	535	713	66	100	133
9	3.96	35.7	4.4482	357	535	713	328	491	655	53	79	105
8	3.96	31.7	4.4482	317	475	634	297	445	593	41	61	81
7	3.96	27.7	4.4482	277	416	555	264	395	527	30	46	61
6	3.96	23.8	4.4482	238	357	475	229	344	458	22	33	44
5	3.96	19.8	4.4482	198	297	396	193	290	386	15	22	30
4	3.96	15.8	4.4482	158	238	317	156	234	312	9	14	19
3	3.96	11.9	4.4482	119	178	238	118	177	236	5	8	10
2	3.96	7.9	4.4482	79	119	158	79	118	158	2	3	4
1	3.96	4.0	4.4482	40	59	79	40	59	79	1	1	1
0	0.00	0.0	4.4482	0	0	0	0	0	0	0	0	0

App. D.1 - Displacement Analysis

Building Information				Drift								
Story	Floor Height	Elev	Floor Weight	Max Inelastic Displacement			Shear Deflected Shape			Flexural Deflected Shape		
	m	m	kN	1.0%	1.5%	2.0%	1.0%	1.5%	2.0%	1.0%	1.5%	2.0%
20	3.96	79.2	4.4482	1.00%	1.50%	2.00%	0.04%	0.06%	0.08%	0.96%	1.44%	1.92%
19	3.96	75.3	4.4482	1.00%	1.50%	2.00%	0.12%	0.18%	0.24%	0.88%	1.33%	1.77%
18	3.96	71.3	4.4482	1.00%	1.50%	2.00%	0.20%	0.29%	0.39%	0.81%	1.22%	1.62%
17	3.96	67.4	4.4482	1.00%	1.50%	2.00%	0.27%	0.41%	0.54%	0.74%	1.11%	1.49%
16	3.96	63.4	4.4482	1.00%	1.50%	2.00%	0.35%	0.52%	0.69%	0.68%	1.02%	1.36%
15	3.96	59.4	4.4482	1.00%	1.50%	2.00%	0.42%	0.63%	0.84%	0.62%	0.92%	1.23%
14	3.96	55.5	4.4482	1.00%	1.50%	2.00%	0.49%	0.73%	0.98%	0.56%	0.83%	1.11%
13	3.96	51.5	4.4482	1.00%	1.50%	2.00%	0.56%	0.83%	1.11%	0.50%	0.75%	1.00%
12	3.96	47.5	4.4482	1.00%	1.50%	2.00%	0.62%	0.93%	1.24%	0.45%	0.67%	0.89%
11	3.96	43.6	4.4482	1.00%	1.50%	2.00%	0.68%	1.02%	1.36%	0.40%	0.59%	0.79%
10	3.96	39.6	4.4482	1.00%	1.50%	2.00%	0.73%	1.10%	1.47%	0.35%	0.52%	0.69%
9	3.96	35.7	4.4482	1.00%	1.50%	2.00%	0.79%	1.18%	1.57%	0.30%	0.45%	0.60%
8	3.96	31.7	4.4482	1.00%	1.50%	2.00%	0.83%	1.25%	1.66%	0.26%	0.39%	0.52%
7	3.96	27.7	4.4482	1.00%	1.50%	2.00%	0.87%	1.31%	1.74%	0.22%	0.32%	0.43%
6	3.96	23.8	4.4482	1.00%	1.50%	2.00%	0.91%	1.36%	1.82%	0.18%	0.27%	0.35%
5	3.96	19.8	4.4482	1.00%	1.50%	2.00%	0.94%	1.41%	1.88%	0.14%	0.21%	0.28%
4	3.96	15.8	4.4482	1.00%	1.50%	2.00%	0.96%	1.44%	1.92%	0.11%	0.16%	0.21%
3	3.96	11.9	4.4482	1.00%	1.50%	2.00%	0.98%	1.47%	1.96%	0.07%	0.11%	0.15%
2	3.96	7.9	4.4482	1.00%	1.50%	2.00%	0.99%	1.49%	1.99%	0.04%	0.06%	0.08%
1	3.96	4.0	4.4482	1.00%	1.50%	2.00%	1.00%	1.50%	2.00%	0.01%	0.02%	0.03%
0	0.00	0.0	4.4482	1.00%	1.50%	2.00%	1.00%	1.50%	2.00%	0.00%	0.00%	0.00%

App. D.2 - Drift Analysis

Building Information				Horizontal Force (N)								
Story	Floor Height	Elev	Floor Weight	Max Inelastic Displacement			Shear Deflected Shape			Flexural Deflected Shape		
	m	m	kN	1.0%	1.5%	2.0%	1.0%	1.5%	2.0%	1.0%	1.5%	2.0%
20	3.96	79.2	4.4482	44.5	66.7	89.0	1.7	2.6	3.5	42.7	64.1	85.5
19	3.96	75.3	4.4482	44.5	66.7	89.0	8.7	13.1	17.4	36.0	53.9	71.9
18	3.96	71.3	4.4482	44.5	66.7	89.0	15.6	23.4	31.1	29.7	44.5	59.4
17	3.96	67.4	4.4482	44.5	66.7	89.0	22.3	33.4	44.5	23.9	35.8	47.7
16	3.96	63.4	4.4482	44.5	66.7	89.0	28.7	43.0	57.4	18.5	27.7	37.0
15	3.96	59.4	4.4482	44.5	66.7	89.0	34.7	52.1	69.5	13.5	20.3	27.0
14	3.96	55.5	4.4482	44.5	66.7	89.0	40.4	60.6	80.8	8.9	13.4	17.9
13	3.96	51.5	4.4482	44.5	66.7	89.0	45.5	68.3	91.1	4.7	7.0	9.4
12	3.96	47.5	4.4482	44.5	66.7	89.0	50.1	75.2	100.3	0.8	1.2	1.6
11	3.96	43.6	4.4482	44.5	66.7	89.0	54.1	81.1	108.2	-2.8	-4.2	-5.6
10	3.96	39.6	4.4482	44.5	66.7	89.0	57.3	86.0	114.7	-6.1	-9.1	-12.1
9	3.96	35.7	4.4482	44.5	66.7	89.0	59.9	89.8	119.7	-9.1	-13.6	-18.1
8	3.96	31.7	4.4482	44.5	66.7	89.0	61.6	92.4	123.2	-11.8	-17.7	-23.5
7	3.96	27.7	4.4482	44.5	66.7	89.0	62.5	93.8	125.0	-14.2	-21.3	-28.4
6	3.96	23.8	4.4482	44.5	66.7	89.0	62.6	93.9	125.2	-16.4	-24.6	-32.8
5	3.96	19.8	4.4482	44.5	66.7	89.0	61.8	92.6	123.5	-18.4	-27.5	-36.7
4	3.96	15.8	4.4482	44.5	66.7	89.0	60.1	90.1	120.1	-20.0	-30.1	-40.1
3	3.96	11.9	4.4482	44.5	66.7	89.0	57.5	86.2	114.9	-21.5	-32.2	-43.0
2	3.96	7.9	4.4482	44.5	66.7	89.0	54.0	81.0	108.0	-22.7	-34.0	-45.4
1	3.96	4.0	4.4482	44.5	66.7	89.0	49.6	74.5	99.3	-23.6	-35.4	-47.2
0	0.00	0.0	4.4482	44.5	66.7	89.0	45.4	68.1	90.8	-23.6	-35.4	-47.2

App. D.3 - Horizontal Force Analysis

Building Information				Shear Force (N)								
Story	Floor Height	Elev	Floor Weight	Max Inelastic Displacement			Shear Deflected Shape			Flexural Deflected Shape		
	m	m	kN	1.0%	1.5%	2.0%	1.0%	1.5%	2.0%	1.0%	1.5%	2.0%
20	3.96	79.2	4.4482	44.5	66.7	89.0	1.7	2.6	3.5	42.7	64.1	85.5
19	3.96	75.3	4.4482	89.0	133.4	177.9	10.5	15.7	20.9	78.7	118.0	157.4
18	3.96	71.3	4.4482	133.4	200.2	266.9	26.0	39.0	52.1	108.4	162.6	216.8
17	3.96	67.4	4.4482	177.9	266.9	355.9	48.3	72.4	96.6	132.2	198.4	264.5
16	3.96	63.4	4.4482	222.4	333.6	444.8	77.0	115.4	153.9	150.7	226.1	301.5
15	3.96	59.4	4.4482	266.9	400.3	533.8	111.7	167.6	223.4	164.3	246.4	328.5
14	3.96	55.5	4.4482	311.4	467.1	622.8	152.1	228.2	304.2	173.2	259.8	346.4
13	3.96	51.5	4.4482	355.9	533.8	711.7	197.7	296.5	395.3	177.9	266.8	355.8
12	3.96	47.5	4.4482	400.3	600.5	800.7	247.8	371.7	495.6	178.7	268.0	357.4
11	3.96	43.6	4.4482	444.8	667.2	889.6	301.9	452.8	603.7	175.9	263.8	351.8
10	3.96	39.6	4.4482	489.3	734.0	978.6	359.2	538.8	718.4	169.8	254.7	339.7
9	3.96	35.7	4.4482	533.8	800.7	1067.6	419.1	628.6	838.2	160.8	241.2	321.5
8	3.96	31.7	4.4482	578.3	867.4	1156.5	480.7	721.0	961.4	149.0	223.5	298.0
7	3.96	27.7	4.4482	622.8	934.1	1245.5	543.2	814.8	1086.4	134.8	202.2	269.6
6	3.96	23.8	4.4482	667.2	1000.8	1334.5	605.8	908.7	1211.6	118.4	177.5	236.7
5	3.96	19.8	4.4482	711.7	1067.6	1423.4	667.6	1001.3	1335.1	100.0	150.0	200.0
4	3.96	15.8	4.4482	756.2	1134.3	1512.4	727.6	1091.4	1455.2	80.0	119.9	159.9
3	3.96	11.9	4.4482	800.7	1201.0	1601.4	785.1	1177.6	1570.2	58.5	87.7	116.9
2	3.96	7.9	4.4482	845.2	1267.7	1690.3	839.1	1258.6	1678.2	35.8	53.7	71.6
1	3.96	4.0	4.4482	889.6	1334.5	1779.3	888.7	1333.1	1777.5	12.2	18.2	24.3
0	0.00	0.0	4.4482	934.1	1401.2	1868.3	934.1	1401.2	1868.3	-11.5	-17.2	-22.9

App. D.4 - Shear Force Analysis

Building Information				Moment (kN-m)								
Story	Floor Height	Elev	Floor Weight	Max Inelastic Displacement			Shear Deflected Shape			Flexural Deflected Shape		
	m	m	kN	1.0%	1.5%	2.0%	1.0%	1.5%	2.0%	1.0%	1.5%	2.0%
20	3.96	79.2	4.4482	0.0	0.0	0.0	0.0	0.0	0.0	0.0	0.0	0.0
19	3.96	75.3	4.4482	0.2	0.3	0.4	0.0	0.0	0.0	0.2	0.3	0.3
18	3.96	71.3	4.4482	0.5	0.8	1.1	0.0	0.1	0.1	0.5	0.7	1.0
17	3.96	67.4	4.4482	1.1	1.6	2.1	0.2	0.2	0.3	0.9	1.4	1.8
16	3.96	63.4	4.4482	1.8	2.6	3.5	0.3	0.5	0.7	1.4	2.2	2.9
15	3.96	59.4	4.4482	2.6	4.0	5.3	0.6	1.0	1.3	2.0	3.0	4.1
14	3.96	55.5	4.4482	3.7	5.6	7.4	1.1	1.6	2.2	2.7	4.0	5.4
13	3.96	51.5	4.4482	4.9	7.4	9.9	1.7	2.5	3.4	3.4	5.1	6.7
12	3.96	47.5	4.4482	6.3	9.5	12.7	2.5	3.7	5.0	4.1	6.1	8.1
11	3.96	43.6	4.4482	7.9	11.9	15.9	3.5	5.2	6.9	4.8	7.2	9.6
10	3.96	39.6	4.4482	9.7	14.5	19.4	4.7	7.0	9.3	5.5	8.2	11.0
9	3.96	35.7	4.4482	11.6	17.4	23.3	6.1	9.1	12.2	6.2	9.2	12.3
8	3.96	31.7	4.4482	13.7	20.6	27.5	7.7	11.6	15.5	6.8	10.2	13.6
7	3.96	27.7	4.4482	16.0	24.1	32.1	9.6	14.5	19.3	7.4	11.1	14.8
6	3.96	23.8	4.4482	18.5	27.8	37.0	11.8	17.7	23.6	7.9	11.9	15.8
5	3.96	19.8	4.4482	21.2	31.7	42.3	14.2	21.3	28.4	8.4	12.6	16.8
4	3.96	15.8	4.4482	24.0	36.0	47.9	16.8	25.3	33.7	8.8	13.2	17.6
3	3.96	11.9	4.4482	27.0	40.5	53.9	19.7	29.6	39.4	9.1	13.6	18.2
2	3.96	7.9	4.4482	30.1	45.2	60.3	22.8	34.3	45.7	9.3	14.0	18.7
1	3.96	4.0	4.4482	33.5	50.2	67.0	26.2	39.2	52.3	9.5	14.2	18.9
0	0.00	0.0	4.4482	37.0	55.5	74.0	29.7	44.5	59.4	9.5	14.3	19.0

App. D.5 - Moment Analysis